QATAR UNIVERSITY

COLLEGE OF ENGINEERING

CHARACTERIZING TRAPPED NAPL IN PORE NETWORKS OF UNCONSOLIDATED SAND USING SYNCHROTRON MICRO-COMPUTED TOMOGRAPHY

BY

JAMEEL ADEL IBRAHIM HANNUN

A Thesis Submitted to

the College of Engineering

in Partial Fulfillment of the Requirements for the Degree of

Master of Science in Environmental Engineering

June 2021

COMMITTEE PAGE

The members of the Committee approve the thesis of
Jameel Adel Ibrahim Hannun defended on 19/04/2021.

Prof. Riyadh Al-Raoush
Thesis/Dissertation Supervisor

Dr. Thomas Seers
Committee Member

Dr. Anand Kumar
Committee Member

Dr. Galal Abdella
Committee Member

Approved:

Khalid Kamal Naji, Dean, College of Engineering

ABSTRACT

HANNUN, JAMEEL, A., Masters : June : 2021, Masters of Science in Environmental Engineering

Title: Characterizing Trapped NAPL in Pore Networks of Unconsolidated Sand Using Synchrotron Micro-Computed Tomography:

Supervisor of Thesis: Riyadh, I, Al-Raoush.

The purpose of this research paper was to determine the correlation of occupancy percentage against the pore radius and coordination numbers for each pore space. X-ray micro-computed tomography images were taken for the fifteen unconsolidated porous media samples (silica sand, quartz sand, and mixed sand) after applying the flooding procedures. The flooding procedure started with water imbibition (at 4.07ml/hr), followed by the introduction of sterol 220 (representing the NAPL phase) and finally water flushing. It was first observed that the maximum occupancy in all samples did not exceed 80%. Additionally, intervals increase for pores having 20% or more occupancy, while it decreased for pores occupied with 10% or less with the increase in pore radius. Finally, pores with coordination numbers five or higher were split either above 50% occupancy or below 10% occupancy.

DEDICATION

This research work is dedicated to my family, Qatar University, and researchers studying within similar fields.

ACKNOWLEDGMENTS

Lots of thanks to Prof. Riyadh Al-Raoush and Dr. Jamal Hannun for offering their time and resources with me to complete this research work. Special thanks to Argonne National Laboratory for helping us in acquiring three-dimensional micro-computed tomography images for all of the fifteen sand samples.

TABLE OF CONTENT

DEDICATION iv

ACKNOWLEDGMENTS v

LIST OF TABLES ix

LIST OF FIGURES x

CHAPTER 1: INTRODUCTION 1

1.1 Overview of Residual NAPL 1

1.2 Overview of Unconsolidated Sand 2

1.3 Overview of Pore Networks 3

1.4 Thesis Structure 5

1.4.1 Chapter 1: Introduction 5

1.4.2 Chapter 2: Review in Literature 5

1.4.3 Chapter 3: Methodology 5

1.4.4 Chapter 4: Analysis 5

1.4.5 Chapter 5: Results and Discussion 6

1.4.6 Chapter 6: Conclusions 6

1.5 Thesis Main Objectives 6

CHAPTER 2: REVIEW IN LITERATURE 7

2.1 Topic's Importance and Imaging Background 7

2.2 Previous Studies 9

2.3 Knowledge Gap 15

CHAPTER 3: METHODOLOGY 16

3.1 Materials and Sediments 16

3.2 Experimental Setup 17

3.3 Experimental Procedure 18

3.4 Imaging 19

CHAPTER 4: ANALYSIS 20

4.1 Image Analysis 20

4.1.1 Median Filter Process 20

4.1.2 Segmentation 22

4.2 Pore Network Analysis 26

4.2.1 Grain-Based Algorithm 26

CHAPTER 5: RESULTS AND DISCUSSION 27

5.1 3D and 2D Images 27

5.2 Sand Labeled Grain Images 37

5.3 Ganglia Labeled Images 46

5.4 System Characterization 56

5.4.1 Trapped NAPL Blobs Characterization 60

5.4.2 Grain Characterization 74

5.5 NAPL Occupancy vs Pore Size and Pore Coordination Number 84

CHAPTER 6: CONCLUSIONS 103

REFERENCES 105

LIST OF TABLES

Table 1. List of EPA DNAPL Chemical Compounds. 4

Table 2. List of major oil spills around the world.....7

Table 3. List of several photon source synchrotrons. 8

Table 4. List of Porous Medium Used in the Experiment with their Physical Properties. 17

LIST OF FIGURES

Figure 1. Shows the Relationship Between Morphological Aspect Ration and Residual Oil Saturation 12

Figure 2. Image of the Experimental Setup for the Aluminum Column 19

Figure 3. Median Filter Mechanism for a 2D Image. 20

Figure 4. Sample Image Histogram. 21

Figure 5. Segmented Images of Mixed Sample M1 (a), Quartz Sample Q1 (b), and Silica Sand Sample S1 (c). 22

Figure 6. Segmented Image of De-aired Water (b) of Mix Sample M1. 23

Figure 7. Segmented Image of Residual NAPL (b) of Mix Sample M1. 24

Figure99. Segmented Image of Air (b) of Mix Sample M1. 25

Figure88. Segmented Image of Sand (b) of Mix Sample M1. 25

Figure 10. 2D Labeled Images of All Silica Sand Samples. 29

Figure 11. 2D Labeled Images of All Quartz Sand Samples. 30

Figure 12. 2D Labeled Images of All Mixed Sand Samples. 31

Figure 13. 3D Pore Network Images for Silica Sand Samples S1-S3. 32

Figure 14. 3D Pore Network Images for Silica Sand Samples S4-S6. 33

Figure 15. 3D Pore Network Images for Quartz Sand Samples Q1-Q3. 34

Figure 16. 3D Pore Network Images for Quartz Sand Samples Q4-Q6. 35

Figure 17. 3D Pore Network Images for Mixed Sand Samples M1-M3. 36

Figure 18. 2D Labeled Silica Sand Grains. 38

Figure 19. 2D Labeled Quartz Sand Grains. 39

Figure 20. 2D Labeled Mixed Sand Grains. 40

Figure 21. 3D Labeled Silica Sand Grains S1-S3. 41

Figure 22. 3D Labeled Silica Sand Grains S4-S6. 42
Figure 23. 3D Labeled Quartz Sand Grains Q1-Q3. 43
Figure 24. 3D Labeled Quartz Sand Grains Q4-Q6. 44
Figure 25. 3D Labeled Mixed Sand Grains M1-M3. 45
Figure 26. 2D Residual Oil Ganglia Labeling in Silica Sand. 48
Figure 27. 2D Residual Oil Ganglia Labeling in Quartz Sand. 49
Figure 28. 2D Residual Oil Ganglia Labeling in Mixed Sand. 50
Figure 29. 3D Residual Oil Ganglia Labeling in Silica Sand S1-S3. 51
Figure 30. 3D Residual Oil Ganglia Labeling in Silica Sand S4-S6. 52
Figure 31. 3D Residual Oil Ganglia Labeling in Quartz Sand Q1-Q3. 53
Figure 32. 3D Residual Oil Ganglia Labeling in Quartz Sand Q4-Q6. 54
Figure 33. 3D Residual Oil Ganglia Labeling in Mixed Sand M1-M3. 55
Figure. 35 Oil and Water Saturations Relation With Sand Average Pores and Throats Radiuses for All Samples. 58
Figure 34. Oil and Water Saturations Relation With Sand Porosity for All Samples .58
Figure 36. Oil and Water Saturations Relation With Sand Average Coordination Number and Averarge Pore-Throat Aspect Ratio. 59
Figure 37. Probability Against Blob's Surface Area Over Blob's Volume for All Silica Sand Samples S1-S6. 62
Figure 38. Probability Against Blob's Surface Area Over Blob's Volume for All Quartz Sand Samples Q1-Q6. 63
Figure 39. Probability Against Blob's Surface Area Over Blob's Volume for All Mixed Sand Samples M1-M3 64
Figure 40. Probability Against Blob's Aspect Ratio for All Silica Sand Samples S1-S6.

.....65
Figure 41. Probability Against Blob's Aspect Ratio for All Quartz Sand Samples Q1-Q6.....66
Figure 42. Probability Against Blob's Aspect Ratio for All Mixed Sand Samples M1-M3.....67
Figure 43. Probability Against Blob's Equivalent Diameter for All Silica Sand Samples S1-S6.....68
Figure 44. Probability Against Blob's Equivalent Diameter for All Quartz Sand Samples Q1-Q6. 69
Figure 45. Probability Against Blob's Equivalent Diameter for All Mixed Sand Samples M1-M3. 70
Figure 46. Probability Against Blob's Volume for All Silica Sand Samples S1-S6....71
Figure 47. Probability Against Blob's Volume for All Quartz Sand Samples Q1-Q6.72
Figure 48. Probability Against Blob's Volume for All Mixed Sand Samples M1-M3. 73
Figure 49. Probability Against Grain's Aspect Ratio for All Silica Sand Samples S1-S6. 75
Figure 50. Probability Against Grain's Aspect Ratio for All Quartz Sand Samples Q1-Q6.....76
Figure 51. Probability Against Grain's Aspect Ratio for All Mixed Sand Samples M1-M3. 77
Figure 52. Probability Against Grains's Diameter for All Silica Sand Samples S1-S6. 78
Figure 53. Probability Against Grains's Diameter for All Quartz Sand Samples Q1-Q6.

.....79
Figure 54. Probability Against Grains's Diameter for All Mixed Sand Samples M1-M3.
.....80
Figure 55. Probability Against Grains's Volume for All Silica Sand Samples S1-S6. 81
Figure 56. Probability Against Grains's Volume for All Quartz Sand Samples Q1-Q6.
.....82
Figure 57. Probability Against Grains's Volume for All Mixed Sand Samples M1-M3.
.....83
Figure 58. Residual Oil Occupancy Percentage Against Pore Radius for Each Pore in Silica Sand Systems S1-S6. 86
Figure 59. Residual Oil Occupancy Percentage Against Pore Radius for Each Pore in Quartz Sand Systems Q1-Q6. 87
Figure 60. Residual Oil Occupancy Percentage Against Pore Radius for Each Pore in Mixed Sand Systems Q1-Q3.....88
Figure 61. Residual Oil Occupancy Percentage Against Pore Coordination Number for Each Pore in Silica Sand Systems S1-S6.....89
Figure 62. Residual Oil Occupancy Percentage Against Pore Coordination Number for Each Pore in Quartz Sand Systems Q1-Q6.....90
Figure 63. Residual Oil Occupancy Percentage Against Pore Coordination Number for Each Pore in Mixed Sand Systems M1-M3.....91
Figure 64. Pore Probability Against Pore Radiuses Histogram for Silica Sand Samples S1-S6.....94
Figure 65. Pore Probability Against Pore Radiuses Histogram for Quartz Sand Samples Q1-Q6. 95

Figure 66. Pore Probability Against Pore Radiuses Histogram for Mixed Sand Samples M1-M3. 96

Figure 67. Pore Probability Against Pore Occupancy Histogram for Silica Sand Samples S1-S6. 97

Figure 68. Pore Probability Against Pore Occupancy Histogram for Quartz Sand Samples Q1-Q6. 98

Figure 69. Pore Probability Against Pore Occupancy Histogram for Mixed Sand Samples M1-M3 99

Figure 70. Pore Probability Against Pore Coordination Number Histogram for Silica Sand Samples S1-S6. 100

Figure 71. Pore Probability Against Pore Coordination Number Histogram for Quartz Sand Samples Q1-Q6. 101

Figure 72. Pore Probability Against Pore Coordination Number Histogram for Mixed Sand Samples M1-M3 102

CHAPTER 1: INTRODUCTION

1.1 Overview of Residual NAPL

Non-Aqueous phase liquids (NAPL) are liquids or wastes of organic origin having a low tendency of mixing with water due to their low solubility (Immiscible). Generally, NAPLs are hydrocarbons (Oils, Tar, Gasoline, etc.) that can come in contact with water or soil in many different ways such as spills from oil tankers, industrial areas, improper waste management, etc. NAPLs are considered water-soil contaminants and can act as a source of long-term pollution in waters and soils. The transport of NAPLs in soils is usually driven by gravitational and capillary forces, where NAPL particles start to separate into small blobs. Thus, large amounts of NAPLs end up as residuals in soil, presenting one of the most difficult problems that environmental engineers can face (Cowell, Kibbey, Zimmerman, & Hayes, 2000). NAPLs can be divided into two subcategories, dense non-aqueous phase liquids (DNAPL) and light non-aqueous phase liquids (LNAPL), where DNAPLs have a higher density than water while LNAPL has a lower density compared to water (Konečný, Boháček, Müller, Kovářová, & Sedláčková, 2003).

The major problem presented when dealing with DNAPL is low detection levels mainly caused by DNAPL migration in the subsurface which involves lots of variables. It is significant to mention that DNAPL hydrocarbon residuals (see Table 1. for examples of DNAPL compounds) can be present in four states (Huling & Weaver, 1991):

- Vapor State.
- Solid State (Adsorption).
- Dissolved State (with underground water).
- Non-dissolved State (Immiscible).

On the other hand, LNAPLs do present a major threat to nature as they can maintain a longer presence in the environment. It is estimated that 99% of leaked LNAPL will stay as residual in any given system mainly due to the extremely low miscibility feature of LNAPL. Furthermore, LNAPLs have the ability to contaminate larger volumes of soils and water as a result of their high toxicity. Preventing the usage of land or water bodies (Frollini & Petitta, 2018).

1.2 Overview of Unconsolidated Sand

In order to understand and characterize residual NAPL, it is important to identify the medium confining NAPLS. Unconsolidated sand (Selected in the thesis paper) can make up a perfect match with residual NAPLs due to the looseness of sand or stone structures. Thus, permitting easy transport on NAPL through a given volume of unconsolidated medium, additionally; enabling a good reserving space (Yu & Cheng, 2002). Unconsolidated sand is generally loose resulting in higher porosity as well as higher permeability in a given sample, meaning that such mediums have the potential to make up perfect oil and gas reservoirs if available, nevertheless; it can result in problematic situations in case of any toxic spill (due to its reserving capacity). However, the mechanism of fluids' transport in an unconsolidated media usually occurs through the empty spaces (voids-pores) between the grains (solids in general), where it is important to consider the following when experimenting with the flow patterns in an unconsolidated specimen:

- Size of pore spaces.
- Size of pore throats (effect on permeability).
- Coordination Number (number of throats connected to each pore).

1.3 Overview of Pore Networks

Pore network construction is an essential tool for predicting flow and migration trends at the pore scale that can be harnessed by several sciences and applications such as petroleum and environmental engineering applications. For instance, pore network modeling (PNM) can be utilized to efficiently generate capillary pressure and permeability curves of a given sample. Moreover, one of the main advantages of pore network modeling is that it does not only result in a better understanding of the flow and transport of large-scale reservoirs, yet it contributes to predictions in a more economic and less time-consuming manner (Raeini, Bijeljic, & Blunt, 2017); (Dong & Blunt, 2009). Having said that, constructing a pore network model comes with its own difficulties, according to Xiong et al. (2016) a good pore network model is the model that best represents a real pore space from a geometrical and topological point of view. The good PNM should represent the distribution of voids and throats while considering their locations. Thus, to construct a pore network model there are generally three main paths, where each path has its own different models:

- Stochastic Equivalent Network.
    - Statistical reconstruction.
        - 2D sediment sections
        - Mercury intrusion test.
- Direct mapping of porous media.
    - Medial axis algorithm.
    - Maximal ball algorithm.
- Grain-based approach.

Due to the broad size of pores and throats in various types of sediments (i.e. variation in sorting and grain size), two approaches are used to extract the pore structure of the sediments using volume images:

- Regular network model.
- Two-scale pore network model (used in rocks).

Table 1. List of EPA DNAPL chemical compounds.

Compound	Density	Compound	Density
Halogenated Semi-volatiles		1,1,2,2-Tetrachloroethane	1.6
1,4-Dichlorobenzene	1.2475	Tetrachloroethylene	1.625
1,2-Dichlorobenzene	1.306	Ethylene Dibromide	2.172
Aroclor 1242	1.385	Non-halogenated Semi-volatiles	
Aroclor 1260	1.44	2-Methyl Napthalene	1.0058
Aroclor 1254	1.538	o-Cresol	1.0273
Chlordane	1.6	p-Cresol	1.0347
Dieldrin	1.75	2,4-Dimethylphenol	1.036
2,3,4,6-Tetrachlorophenol	1.839	m-Cresol	1.038
Pentachlorophenol	1.978	Phenol	1.0576
Halogenated Volatiles		Naphthalene	1.162
Chlorobenzene	1.106	Benzo(a)Anthracene	1.174
1,2-Dichloropropane	1.158	Flourene	1.203
1,1-Dichloroethane	1.175	Acenaphthene	1.225
1,1-Dichloroethylene	1.214	Anthracene	1.25
1,2-Dichloroethane	1.253	Dibenz(a,h)Anthracene	1.252
Trans-1,2-Dichloroethylene	1.257	Fluoranthene	1.252
Cis-1,2-Dichloroethylene	1.248	Pyrene	1.271
1,1,1-Trichloroethane	1.325	Chrysene	1.274
Methylene Chloride	1.325	2,4-Dinitrophenol	1.68
1,1,2-Trichloroethane	1.4436	Miscellaneous	
Trichloroethylene	1.462	Coal Tar	1.028
Chloroform	1.485	Creosote	1.05
Carbon Tetrachloride	1.5947		

Note. Data are from (Huling & Weaver, 1991).

1.4 Thesis Structure

The thesis report will be divided into six main chapters, an introduction, review in literature, methodology, analysis, results and discussion, and finally a conclusion section. Each section will have a brief description as follows:

1.4.1 Chapter 1: Introduction

The introduction section has five subsections, where it starts with overviewing three significant concepts that will be used in the thesis report (NAPLs, unconsolidated sand, and pore network model). The three subsections are then followed by a section that defines the thesis structure. Finally, the thesis's main objectives are listed.

1.4.2 Chapter 2: Review in Literature

The literature review starts with defining the topic’s background while giving examples. Then, lists the previous studies in the same field and their outcomes. The final sentences of the literature review chapter will state the gap of knowledge.

1.4.3 Chapter 3: Methodology

The methodology section starts by defining all materials, compounds and apparatus used, followed by listing the experimental procedure step by step. The methodology part will ultimately include the imaging process (resolution, size, and synchrotron).

1.4.4 Chapter 4: Analysis

There will be two main subsections in the analysis chapter, the image analysis as well as the pore network analysis subsections. The image analysis will mainly target the NAPL and grain segmentation. Whereas the pore network analysis will focus on the algorithm of NAPL and ganglia pore intersections.

1.4.5 Chapter 5: Results and Discussion

In the results and discussion chapter, 3D and 2D images representing the system features will be presented. Finally, occupancy (residual NAPL) versus pore radius graphs will be plotted, in addition to plotting the occupancy versus coordination number graphs. These graphs are targeted to cover the thesis objectives and the gap of knowledge.

1.4.6 Chapter 6: Conclusions

In the conclusion section, the main topic will be generally rewritten and then all outcomes will be summarized point by point.

1.5 Thesis Main Objectives

The thesis work has three main objectives:

- To use 3D micro-computed tomography images to detect residual NAPL in unconsolidated media.
- To determine the occupancy (of residual NAPL) ratio in pores with respect to pore sizes for various unconsolidated sands.
- To determine the occupancy (of residual NAPL) ratio in pores to the coordination number of pores for various unconsolidated sands.

CHAPTER 2: REVIEW IN LITERATURE

2.1 Topic's Importance and Imaging Background

Characterizing unconsolidated sand systems that can have large oil occupancy potentials is very significant for several reasons. One major reason for the study is to develop higher oil recovery percentages, especially after noting that such mediums can maintain between 15-35% of oil residuals in their pores after initial recovery (Chatzis, Morrow, & Lim, 1983). So, an enhancement in the oil recovery field will definitely have a considerable economic and environmental return. When speaking about considerable environmental returns, it is a must to mention the process of Carbon storage that could benefit from unconsolidated sand systems characterizations in order to have an improved storage capacity (Stefan Iglauer, Favretto, Spinelli, Schena, & Blunt, 2010). One more reason for such a study is to help in the remediation processes (extracting harmful oils) that are generally resulted from oil spills worldwide (See Table 2. list of some of the major oil spills).

Table 2. List of major oil spills around the world.

Country	Location	Year	Metric Tonnes
Kuwait	Arabian Gulf/ On Shore	1991	544,00-816,300[a-f]
Mexico	Gulf of Mexico	1980	475,000[b]
Nigeria	Niger Delta	1976-1996	322,248[c]
USA	Lakeview Gusher	1911	12,000,00[d]
USA	Gulf of Mexico (Deepwater Horizon)	2010	585,000[d]
Trinidad and Tobago	Caribbean	1979	287,000[d]
Angola	Angolan coast	1991	260,000[e]
Uzbekistan	Fergana Valley	1992	285,000[d]
Iran	Nowruz Field	1983	272,109[f]
South Africa	Cape Town Coast	1983	267,007[f]

Note. Data are from (Khordagui & Al-Ajmi, 1993)[a], (Jernelöv & Lindén, 1981)[b], (Nwilo & Badejo, 2005)[c], (Q. Wang et al., 2011)[d], (Huijer, n.d.)[e], and (Etkin, 1999)[f].

X-ray Micro-computed tomography (μ-CT) technology can be harnessed effectively to study geo-samples in several ways. Earlier, researchers had limited resources or methods that can help them to inspect a sediment sample. Fortunately, with the advances in science, cutting-edge technologies such as micro-computed tomography became available for researchers to scan their samples. Currently, using μ-CT is considered the most technologically advanced technique to scan sediment samples. Photon sources generate x-rays that are capable of penetrating low-medium density solids in samples providing micro-scale volume images, that can be later rendered into three-dimensional models for further studies. Generally, such tests utilize lab tomography (Compact Light Sources), while dynamic multiphase tests use Synchrotron facilities (see Table 3. examples of active Photon Source Synchrotrons).

Table 3. List of several photon source synchrotrons.

Facility Name	Country	Energy (GeV)	Circumference (m)
SPring-8	Japan	8	1,436
Advanced Photon Source (APS)	USA	7	1,104
PETRA III	Germany	6	2,304
European Synchrotron Radiation Facility (ESRF)	France	6	844
(SSRF)	China	3.5	432
Australian Synchrotron	Australia	3	216
Diamond Light Source	UK	3	561.6
SESAME	Jordan	2.5	133
National Synchrotron Light Source II	USA	3	792
PETRA II	Germany	12	2,304
National Accelerator Laboratory (SLAC)	USA	8	3,000
Cornell Laboratory for Accelerator-based Sciences and Education	USA	5.5	768
National Synchrotron Radiation Research Center	Taiwan	3	518.4
Sirius (synchrotron light source)	Brazil	3	518.2
Iranian Light Source Facility (ILSF)	Iran	3	489.6
MAX IV 3 GeV Storage Ring	Sweden	3	528

2.2 Previous Studies

The study of residual oils/oil entrapments in unconsolidated media can be traced back to the 1970s-1980s, mainly focusing on enhancements made for oil recovery. Despite the limitations in technologies at that time, researchers were able to come up with practical solutions to characterize a system of unconsolidated sand. For instance, Chatzis et al. (1983) used styrene monomer (having around 1% benzoyl peroxide that will polymerize the styrene) to act as the residual oil in Berea sandstone and glass bead packings. While the column samples were submerged in water, they went into constant pressure (70 PSI) and temperature (80^{o} C) for around 48 hours to promote the polymerization process of styrene. Mineral solvents were used to extract polymerized styrene blobs out of the sandstone columns. Finally, polymerized styrenes (representing oil residual) were imaged using an electron microscope. That procedure gave the researchers an insight into the different shapes oil blobs can make inside unconsolidated sand samples. Moreover, researchers were able to identify the percentages for different blob types in the sample (65% singlets, 20% doublets, and 15% branched). Similar to the previous study, glass bead columns were used to simulate an unconsolidated media. Columns were drained for 24 hours, followed by a flooding procedure that was carried out at different capillary numbers. Using gravimetric analysis, residual oil volumes were acquired. Several remarks were made for the characterization of residual oils, where it was clear that blobs movement without breaking into smaller volumes has a major effect on the relationship between the capillary number and blob size distribution (Morrow, Chatzis, & Taber, 1988). In another study, micromodels (two-dimensional) were used to investigate the movement of residual oil when gas flooded having more than 4,500 capillary intersections. Oil (Soltrol 130), distilled water, and gas were used as the displacing fluids. Initial results showed a residual oil saturation of values between

69%-75%. Moreover, it was observed that oil migrates by a double-drainage process. Finally, it was observed that residual oil values were lower in positive spreading coefficient systems compared to negative spreading coefficient systems (interfacial tension of water-gas deducted by interfacial tension of oil-gas, finally deducted by interfacial tension of oil-water) (Oren et al., 1992). In a similar packing technique, Karpyn et al. (2010) used columns packed with glass beads to simulate unconsolidated media. The columns were saturated with water and oil through nine steps, where x-ray images (μ-CT) were taken during that process. General characterization of the oil residuals was carried out, where it was observed that 98% of residual oil is constructed out of blobs of volumes less than $1mm^3$ (low contribution of large blob sizes). Additionally, residual oil blobs had the same structure after imbibition and drainage processes. Sandstone specimens were used in another experiment aimed at improving oil extraction and carbon-dioxide storage. 3D X-ray images (μ-CT) were taken for the sandstone specimen (Clashach and Doddington) and retained oil maps were simulated. The paper concluded that trapped oil will form a large surface area (different ganglia sizes) at the water injection sites for oil extraction or carbons injection aquifers (Iglauer et al., 2010). Another approach used micromodels to observe retained oil in the samples. Digital microscope shots were captured to observe oil blobs, where it showed that oil blob length had a widespread in the water-wet network (Jamaloei et al., 2011). Iglauer et al. (2013) conducted experiments on eight core samples containing different porous media (Clashach sandstone, quartz sand, Estaillades limestone, and Aerolith) with different wettabilities (water-wet or oil-wet). The flooding procedure took place via three different methods: water-gas-water, brine-oil, and the gas-water. Three-dimensional segmented systems were built using the micro-computed tomography images, where system features such as residual oil surface area versus volume and

residual oil distribution were plotted. However, two significant conclusions were that larger oil volumes can be extracted using direct gas flooding and that the gas-water procedure can result in larger gas storage. In another study aimed to investigate entrapped oil characteristics in Clashach sandstone, which were oil-flooded (with crude oil) then had water imbibition (brine) of about 50 pore volumes (PV). After that, micro-computed tomography images of Clashach columns were taken. It was concluded that the water-wet system had almost double the oil saturation of oil-wet systems (35% to 18.8%). Moreover, it was observed that residual oil clusters were more spherical in a water-wet system while having more of a sheet geometry in oil-wet systems (Iglauer et al., 2012). A group of researchers experimented with sandstone cores by utilizing x-ray micro-computed tomography scans of polymer, water, and performed particle gel floods. Scans were later used to construct a three-dimensional network (PNM) of the scanned samples. By constructing the model, it was observed that residual oil tends to have a significantly large size in comparison with the pore sizes (oil blobs approximately 20 times bigger than pores). It was also observed that more residual oil clusters were shaped when the volume of injection liquid was increased (Daigang et al., 2015). Iglauer et al. (2016) compared two different flooding procedures for a sandstone pack, where the first procedure starts with saturating the sample with oil (to simulate an oil reservoir) followed by gas injection and water flooding. In the second procedure, three flooding protocols were used for the saturated oil sample, where water is flooded twice, before the gas injection and after the gas injection. It was concluded that less oil was retained when applying the first flooding procedure (oil/gas-water) in a mixed-wet sample. In another related study, twelve samples having different materials (silica glass beads, borosilicate crushed glass, and Bentheimer sandstone) with different porosities and particle diameters. Twenty minutes after the end of the samples' imbibition

procedure (5-10 pore volumes of water) x-ray micro-computed tomography images were taken. The paper did discuss that there is no linear relationship between residual oil non-wetting saturation and pore's aspect ratios. Nevertheless, the researchers came up with a method to do so, where the pore radius of a given void was divided by the average radii of all throats connected to the same void (morphological aspect ratio). From this, a linear relationship was plotted indicating the increase of residual oil non-wetting saturation with the increase of morphological aspect ratio (see Figure 1.)/ (Andersson et al., 2018).

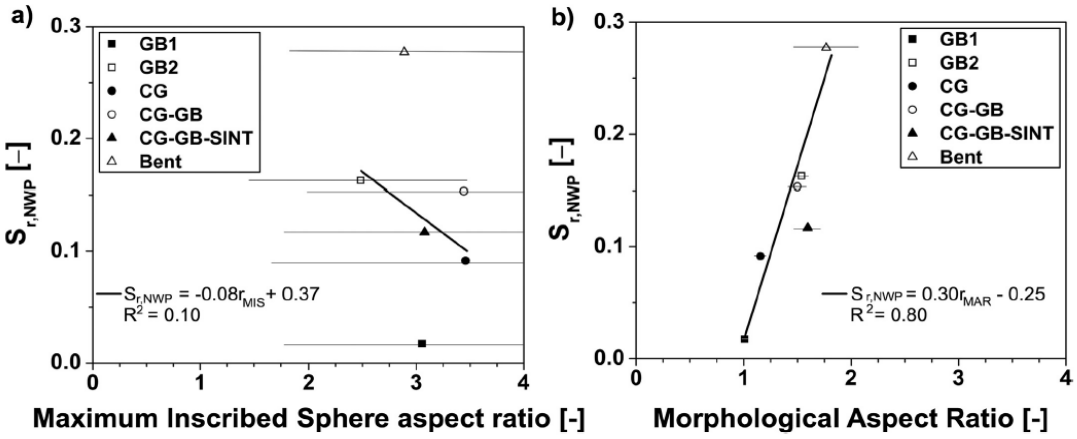

Figure 1. Shows the Relationship Between Morphological Aspect Ration and Residual Oil Saturation (Andersson et al., 2018).

Heshmati & Piri (2018) built two micromodels aimed to study the effects of flow on residual oil blobs in porous media, where one micromodel simulated a Bentheimer sandstone while the other micromodel simulated a single pore connected to four throats. For both setups, it was observed that higher injection speeds resulted in the formation of smaller residual oil cluster sizes. Moreover, increasing the injection rate of fluids caused some throats to have lower flow rates, mainly due to clogging caused by residual oil blobs. Using another technique, a sand column was studied to

observe the oil extraction using oil displacing liquids (emulsion). Thus, three total cores were prepared (emulsion, sand, and displacing cores) where the columns were fully saturated with brine then they were injected with oil, then the sample was injected again with brine. After that, oil displacing liquid was injected into the core at one pore volume. It was concluded that the oil-water interfacial tension had been weakened after injecting the oil displacing liquids causing less residual oil in the sample. Furthermore, oil recovery was approximately 9.84% more efficient in comparison with conventional surfactant flooding procedures (Zhou et al., 2018). Another study used six micromodels to having different surface roughness. porosities, and pore volumes (to simulate sandstones), where the main objective of the study was to observe the effect of surface roughness on residual oil at the pore-scale. The micromodels were first saturated with crude oil then gas injection was introduced using a syringe pump. Residual oil behavior was captured with the help of x-ray micro-computed tomography. It was concluded that surface roughness will decrease residual oils in the system by 10% (Mehmani et al., 2019). In another experiment conducted by Wang et al. (2019), four rock test columns were prepared (carbonate, Fontainebleau sandstone, and sandstone) with different porosities and permeabilities then the samples were flooded with oil and water. After that, x-ray micro-computed tomography scans were taken for the four samples, where three-dimensional images were rendered. Rocks' critical capillary number was generated for oil-wetted (10^{-5}) and water-wetted samples (10^{-6}). Also, it was observed that the lowest oil saturation occurs with weaky water-wet rocks. In another study, the study of sandstone samples was carried out to experiment with the effectiveness of using carbon dioxide gas to enhance oil recovery first then store the gas itself. The experiment was conducted on a sandstone micro-core (Bentheimer) that was initially water wet then was injected with oil. After that, oil was injected into the sample

followed by the injection of fifty pore volumes of water. Another oil flooding procedure was carried out (50 PV) followed by the flooding of supercritical CO_2 (40 PV). The final flooding procedure was to inject the sample with supercritical CO2 containing brine, where x-ray micro-computed tomography images were taken during and after all flooding processes. It was concluded that good amounts of residual CO_2 were achieved in oil-wet rocks (13.5%), while the process of recovering oil was significantly improved (50% oil recovery) (Iglauer et al., 2019). Fang et al. (2019) used glass micromodels having three different permeability values (simulating Daqing Oilfield in China) to compare the effectiveness of oil recovery using four different flooding techniques (or fluids). To simulate the oil recovery, samples were injected with water, polymer surfactant, binary flooding, and binary flooding with polymer surfactant. It was observed that polymeric surfactant flooding resulted in the best oil recovery compared to the three other displacing fluids. Alhammadi et al. (2020) injected two carbonate rock samples with CO_2 and brine (200 PV) at controlled conditions then samples were untouched for three days. For two weeks, crude oil was introduced into the rock columns followed by eight fractional brine flows. X-ray micro-computed tomography images were captured for samples after each procedure. The procedure resulted in a large oil recovery percentage reaching 78.3%, keeping in mind that the oil saturation percentage at the start point was around 81.9% (Alhammadi et al., 2020). Liang et al. (2020) studied the effect on residual oil distribution after imbibition by constructing a glass micromodel having a pore size range between 50-400 micro-meter. The micro model (oil-wet) was first injected with kerosene then was injected with brine (0.2 PV). The same procedure was repeated on a second glass micromodel (water-wet). It was observed that the residual oil in the water-wet model was fourteen times less abundant

than the oil-wet model. Also, it was observed that a higher coordination number in micro-models resulted in decreased residual oil saturation.

2.3 Knowledge Gap

It was concluded that there is a lack of studies in correlating occupancy (of residual NAPL) in pores with respect to pore sizes for various real geological porous media and with respect to the coordination number of pores for various real geological porous media as well.

CHAPTER 3: METHODOLOGY

3.1 Materials and Sediments

The work in this chapter including all mentioned materials (section 3.1), the experimental setup (section 3.2), experimental procedure (section 3.3) and imaging parts (section 3.4) was conducted by (Al-Raoush, 2014). Data was used from that work for the analysis shown in here in this thesis. For the sake of clarifications, the details of the previous work and experiments are summarized below.

Fifteen soil samples were selected in the experiment to simulate unconsolidated porous sand media. Out of the total fifteen samples, six silica sand samples of different sizes were included in order to replicate rounded physical properties of the sand (D_{50} from 0.196mm to 0.433mm), while six quartz samples having different sizes were selected mainly to simulate angular shapes (D_{50} from 0.179mm to 0.431mm). The last three samples were a mix of silica sand and quartz sand (D_{50}= 0.252mm) (See Table 4. having mix ratios). All sand test samples were acquired from AGSCO Corporation in Wheeling, Illinois, USA. The selection of samples' sizes considered the representation of unit cell or representative elementary sample (REV).

In order to simulate NAPLs (or potential residual oil) in the test samples, Soltrol 220 oil was acquired from Chevron Philips Chemical Company representing the non-wetting phase inside the samples. After that, Iodobenzene (C_6H_5I) was added to Soltrol 220 oil to help in imaging contrast. On the other process, de-aired water was selected to represent the wetting phase, where Caesium chloride (CsCl) was added to help in imaging contrast. Despite the addition of doping agents, neither Iodobenzene nor Caesium chloride are expected to have a significant impact on the properties of the test fluids (Brusseau et al., 2007).

Table 4. List of porous medium used in the experiment with their physical properties.

Porous Medium	Porosity	D50 (mm)[a]	C_u[b]	C_c[c]	Ψ[d]	X_v[e]
Silica sand: S1	0.347	0.433	1.858	1.146	0.914	0.835
Silica sand: S2	0.375	0.352	1.847	1.118	0.903	0.827
Silica sand: S3	0.338	0.271	1.793	1.059	0.89	0.815
Silica sand: S4	0.359	0.267	1.794	1.068	0.888	0.812
Silica sand: S5	0.325	0.258	1.831	1.004	0.89	0.815
Silica sand: S6	0.383	0.196	1.524	1.086	0.883	0.807
Quartz sand: Q1	0.457	0.431	1.443	0.939	0.809	0.715
Quartz sand: Q2	0.455	0.276	2.494	1.062	0.815	0.725
Quartz sand: Q3	0.451	0.237	1.953	1.074	0.818	0.714
Quartz sand: Q4	0.450	0.233	2.144	1.076	0.813	0.725
Quartz sand: Q5	0.458	0.213	1.976	1.006	0.825	0.738
Quartz sand: Q6	0.456	0.179	1.720	1.059	0.813	0.727
Mixed: M1	0.409	0.298	2.461	1.064	0.842	0.757
Mixed: M2	0.420	0.252	1.959	1.094	0.852	0.772
Mixed: M3	0.420	0.244	1.890	1.000	0.800	0.950

Note. [a]Data is from (Al-Raoush, 2014), [b] C_u: Uniformity coefficient = D_{60} / D_{10}, [c] C_c: Coefficient of gradation = $D_{30}^2 / (D_{60} * D_{10})$,[d] Sphericity index, and [e]Roundness index.

3.2 Experimental Setup

With the aim of containing the fifteen sand samples, x-ray transparent aluminum columns having a length of 85mm, an inner diameter of 6.17mm, and a column wall thickness of 0.3mm were used. Additionally, hydrophobic filters were installed at both ends of the aluminum columns to confine the sand samples inside the columns as well as controlling the ingoing and outgoing fluid flow. Hydrophobic filters were acquired from Applied Separations Incorporation in Pennsylvania, USA (20μm) and Alltech Associates Incorporation in Chicago, USA (2μm). Two stainless steel compression adaptors were connected to the aluminum columns, one from the top side, and the second adaptor was connected from the bottom side. A syringe pump (Cole-Parmer Series 74900-10 syringe pump) was connected to the topside compression adaptor having another connection with a 3-port stainless steel valve equipped with

compression fittings to adjust the flow path. A similar setup was carried out to the bottom of the aluminum columns, except that the bottom side had a compression adaptor connected to a scanning station support (movable plate used to capture x-ray scans from all directions) (see Figure 2.)/ (Al-Raoush, 2014).

3.3 Experimental Procedure

- All sand samples (silica and quartz) were cleaned using distilled water.
- All sand samples went through 24 hours drying process inside an oven.
- Nitric acid was applied to sand samples to remove any remaining impurities.
- The final cleaning process was to wash the sand samples with distilled water.
- Six silica sand samples having different sizes were set up (S1 to S6).
- Six quartz sand samples having different sizes were set up (Q1 to Q6).
- Three mixed samples were set up having quartz (50%) and silica (50%) mixes with different sizes (M1 to M3).
- 8% by volume of Iodobenzene (C_6H_5I) was added to Soltrol 220.
- Soltrol 220 was dyed in red using “Oil Red O” acquired from Sigma-Aldrich Chemical Company in St. Louis, Missouri, USA.
- Dry sand samples were packed in the aluminum columns to have an equivalent sand grain distribution.
- De-aired water imbibition took place from the bottom side of the columns (upwards flow) at a flow rate of 4.07ml/hr.
- Low capillary number flow was carried out for all columns’ experiments ($C_a = 1\times10^{-6}$).

- Soltrol 220 oil was injected from the bottom side of the columns (upwards flow) at a flow rate of 4.07ml/hr.
- De-aired water was injected from the bottom side to sweep the soltrol 220 oil (whatever remains is the residual oil).
- The experiment was conducted at a room temperature of 23º C.

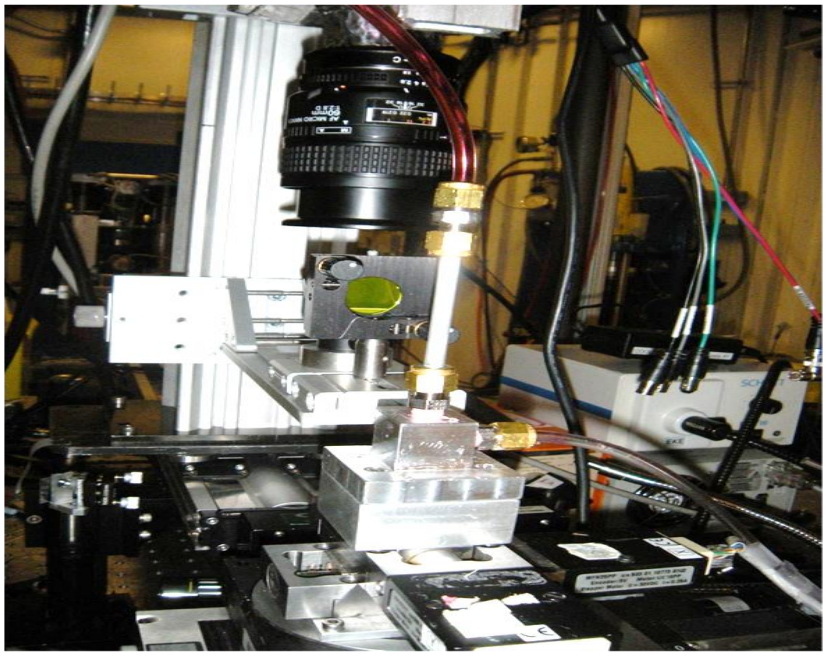

Figure 2. Image of the Experimental Setup for the Aluminum Column (R. I. Al-Raoush, 2014).

3.4 Imaging

X-ray micro-computed tomography images were taken at the Argonne National Laboratory, Illinois, USA, using beamline number 13-BM-D. Radiographs of the samples' cross-sections were used to build volume images with the help of GSECARS, The University of Chicago codes, where the samples' boundary effects were eliminated by taking the scans at the center of each sample column. X-ray scans returned images having a Voxel resolution of 9.6 μm and an image size of 690x690x1000 Voxel (Al-Raoush, 2014).

CHAPTER 4: ANALYSIS

4.1 Image Analysis

4.1.1 Median Filter Process

The median filter has the main aim of reducing the black and white noises in images as well as attenuating higher frequencies to increase image contrast. Thus, each physical material in an image has its unique high-frequency interval (Pratt, 2013; Brownrigg, 1984; Sun & Neuvo, 1994). A typical two-dimensional (picture element, **pixel**), is present in a grid arrangement of nine boxes, a box at the center that is surrounded by 8 neighboring boxes, where each box represents a single pixel value. However, **vo**lume **el**ements (**vo**x**el**s) of three-dimensional images are present in a spatial grid of twenty-seven boxes, the central voxel, and the neighboring 26 voxels, where each box has a voxel value. The mechanism of a median filter works by selecting the value of a middlebox of either two-dimensional or three-dimensional images. After that, all neighboring boxes' values (in contact with the middlebox see Figure 3. for better visualization), are taken and reordered from smallest values to largest values (including the value of the middlebox). Finally, the median (middle) value is assigned for the middle box in the new filtered image.

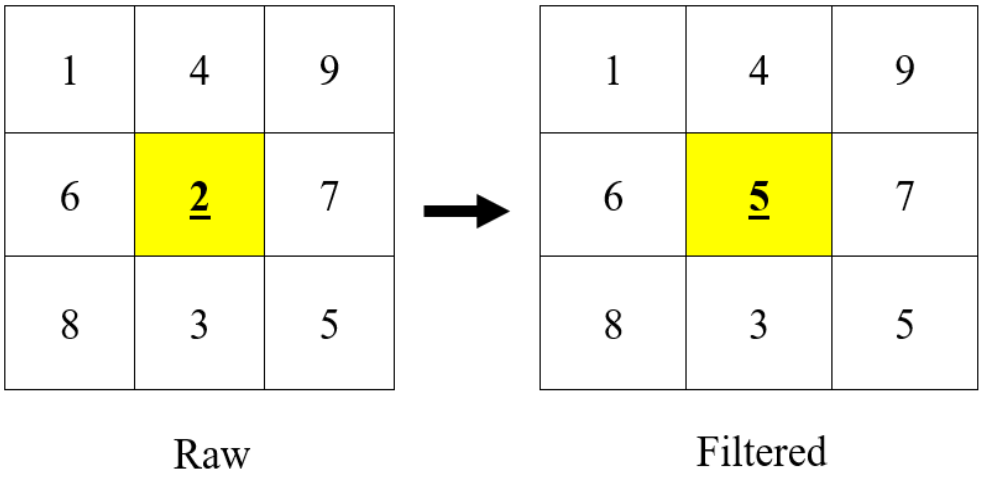

Figure 3. Median Filter Mechanism for a 2D Image.

After applying the median filter to the raw images, the black and white noise elements are eliminated. A notable increase in the contrast of different materials is achieved. Figure 4. shows the histogram of an image after median filtration. The first peak (at the left side of the image) represents the increase in voxels' frequencies for the de-aired water phase. While the middle peak represents a high number of voxels for the sand phase (the most frequent material by volume in all images). The last peak (at the right side of the image) shows the voxels corresponding to the oil phase. Going from left to right, the water phase has a CT Number (voxel brightness) ranging between -400 to -100. Where the sand phase has a CT Number ranging between -100 to 2000. The rightmost peak representing oil has a CT Number ranging between 2000 to 4000. It is noted that the oil phase naturally has a lower CT Number than sand, but to increase the contrast of oil; a doping agent (Iodobenzene) was mixed with the oil to increase its brightness in the x-ray images. Thus, offsetting the CT Number range behind that of sand, to facilitate segmentation with enhanced accuracy and computational efficiency (more on that below).

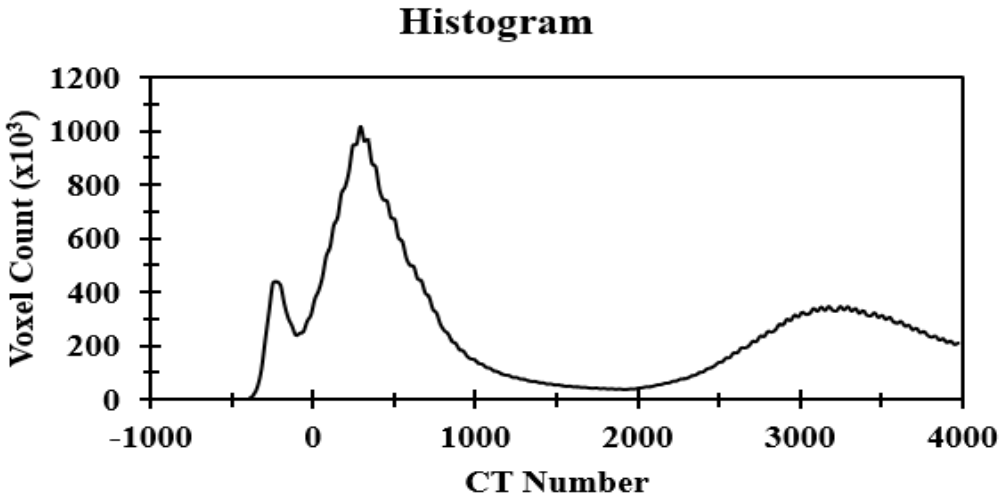

Figure 4. Sample Image Histogram.

4.1.2 Segmentation

After acquiring raw x-ray micro-computed tomography images, the first step was to segment the images. The main target for the process of segmentation is to allocate values for all regions in an image, where such values will represent the different material phases (NAPL, de-aired water, and sand in this experiment). Even though several automated methods which have the ability to segment a raw image are available, manual segmentation was carried out in the research paper in order to assure more accurate value allocation. Hounsfield scale or computed tomography number was given to the grey-scale images to giving an interval for each medium. Using PerGeos Software, the sand medium was assigned to the high computed tomography number of scans below the KI edge at 2000, while NAPL was assigned to computed tomography numbers range above the KI edge. De-aired water was assigned to the remaining low computed tomography number range. A slim range falling between sand and de-aired water was used to detect air in the sample image (see Figure 5. for examples of segmented samples).

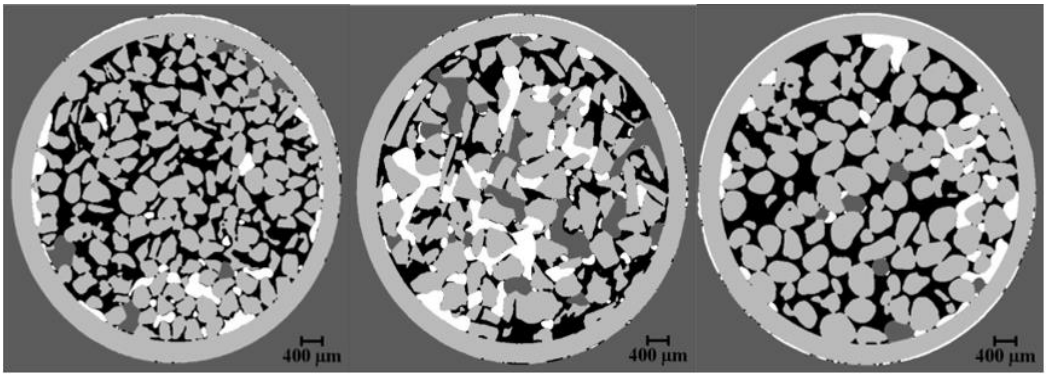

(a) (b) (c)

Figure 5. Segmented Images of Mixed Sample M1 (a), Quartz Sample Q1 (b), and Silica Sand Sample S1 (c).

4.1.2.1 De-Aired Water Segmentation

After acquiring raw x-ray micro-computed tomography images, the following step after filtering (median) was to segment the images. CT Numbers of the voxels in the three-dimensional x-ray images were used to convert the x-ray grey scale values to meaningful information that represents the special location of each material in the image volume. Visual observation along with the histogram of the three-dimensional image was used to select threshold values to separate each phase. For water, CT Number thresholds were greater or equal to -400 to less or equal than -100 were re-assigned as water phase. That selected range was transferred to a new three-dimensional image that has the label of water, which is equal to one. The new image reconstructs a micron-resolution model of the water located in the image volume (see Figure 6.).

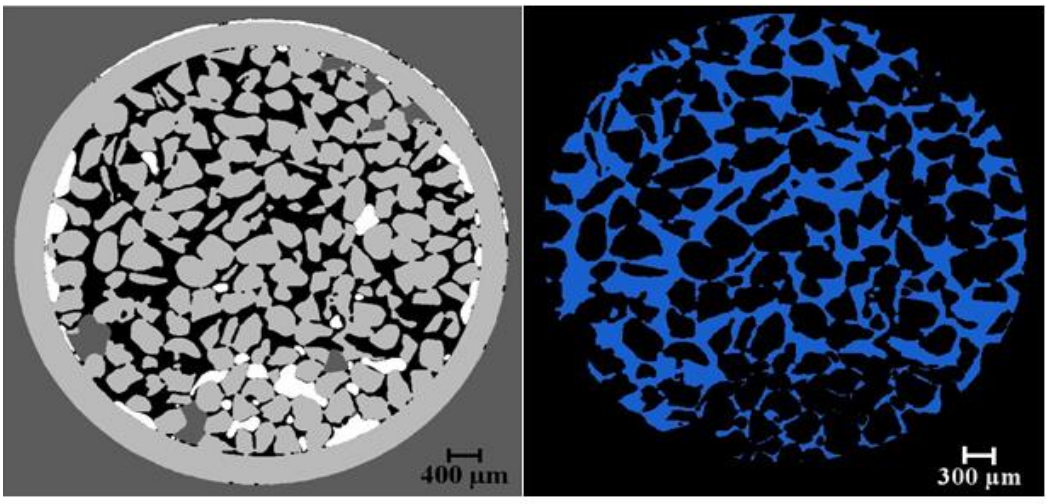

Figure 6. Segmented Image of De-aired Water (b) of Mix Sample M1.

4.1.2.2 Residual NAPL Segmentation

Similarly, the oil phase was extracted from the three-dimensional filtered scans. The segmentation of NAPL was carried out by selecting a threshold range (of greyscale image) with a CT Number greater or equal to 2000 and a voxel CT Number less or equal to 4000. Voxels in that CT number range were allocated in a new labeled image and were given a voxel value of four. The new labeled image reconstructs the volume, shape, and location of residual NAPL blobs within image volume (shown in Figure 7.).

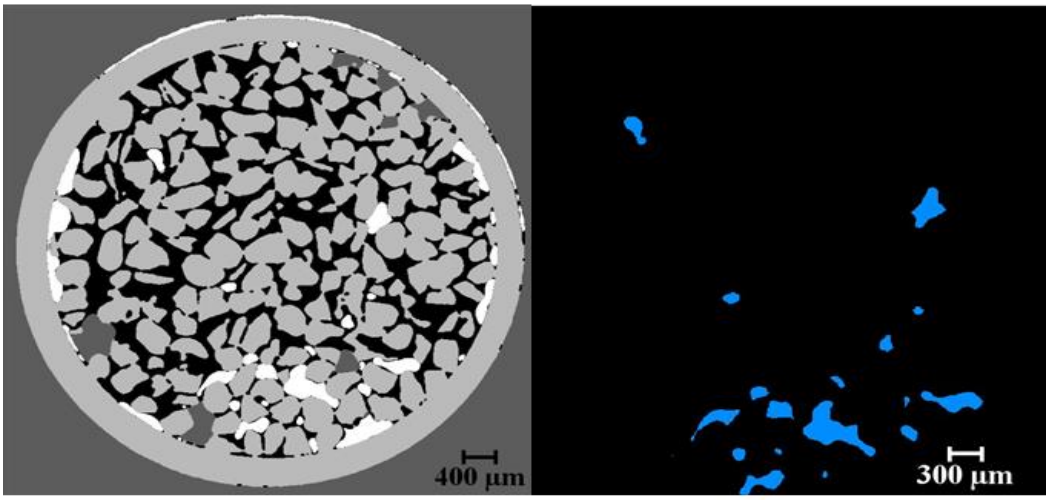

(a) (b)

Figure 7. Segmented Image of Residual NAPL (b) of Mix Sample M1.

4.1.2.3 Sand Segmentation

Likewise, the sand media was acquired from the three-dimensional filtered scans. The segmentation of sand was carried out by selecting a threshold range having a CT Number greater than -100 and a voxel CT Number less than 2000. Voxels in that CT number range were allocated in a new labeled image and were given a voxel value of three. The location of solids in the labeled image represents the solid content in the porous media, where liquids flow around (see Figure8.).

4.1.2.4 Air Segmentation

Finally, the entrapped air was segmented from the three-dimensional filtered images. The segmentation of air was achieved by selecting a threshold range having a CT Number less than -400. Voxels in that CT number range were allocated in a new labeled image and were given a voxel value of two (see Figure9.).

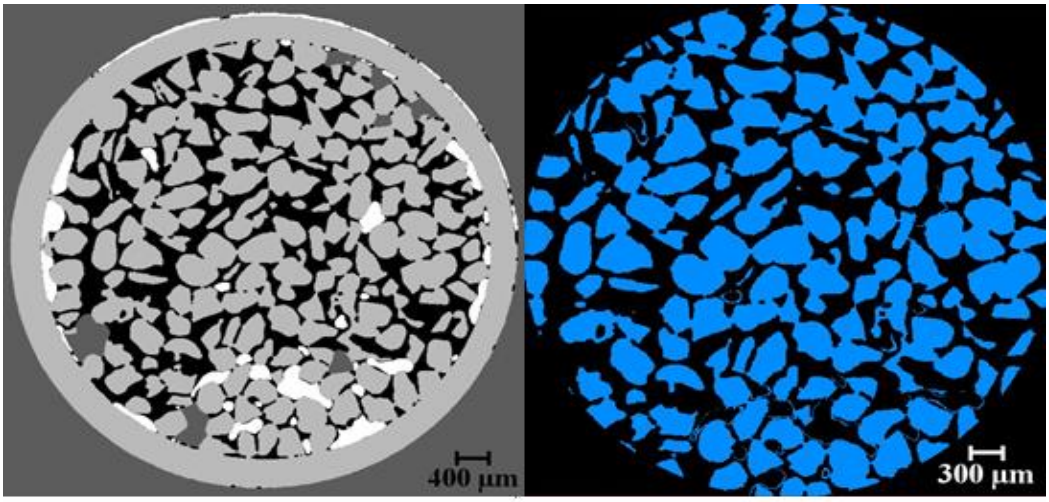

(a) (b)

Figure 8. Segmented Image of Sand (b) of Mix Sample M1.

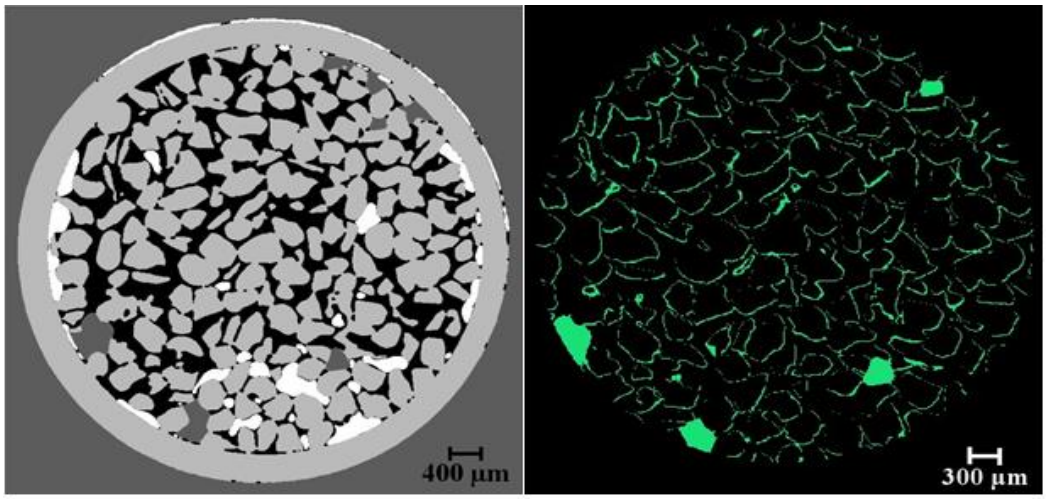

(a) (b)

Figure 9. Segmented Image of Air (b) of Mix Sample M1.

4.2 Pore Network Analysis

The modeling of pore networks is a difficult task, mainly due to the geometrical complexity of voids. So, in a typical pore network model, perfect spheres are used to represent void spaces that are connected together with tubes that simulate pore throats forming a complete system, where the transport of the system's fluids (NAPL, de-aired water, and air in this experiment) occur. The use of simple spherical and cylindrical tube shapes to represent a pore model is justified by the fact that fluids movement at the pore scale is governed by the capillary pressure. Which in terms is governed by the pore-throat radius where a fluid is heading to. Moreover, such a method is efficient in terms of system connectivity representation.

4.2.1 Grain-Based Algorithm

The used algorithm takes the center points of all voids as the starting point, where the algorithm draws lines through all void centerlines creating a network (using samples' 3D binarized images). The algorithm recognizes a pore when more than one line meet at the same point (junction). Thus, a throat is recognized as a line that passes between two junctions. The line width increases till coming into contact with grains from all directions, which defines the radius of the junction (pore) or the throat. The algorithm automatically selects the minimum radius, that will simulate the flow through pores and throats driven by capillary pressure (see Equation 1.). Despite the fact that there are several algorithms used to construct pore network models such as Medial Axis (Al-Raoush & Willson, 2005), Maximum Ball (Al-Kharusi & Blunt, 2007), Statical Approach, and Mercury intrusion test (Xiong et al., 2016), grain-based maximal balls algorithms remain the most accurate models in constructing a pore network made of sand samples (Al-Raoush et al., 2019; Bakke & ØRen, 2002).

$$P_c = \frac{2\sigma \cos\theta}{R}$$ Equation 1. Capillary Pressure Equation

CHAPTER 5: RESULTS AND DISCUSSION

5.1 3D and 2D Images

Two-dimension cross-sectional images taken from the three-dimensional computed tomography scans of silica sand samples clearly show the distinctive color labeling for each material phase (see Figure 10.). When looking at the sand grains (yellow label), the physical properties of silica sand are identified mainly due to the roundness of sand grains. Also, the different sizes between the six silica sand samples are clear, where sample S1 has the largest average diameter (D_{50} = 0.43mm) and sample S4 has the lowest average diameter (D_{50} = 0.19mm). Other mediums such as water (labeled in blue), residual NAPL (labeled in red), and air (labeled in green) are identified in the system images for silica sand. Silica systems with larger average grain diameters tend to have large residual NAPL ganglia, while systems with smaller average grain diameters tend to have clusters of NAPL residuals.

Likewise, two-dimension cross-sectional images of quartz sand samples clearly show the unique color labeling for each medium phase (see Figure 11.). Color labeling for different materials in quartz sand was similar to silica sand (grains is yellow, water is blue, residual NAPL is red, and the air is green). Physical properties of quartz sand are shown in the two-dimensional images, where the quartz's grains angularity appears. Quartz sand samples have larger average porosity values (0.478) than silica sand (0.348). Similar to silica sand, quartz sand with larger average grain diameters had residual NAPL ganglia, while systems with smaller average grain diameters had smaller clusters of NAPL residuals.

The three mixed sample images (See Table 4. for mixing ratios) show the mixed physical properties of both silica sand (rounded) and quartz sand (angular) (see Figure 12.). Color labeling of different phases in the mixed sand packs was similar to silica

and quartz sand (grains is yellow, water is blue, residual NAPL is red, and the air is green). Sample M3 has the lowest average grain diameter (D_{50} = 0.230mm), while sample M1 has the largest average grain diameter (D_{50} = 0.298mm). The average porosity for the mixed samples falls between the silica and quarts sand at a value of 0.400.

The silica sand pore network models (see Figure 13. and Figure 14.) acquired from the three-dimensional computed tomography images represent the pore space by spheres and the throats by cylinders. The three-dimensional pore networks do have color gradients representing the pore radius sizes (red color returns a large pore or throat radius). The three-dimensional pore network model confirms the average radius sizes for silica sand. For example, it was stated that sample S1 has the largest average diameter (D_{50} = 0.433mm). So, by looking at sample S1 pore network model, the red color gradient is clearly dominant (representing pore radiuses larger than 90µm). Moreover, by inspecting silica sand three-dimensional pore network models, larger connected voids are observed in samples having large average pore radiuses in comparison with samples having small average radiuses. That confirms the observations from the two-dimensional scans, where it was observed that residual NAPL ganglia shapes were dominant in silica systems with larger average grain diameters, and cluster NAPL residuals were dominant in systems with smaller average grain diameters. Similar results were observed from the quartz and mixed sand samples' three-dimensional pore network models (see Figure 15., Figure 16., and Figure 17.). However, a larger number of voids were detected when scanning the three-dimensional pore network models of quartz sand and mixed sand samples, which can promote the storage of NAPLs. Especially, branched and doublets shapes of residual NAPL (will be determined in the ganglia label section).

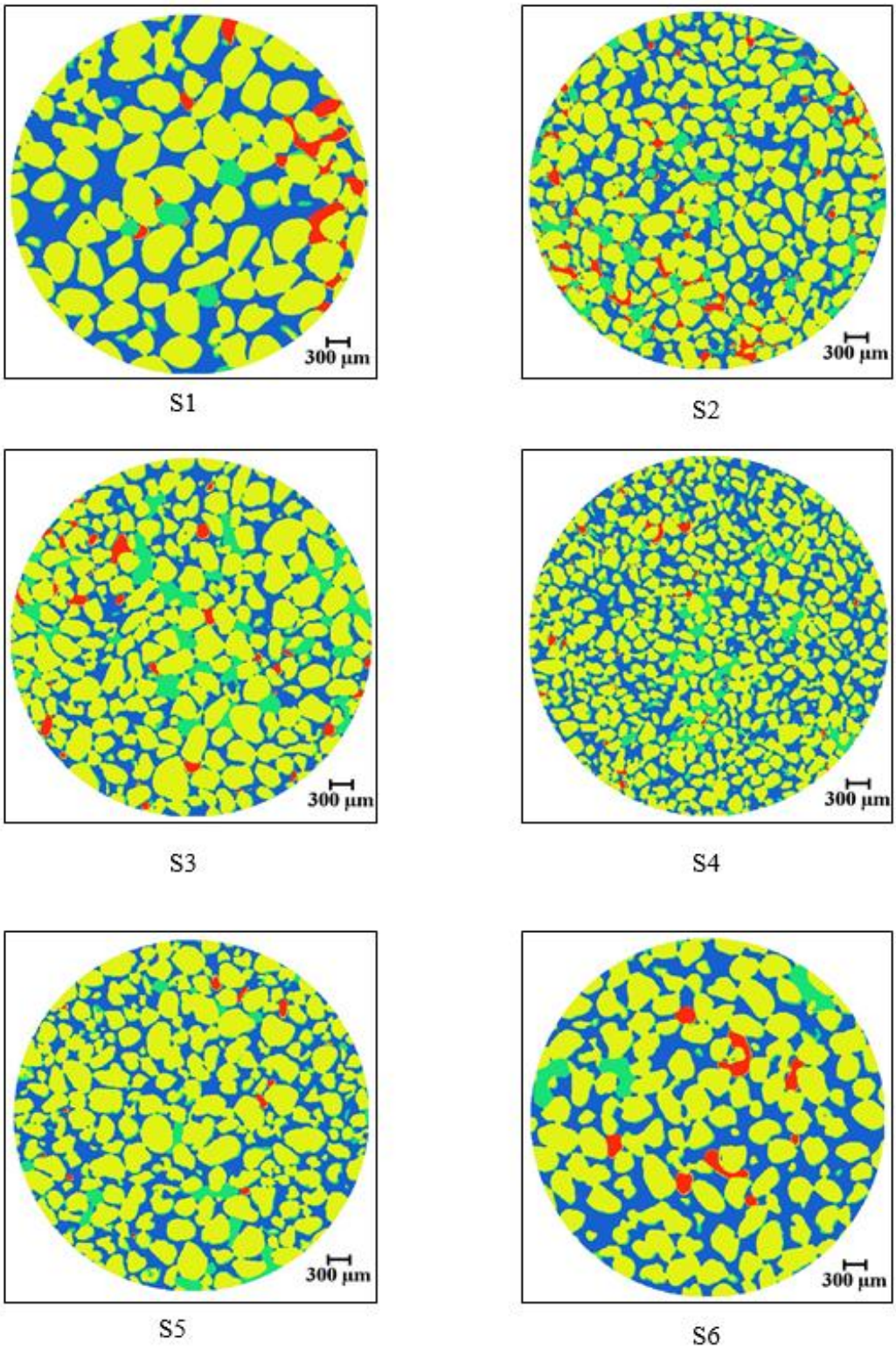

Figure 10. 2D Labeled Images of All Silica Sand Samples.

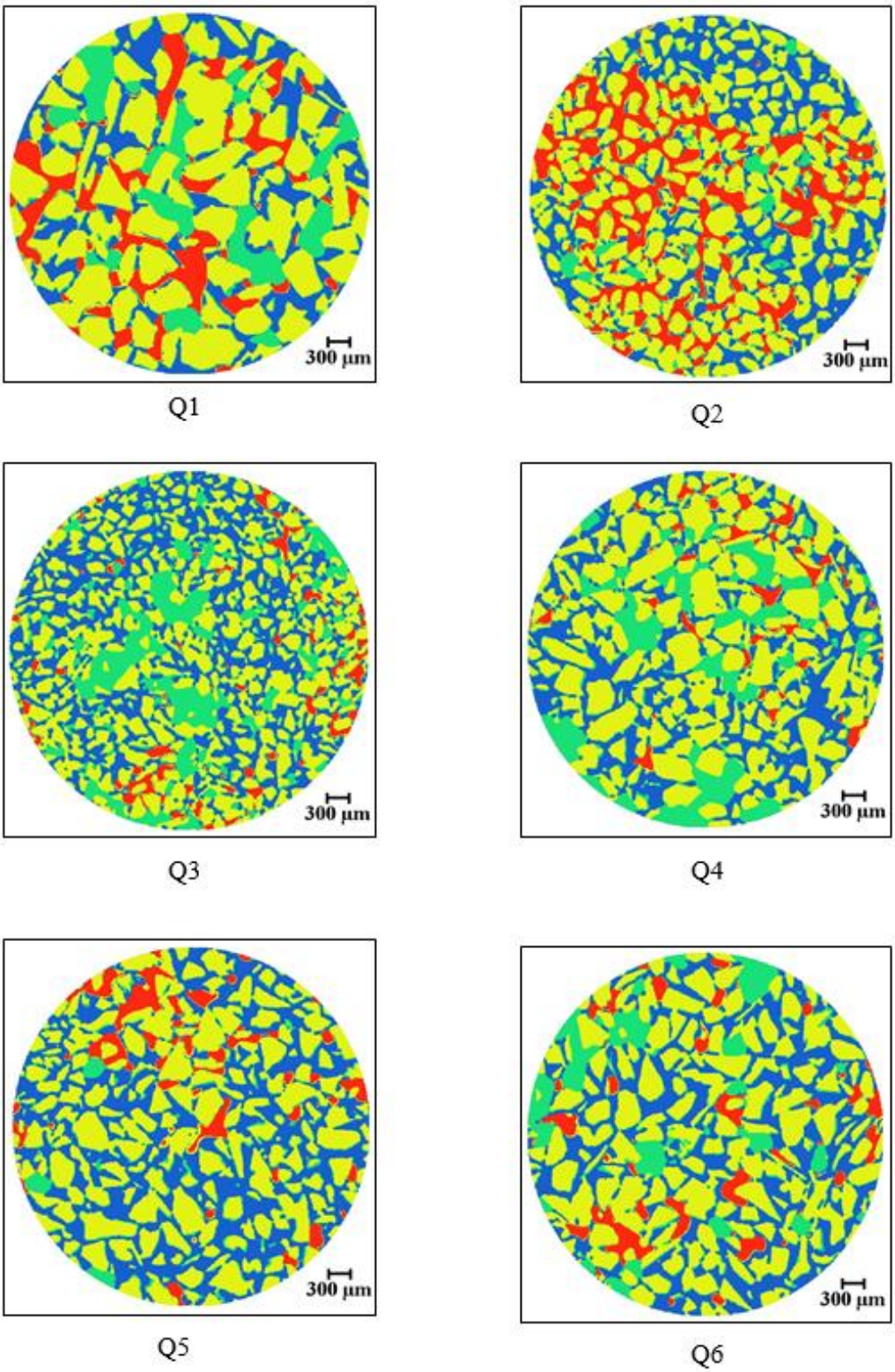

Figure 11. 2D Labeled Images of All Quartz Sand Samples.

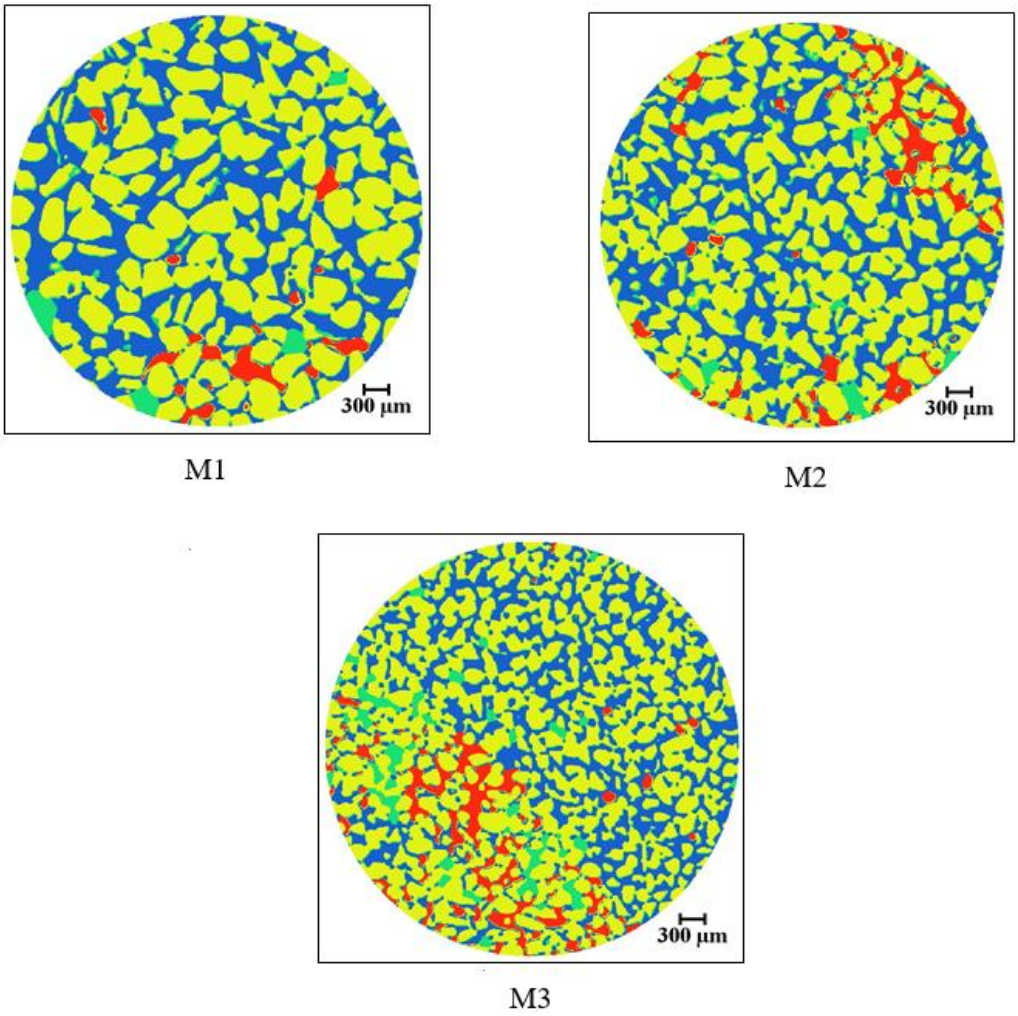

Figure 12. 2D Labeled Images of All Mixed Sand Samples.

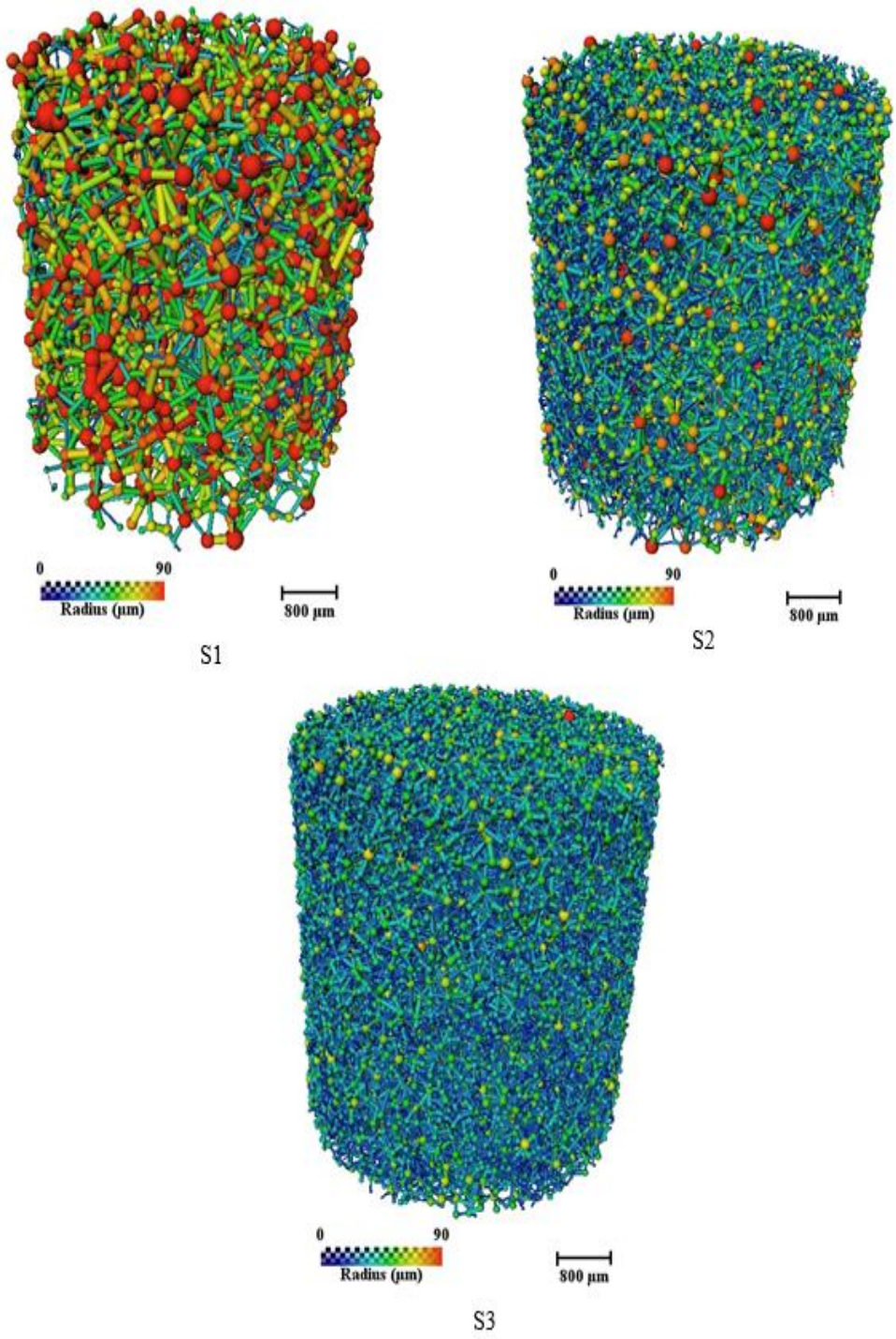

Figure 13. 3D Pore Network Images for Silica Sand Samples S1-S3.

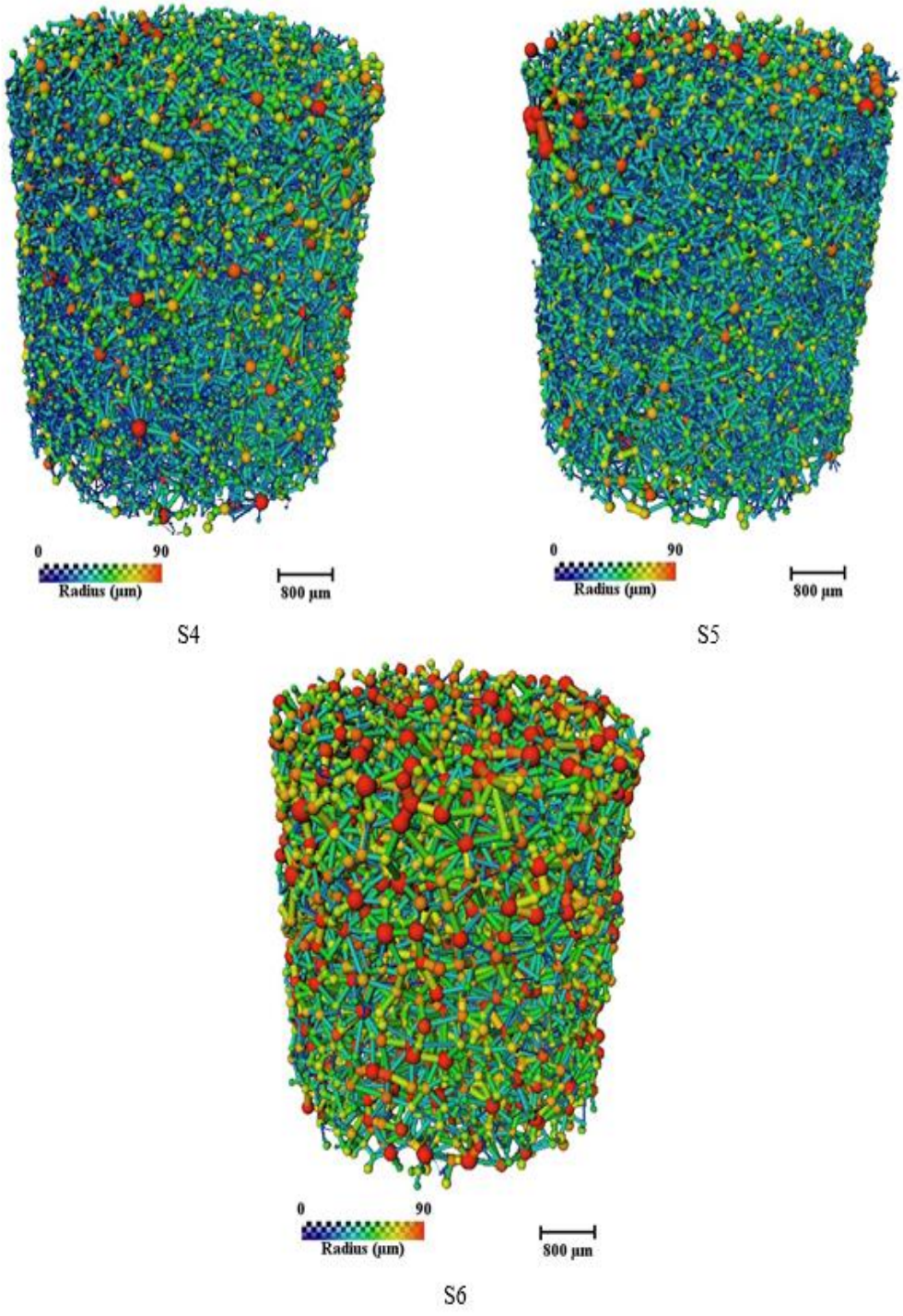

Figure 14. 3D Pore Network Images for Silica Sand Samples S4-S6.

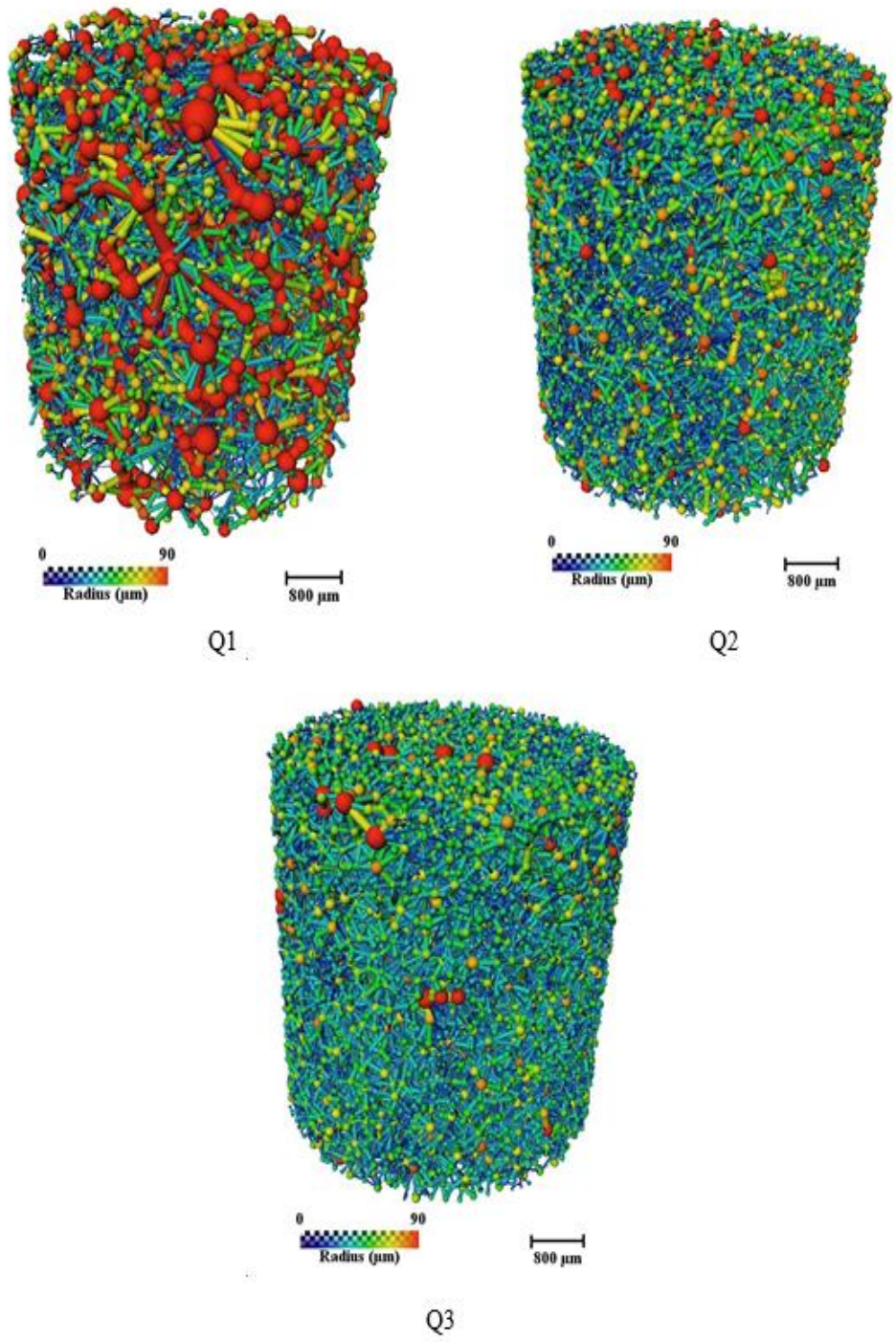

Figure 15. 3D Pore Network Images for Quartz Sand Samples Q1-Q3.

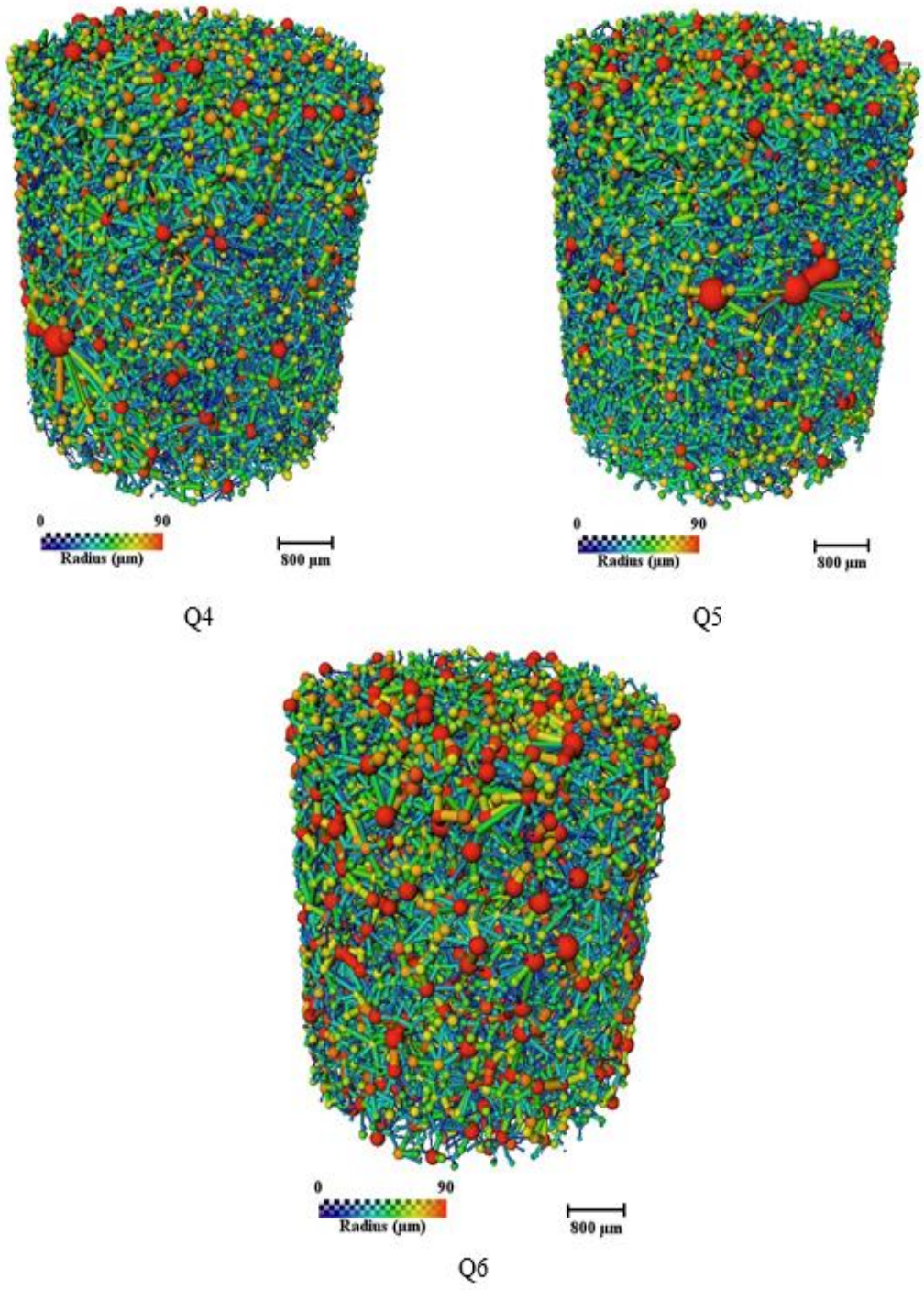

Figure 16. 3D Pore Network Images for Quartz Sand Samples Q4-Q6.

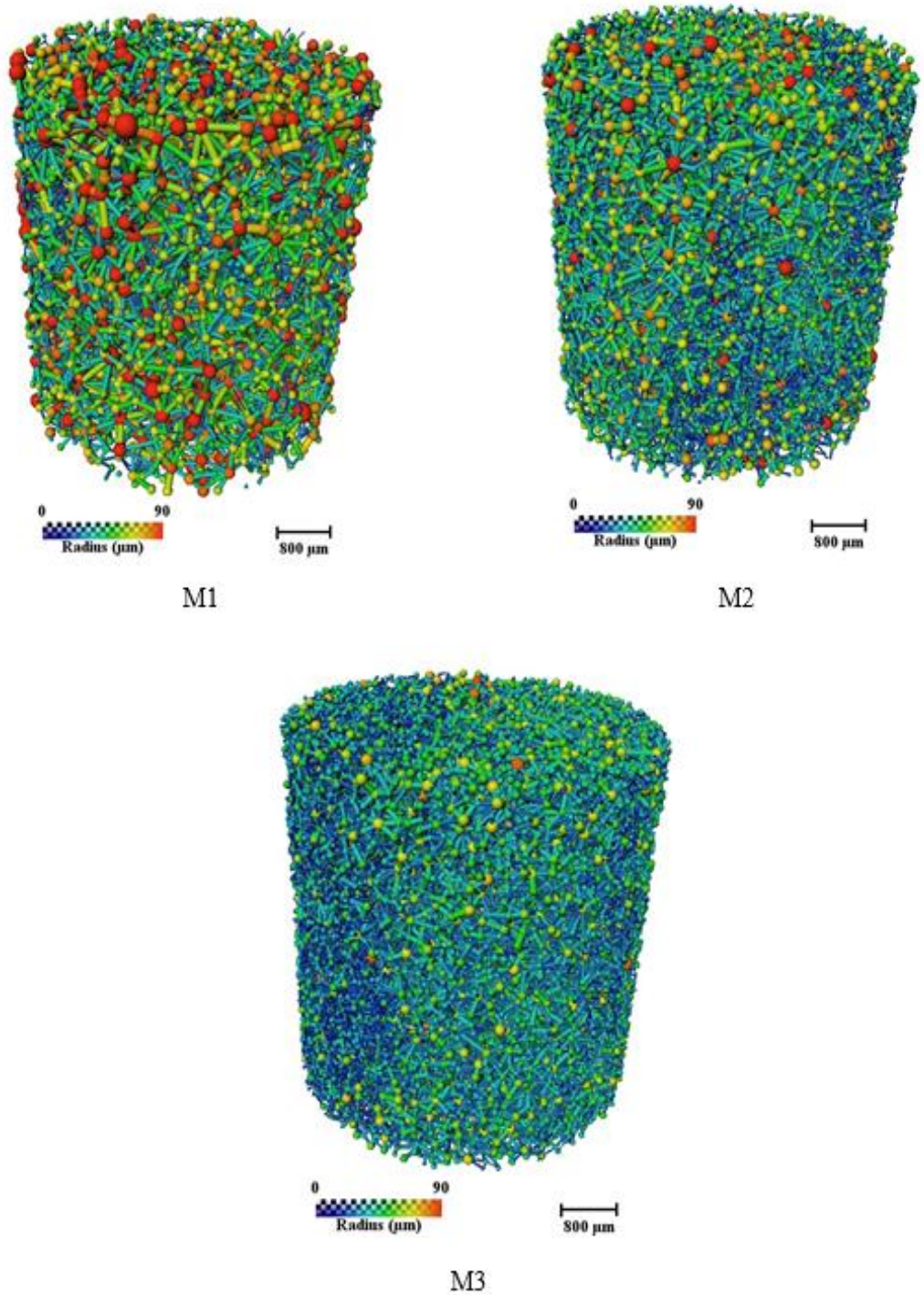

Figure 17. 3D Pore Network Images for Mixed Sand Samples M1-M3.

5.2 Sand Labeled Grain Images

The silica sand two-dimensional cross-section images (see Figure 18.) give detailed visualization of the silica sand shapes, where each individual grain was labeled with a distinctive color. The first physical feature that appears on silica sand is its grain sphericity, where all six silica samples have an average sphericity index value of 0.895 having a maximum value of 0.914 that appears in silica sand samples S1 (closest to 1). The high sphericity characterization in silica can be better visualized when going through the three-dimensional scans (seen in Figure 21. and Figure 22.). The roundness of silica sand can also be observed from the two and three-dimensional scans, where the silica sand samples have a high average roundness value of 0.819 with a maximum roundness value of 0.835 in sample S1.

The quartz sand labeled two-dimensional cross-sections scans (see Figure 19.) do show different physical properties in comparison with silica sand samples, where quartz grains are characterized with high angularity and sharp edges. That is confirmed by the average sphericity value of quartz sand (0.816) with the highest sphericity index value of 0.825 occurring at sample Q5. Figure 23. and Figure 24. demonstrate the high angular properties along with the sharp edges in quartz. The average roundness index value in quartz sand was also lower (0.724) than the roundness index value in silica sand. That confirms the differences in grain properties visualized from the two and three-dimensional images.

The three mixed samples of two and three-dimensional labels show the properties of both silica and quartz sand scans (see Figure 20. and Figure 25.) due to their mixing ratios (see Table 4.). The average value of the sphericity index (0.849) and the average value of the roundness index (0.767) for the mixed samples fall in between \ silica and quartz samples mainly due to their equal contribution in the mix (50% each).

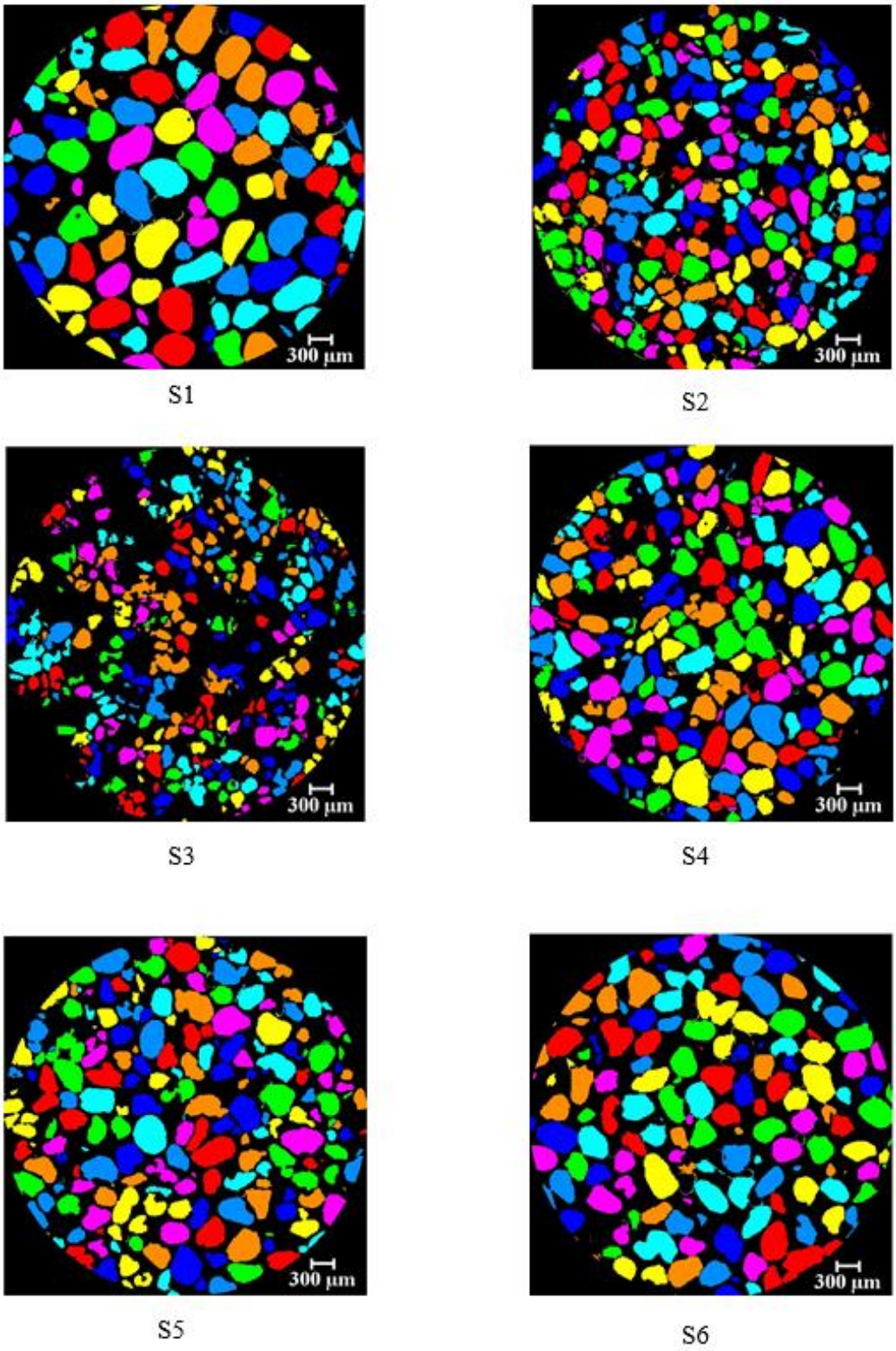

Figure 18. 2D Labeled Silica Sand Grains.

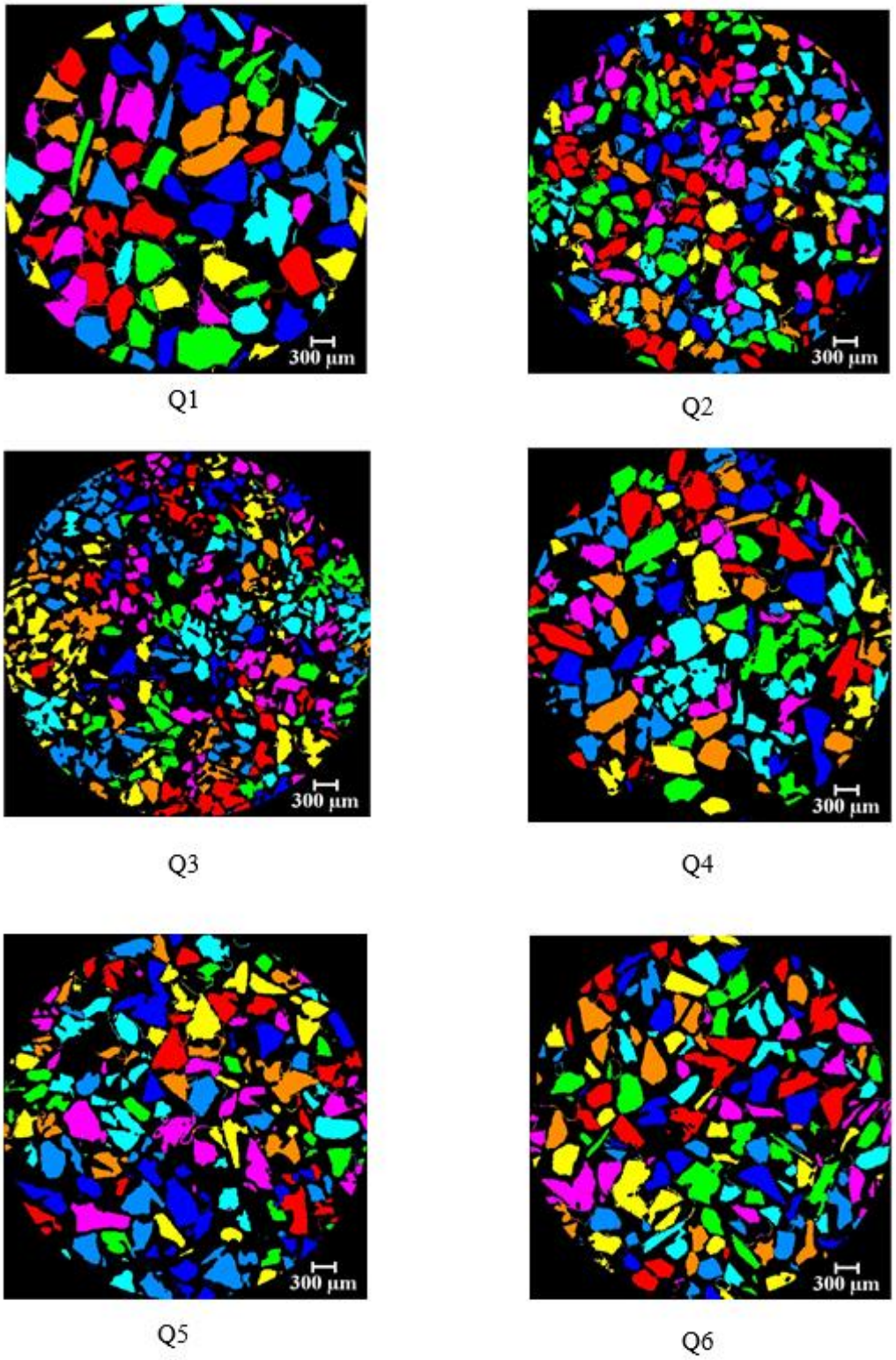

Figure 19. 2D Labeled Quartz Sand Grains.

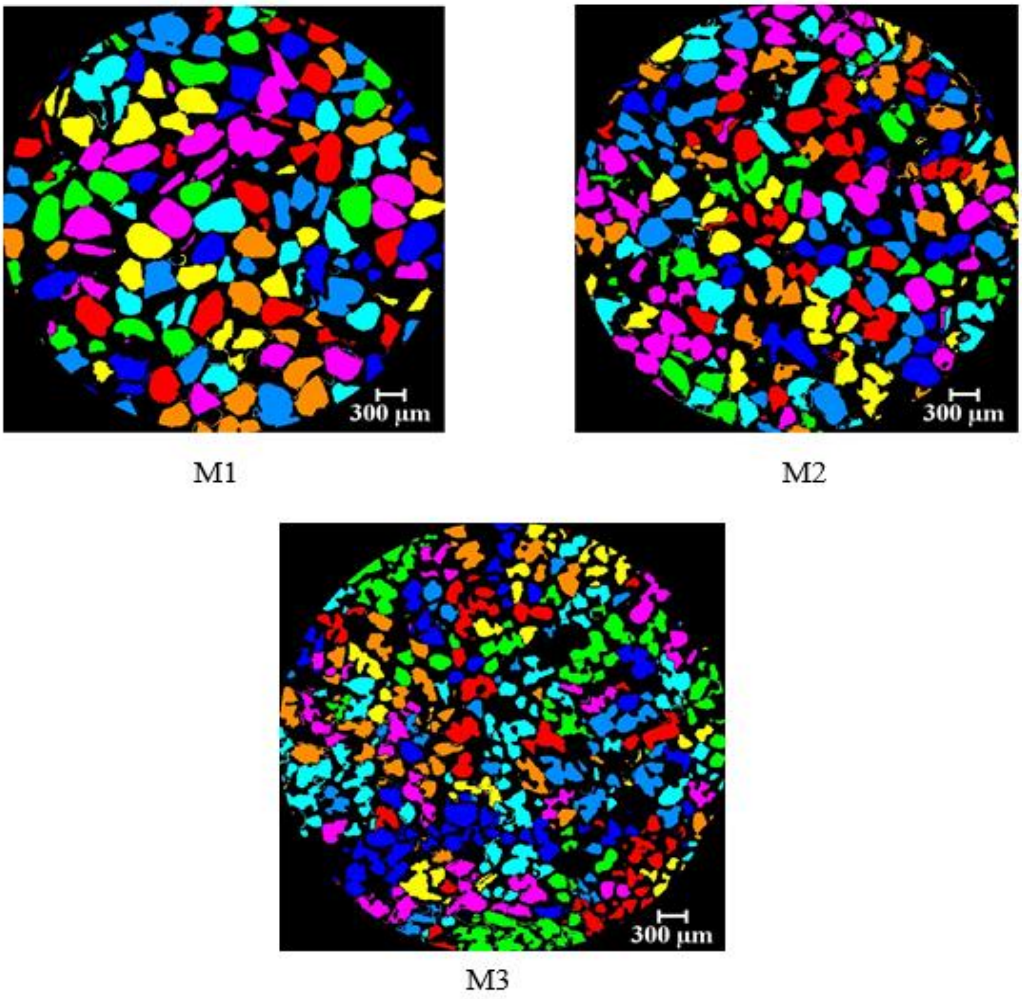

Figure 20. 2D Labeled Mixed Sand Grains.

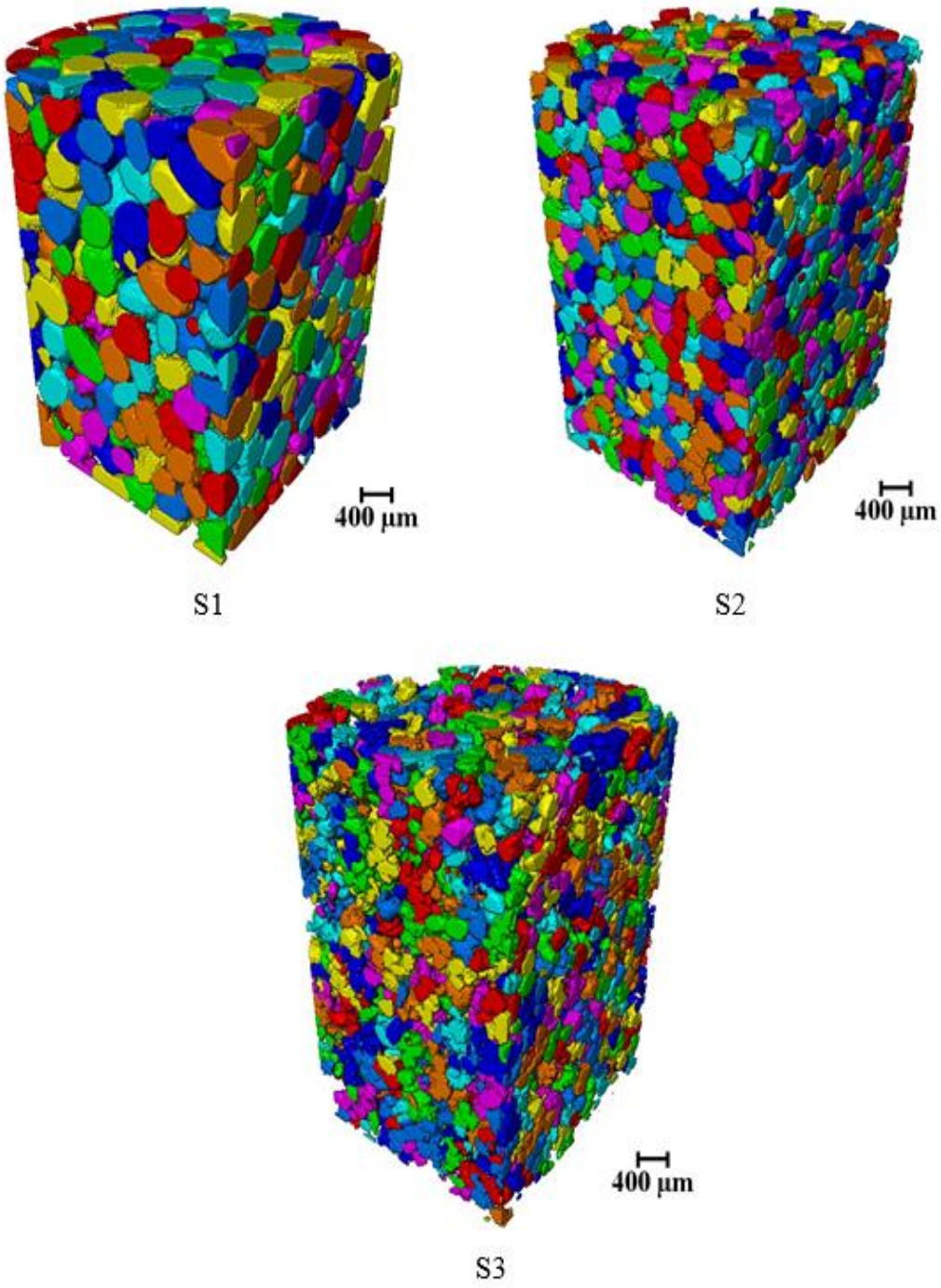

Figure 21. 3D Labeled Silica Sand Grains S1-S3.

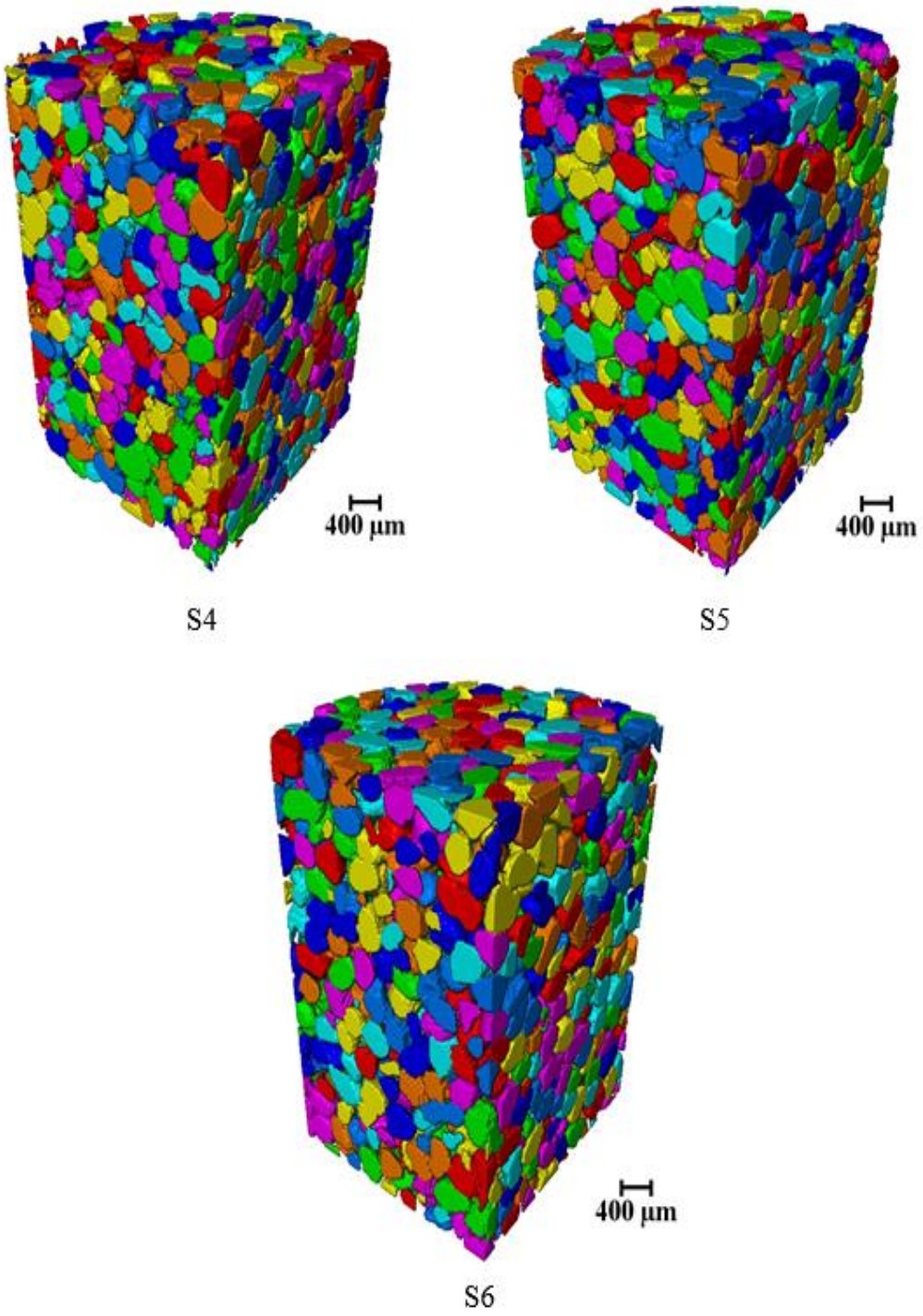

Figure 22. 3D Labeled Silica Sand Grains S4-S6.

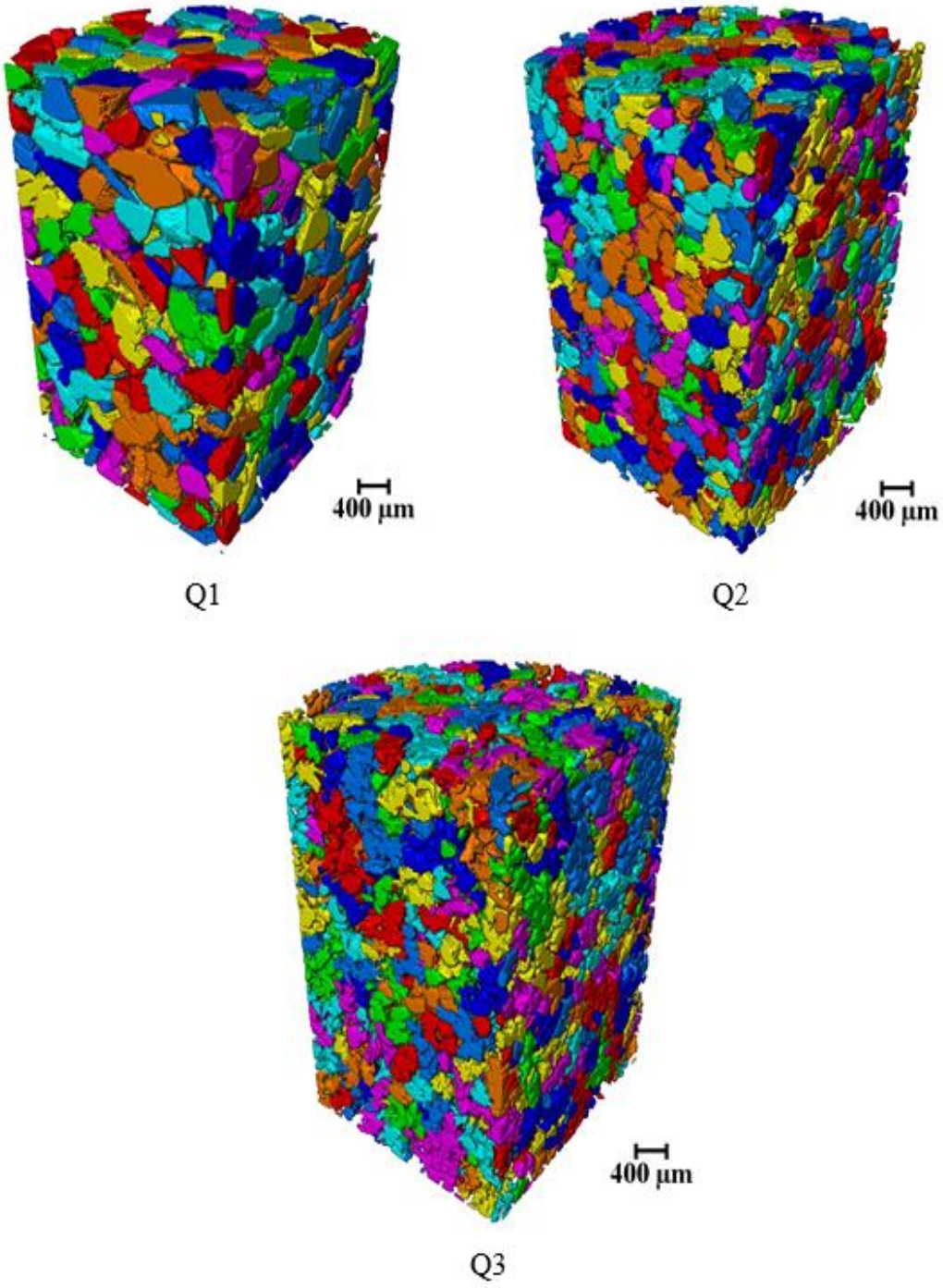

Figure 23. 3D Labeled Quartz Sand Grains Q1-Q3.

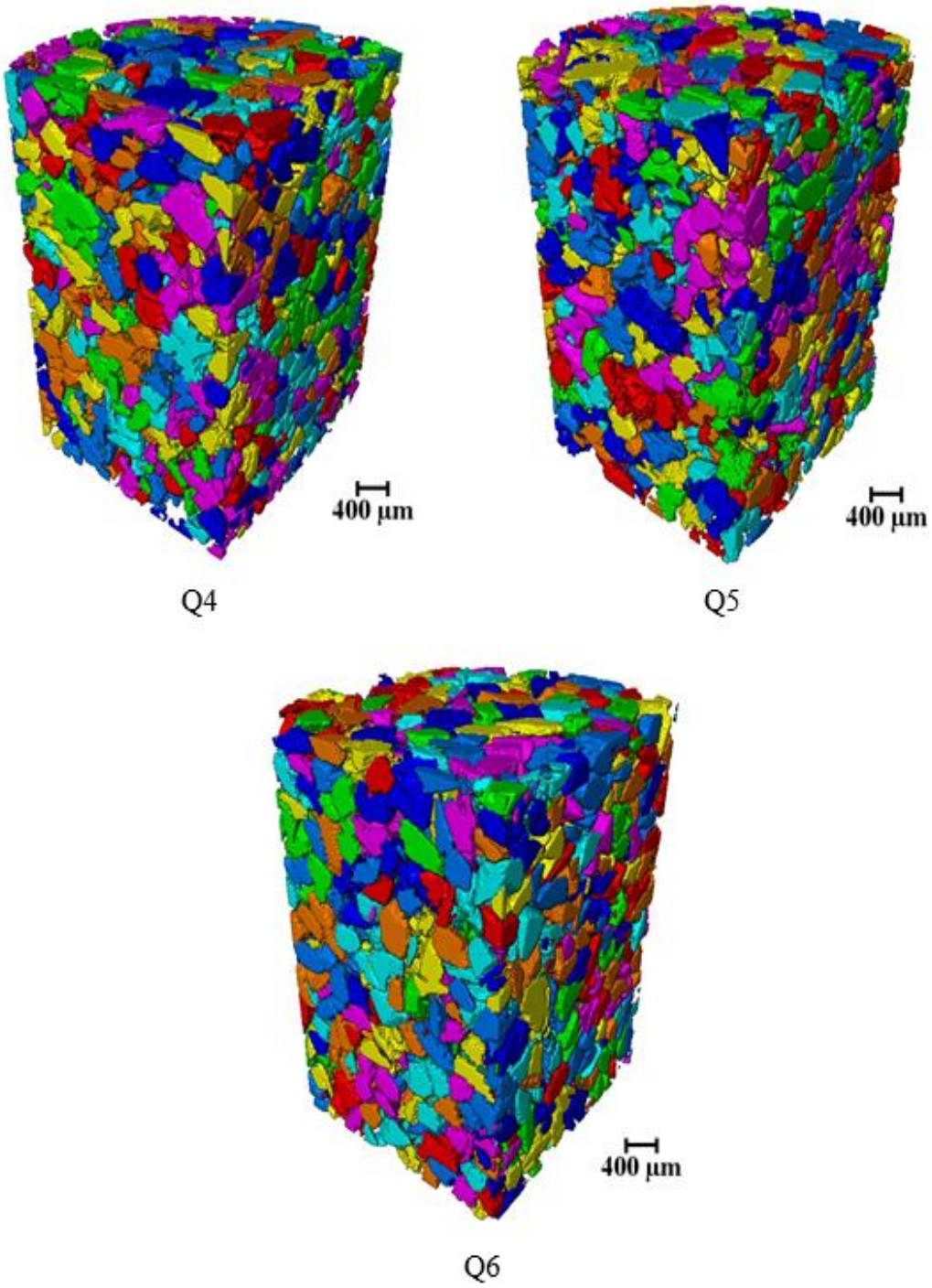

Figure 24. 3D Labeled Quartz Sand Grains Q4-Q6.

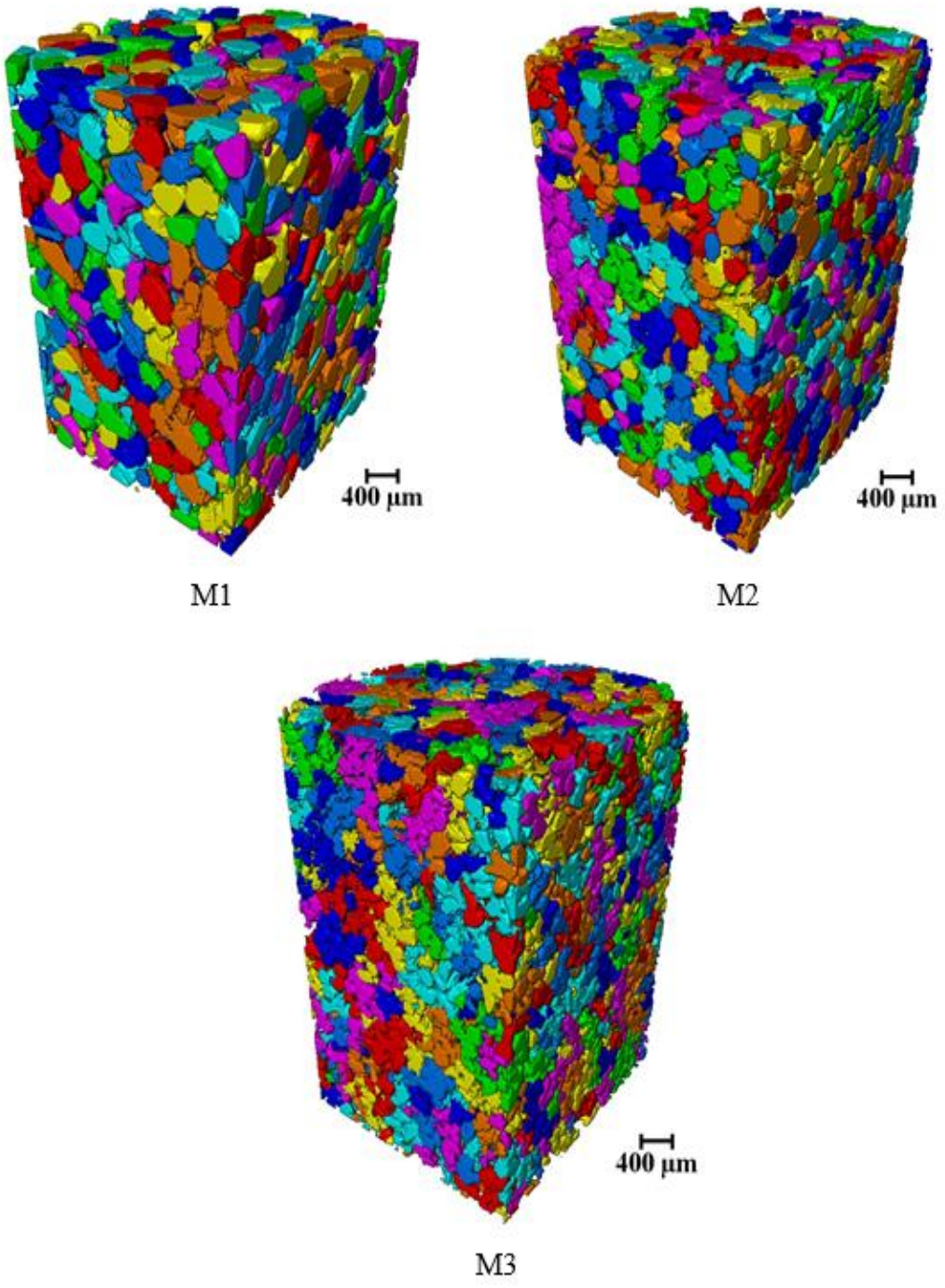

Figure 25. 3D Labeled Mixed Sand Grains M1-M3.

5.3 Ganglia Labeled Images

The silica sand two-dimensional cross-sections do only represent residual oil blobs (NAPL), where each separate blob was given a unique color (see Figure 26.). The two-dimensional cross-section images reveal that residual oil stored in silica sand samples are mainly taking the shapes of individual clusters rather than connected ganglia except for samples S1 and S6. Samples S1 and S6 do have one element in common which is the large average grain diameters causing the increase in void radii, thus; creating enough space for branched ganglia formations. Furthermore, the three-dimensional scans of silica sand samples do confirm the outcomes of two-dimensional scans, where ganglia formations (doublets and branches) are dominant along column samples S1 and S6. While smaller cluster formations are dominant in column samples S2, S3, S4, and S5 (See Figure 29. and Figure 30.).

Unlike silica sand samples, the quartz sand two-dimensional cross-sections do indicate that NAPL residuals take the shape of long branched ganglia (see Figure 27.). That can be evidently observed in sample Q2, where the two-dimensional cross-section image has the largest residual NAPL branch. Moreover, the result is confirmed when observing the three-dimensional scans (see Figure 31.) of quartz sand sample Q2. Other quartz sand samples (shown in Figure 31. and Figure 32.) show the same behavior of having long branched ganglia of residual NAPL as the dominant shape over smaller clusters. Long branched ganglia can occur both in sand and rock samples (Al-Raoush, 2009; Arns et al., 2005; Coles et al., 1998; Prodanović et al., 2006; Schnaar & Brusseau, 2005).

In a similar behavior, the three mixed samples (M1, M2, and M3) two-dimensional cross-section images also show that the dominant shape of residual blobs in the columns is the branched shape. However, the two-dimensional scans also suggest

that some individual cluster formations were produced (see Figure 28.). The three-dimensional scans (seen in Figure 33.) give a better understanding/visualization of ganglia formations in mixed samples. As mentioned above, blob clusters are better visualized in the three-dimensional scans despite the domination of the branched ganglia. The formation of cluster blobs might have resulted from the silica sand contribution in the mixed samples. Mixed sample M3 shows an interesting behavior, where branched ganglia are stacked on the left side of the sample and individual cluster blobs are concentrated on the right side of the sample. That indicates the left side of mixed sample M3 had better pore connectivity (leading to branched ganglia formations) in comparison with the right side of the sample.

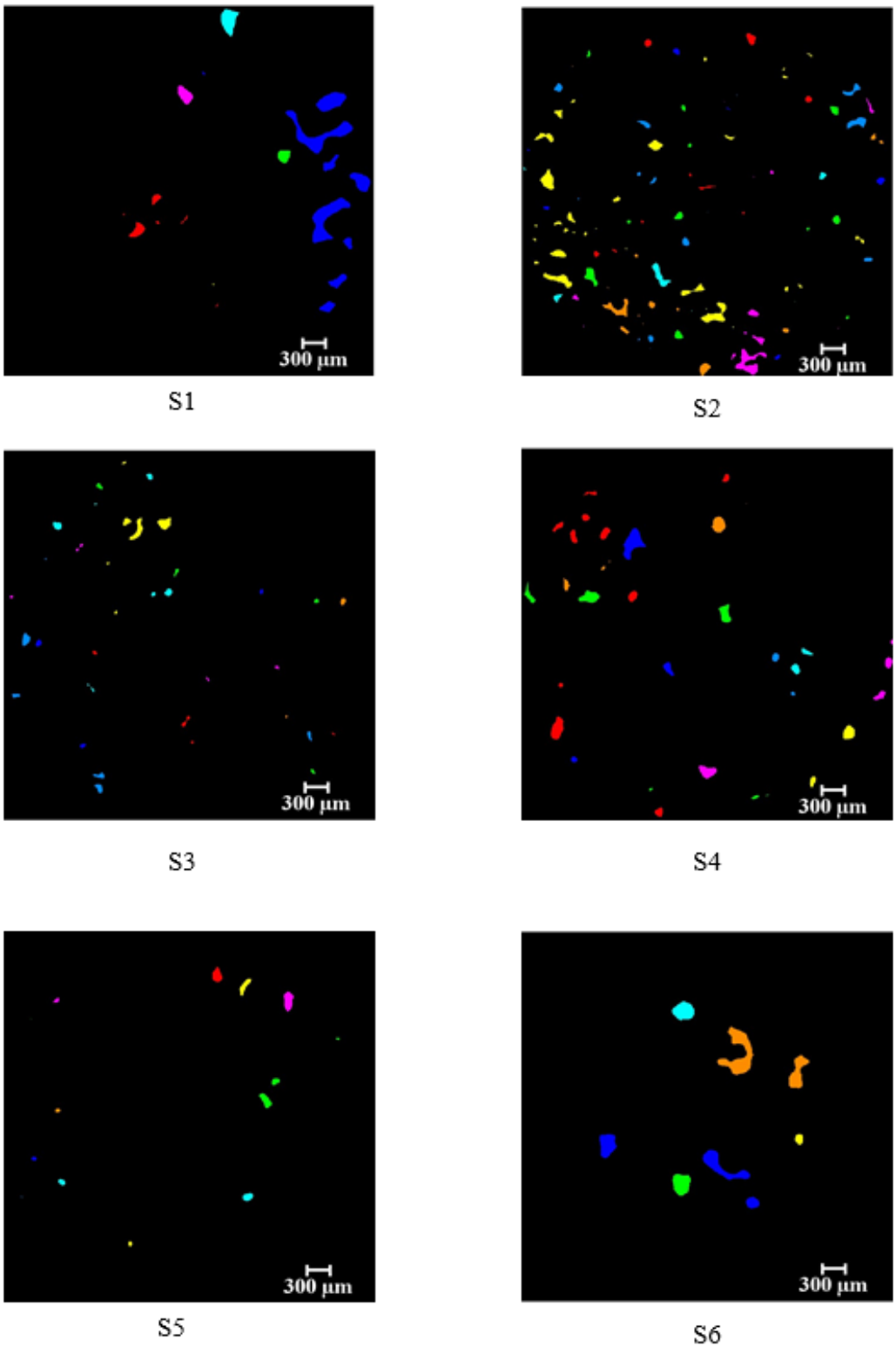

Figure 26. 2D Residual Oil Ganglia Labeling in Silica Sand.

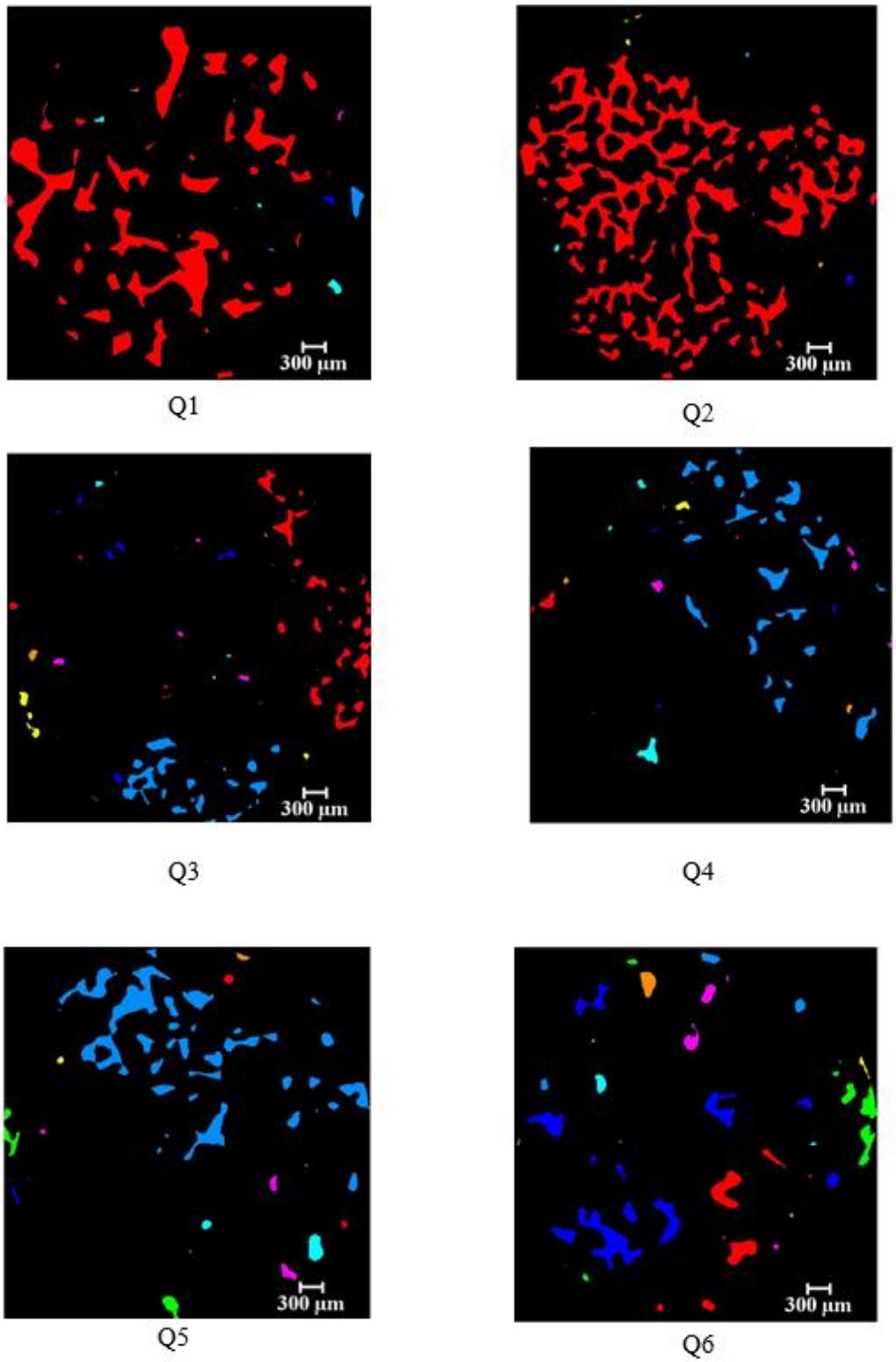

Figure 27. 2D Residual Oil Ganglia Labeling in Quartz Sand.

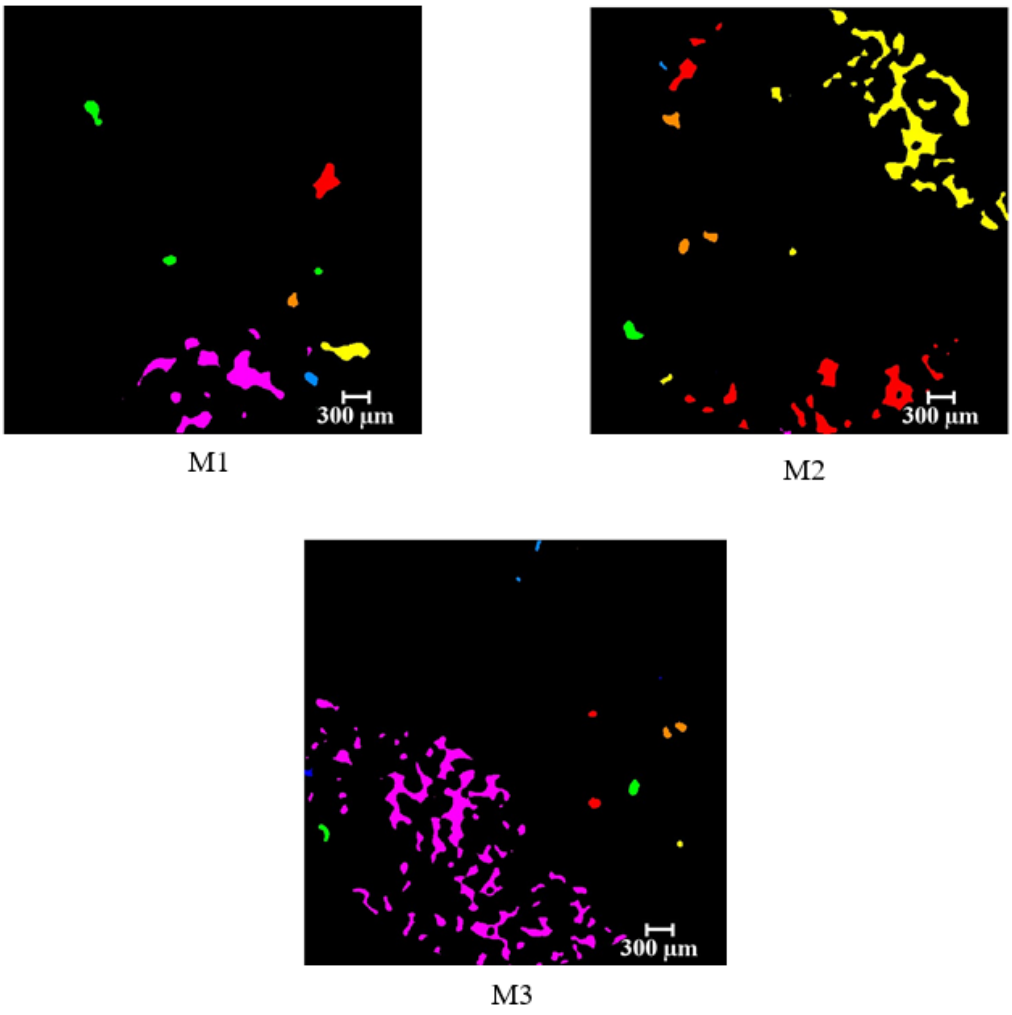

Figure 28. 2D Residual Oil Ganglia Labeling in Mixed Sand.

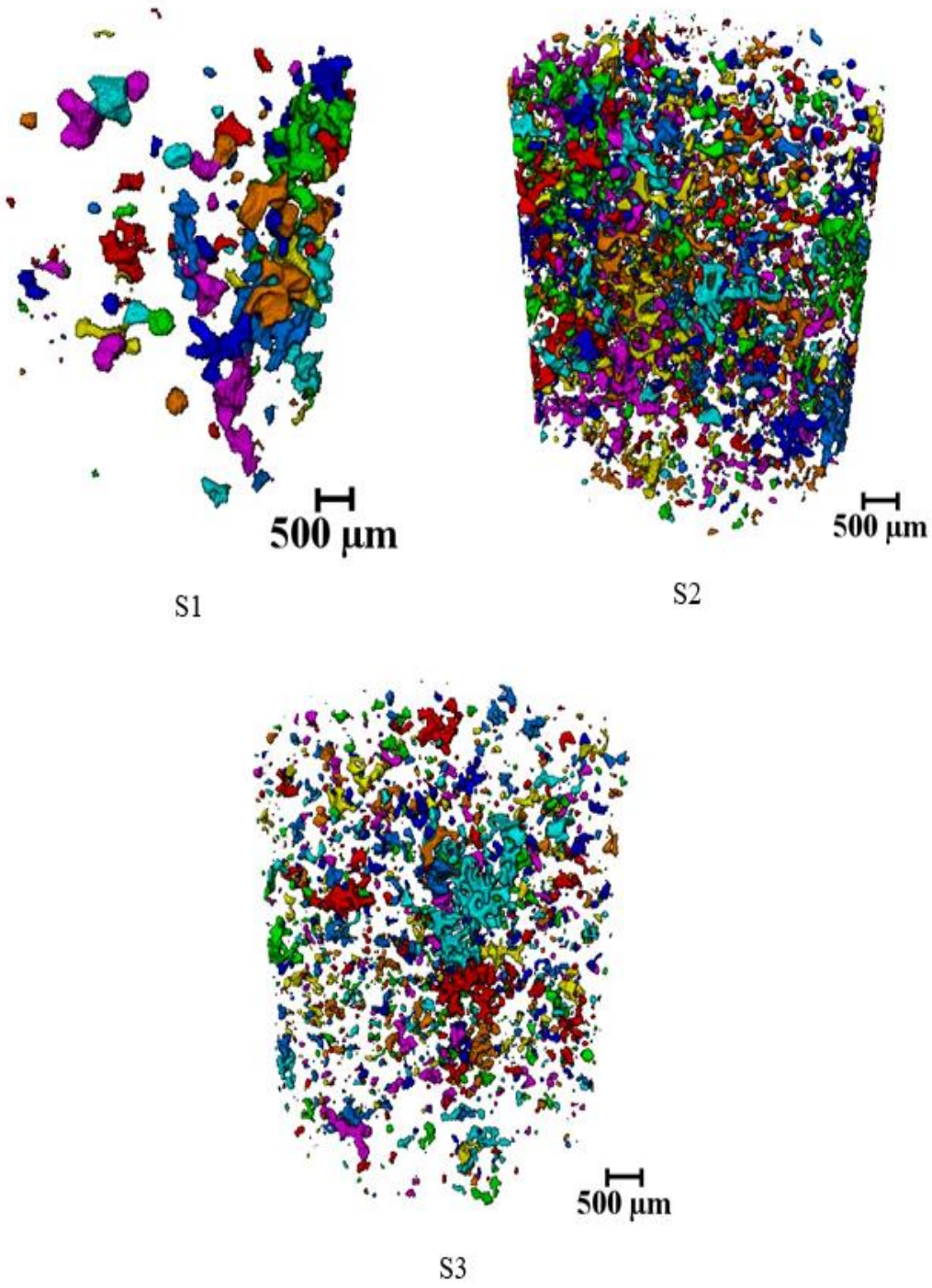

Figure 29. 3D Residual Oil Ganglia Labeling in Silica Sand S1-S3.

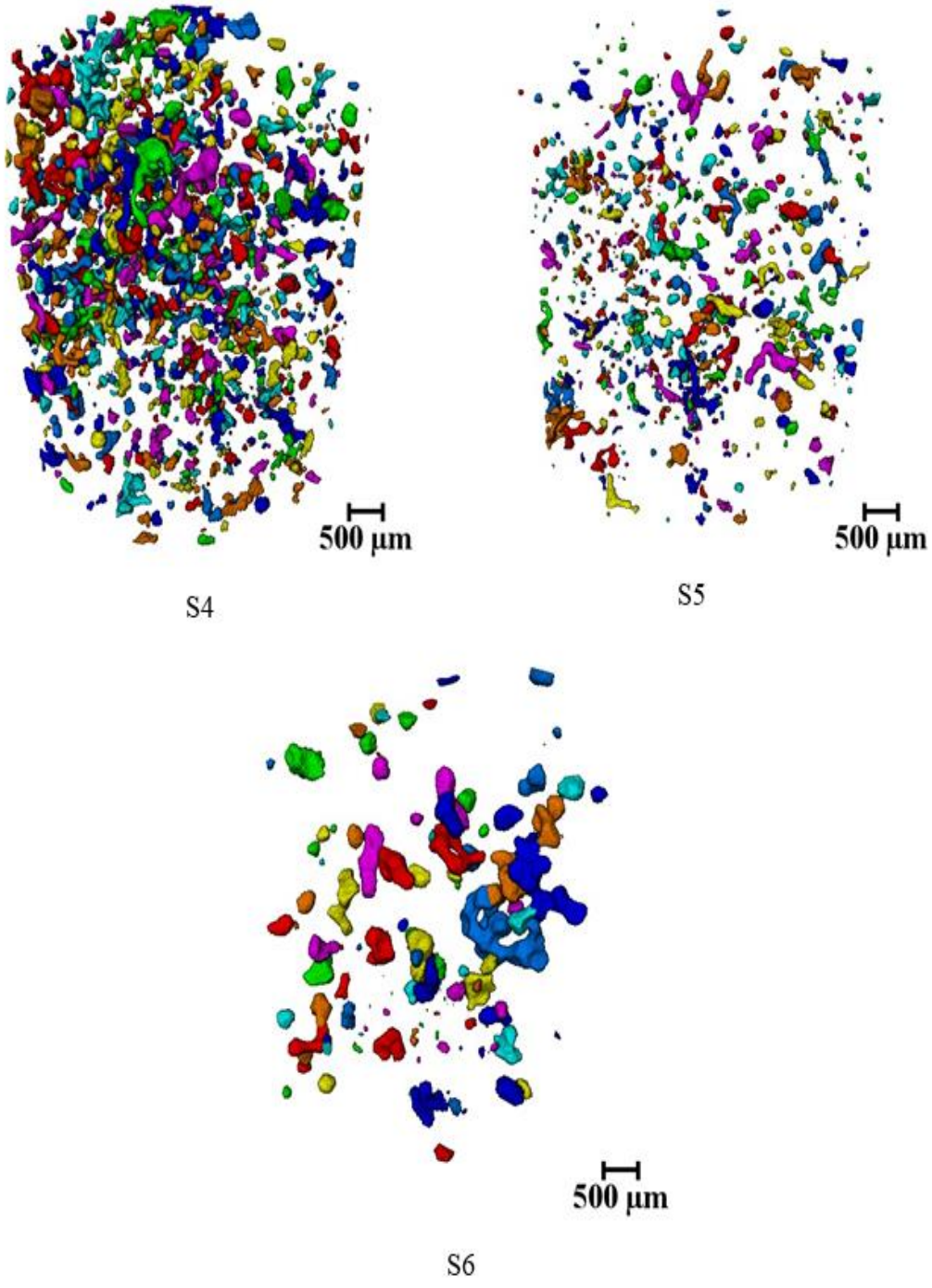

Figure 30. 3D Residual Oil Ganglia Labeling in Silica Sand S4-S6.

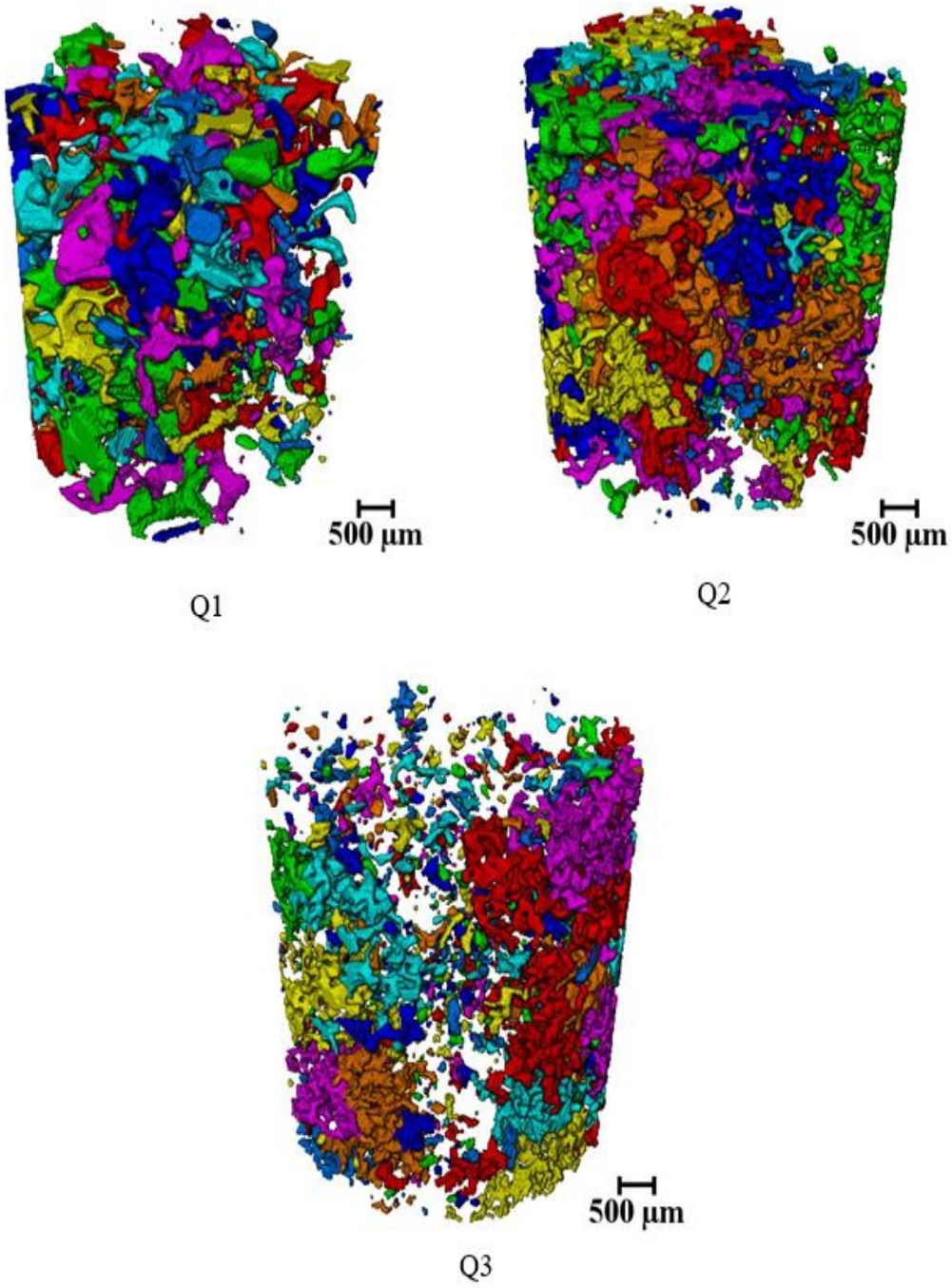

Figure 31. 3D Residual Oil Ganglia Labeling in Quartz Sand Q1-Q3.

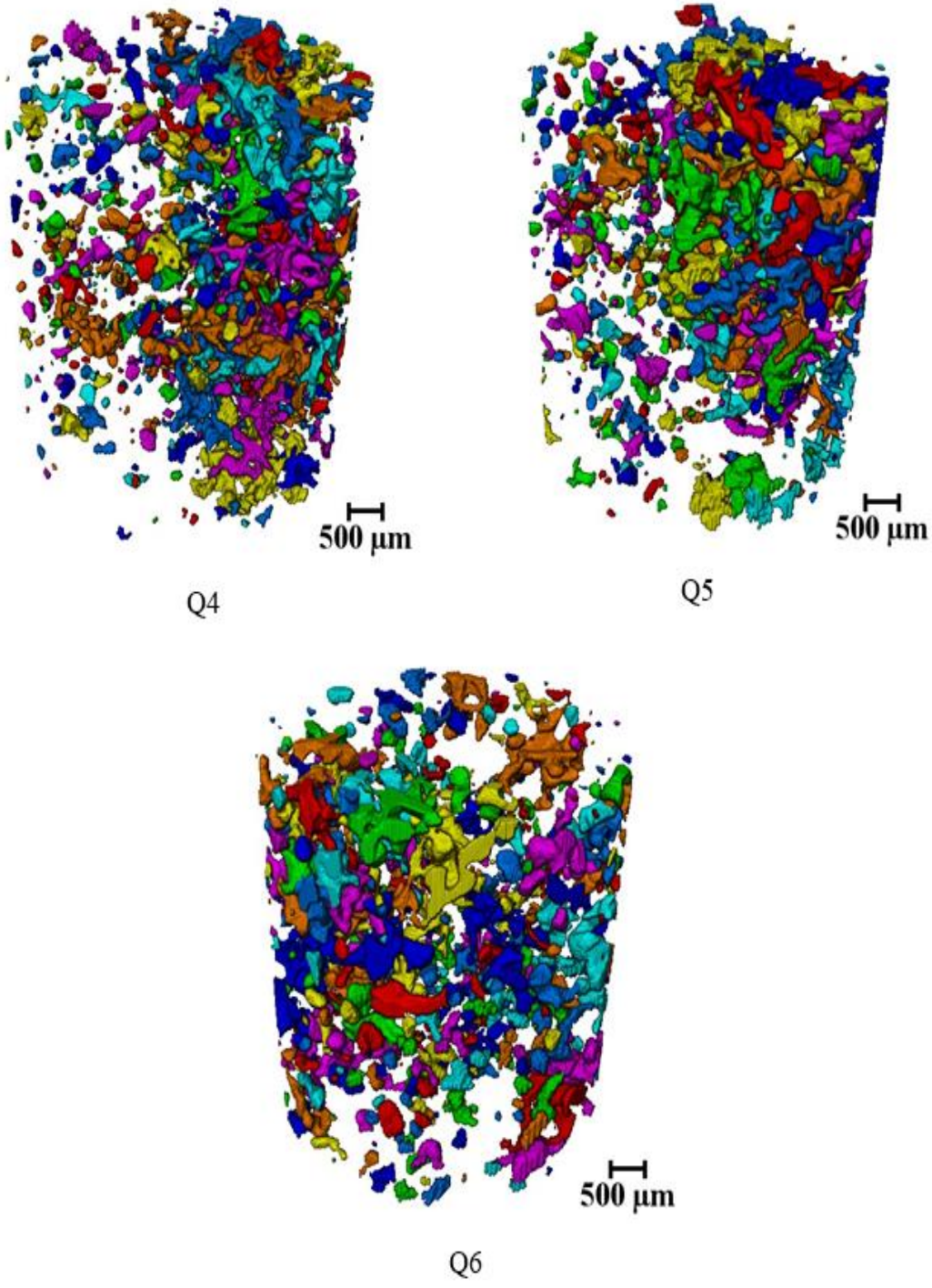

Figure 32. 3D Residual Oil Ganglia Labeling in Quartz Sand Q4-Q6.

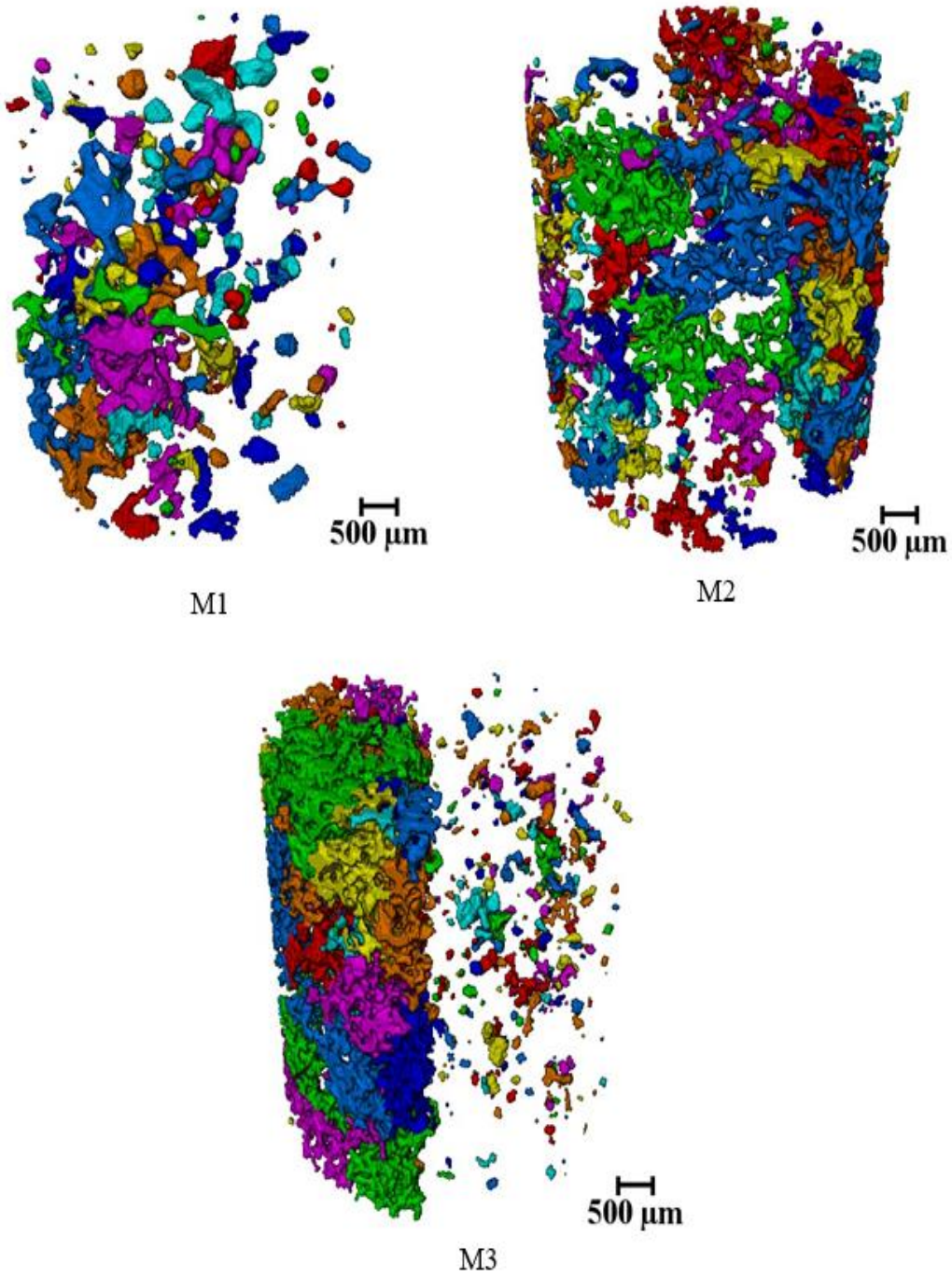

Figure 33. 3D Residual Oil Ganglia Labeling in Mixed Sand M1-M3.

5.4 System Characterization

Several physical properties of the fifteen sand samples were determined using the constructed three-dimensional pore network models. The oil saturation and water saturation relations with the sand samples' porosity were determined in (Figure.). It was observed that there is an increase in oil saturation values with the increase of sand porosity for all fifteen samples, while it was observed that water saturation decreases with the increase of sand porosity values also for all fifteen samples. The increase in oil saturation is due to the larger pores that allow preferential flow paths through the porous media leaving a higher portion of pores with lower fluid percolation. This leads to larger pores being occupied with NAPL residuals, which increases the irreducible oil saturation; hence resulting in lower water saturations at higher porosities for all sand samples.

The relationship between oil saturation and water saturation values was also plotted against pores and throats radiuses (see Figure 34.). There is a weak negative correlation between oil saturation and the increase of pore and throat radiuses for all fifteen samples. That is mainly due to the morphology and grain size distribution of the sand samples. On the other hand, it was observed that there is a positive correlation between water saturation and the increase of pore and throat radii for all fifteen samples. That effect was significant in silica sand samples compared to quartz sand samples. The increase of pore and throat radii allowed more residual blobs to be flushed out after the second water imbibition, especially for silica sand. The general trend of Figure and Figure 34 agrees with results reported in the literature on characterized residual NAPLs in the sand (Blunt et al., 2013; Doan et al., 2012; Iglauer et al., 2011; Lebedeva & Fogden, 2011; Princ et al., 2020).

The relationship between oil saturation and water saturation was plotted against the pore coordination number (see Figure 36.). The plot shows no clear correlation between oil and water saturations with the pore coordination number, due to the fact that the pore and throat sizes are widely distributed over each coordination number. In other words, oil and water saturation against the coordination number correlation is significantly affected by other pore network features such as pore and throat sizes and pore-throat aspect ratio. The latter shows an increase in oil saturation with the increase of the average pore-throat aspect ratio, while water saturation decreases with the increase of the average pore-throat aspect ratio. The data points are strongly correlated, which agrees with previous studies of (Andersson et al., 2018) that established a linear fit between residual oil saturation and pore-throat aspect ratio (called morphological aspect ratio) by dividing the pore radius of a given void by the average radiuses of all throats connected to the same pore body.

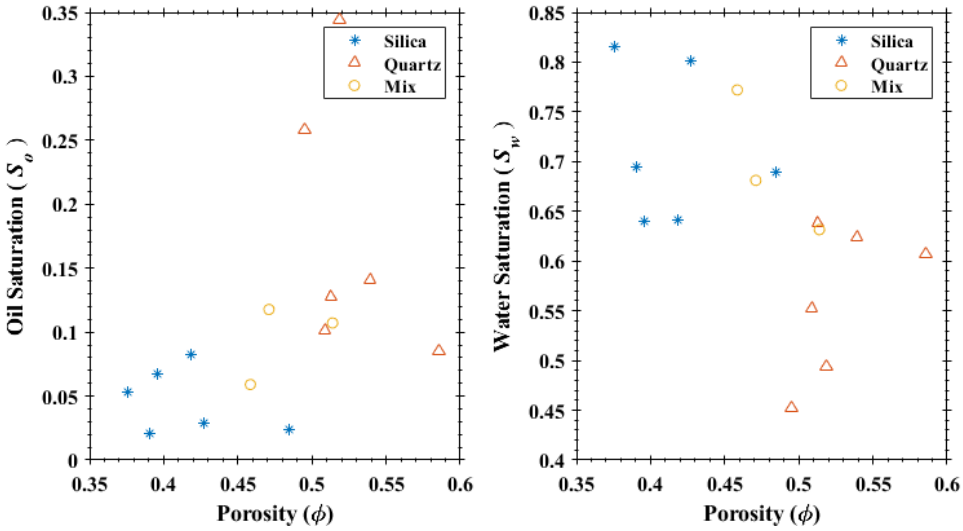

Figure 35. Oil and Water Saturations Relation With Sand Porosity for All Samples

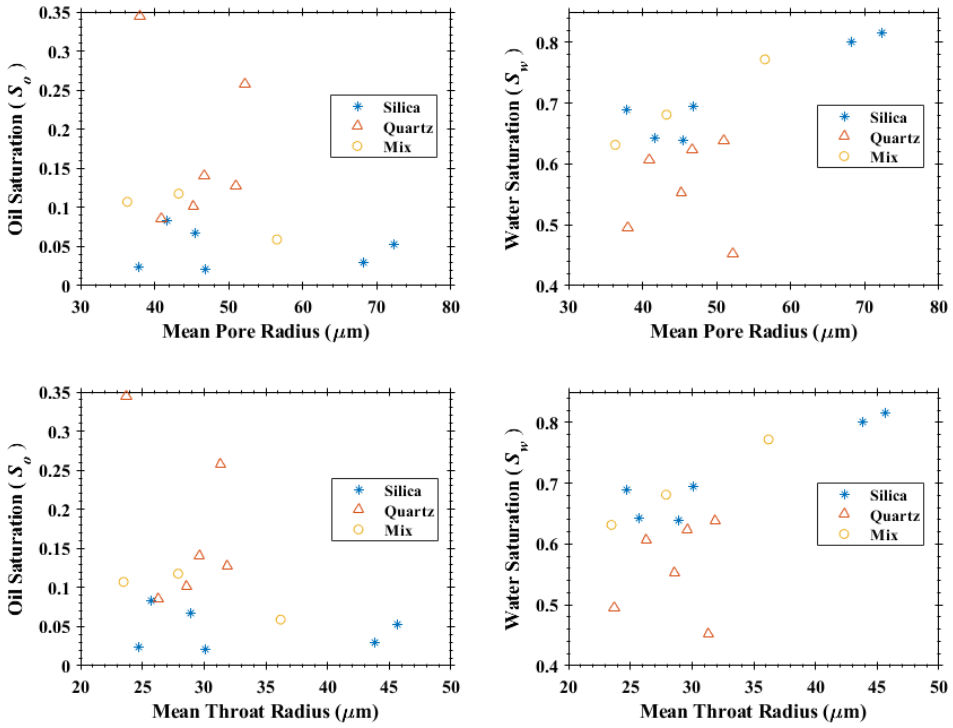

Figure. 34 Oil and Water Saturations Relation With Sand Average Pores and Throats Radiuses for All Samples.

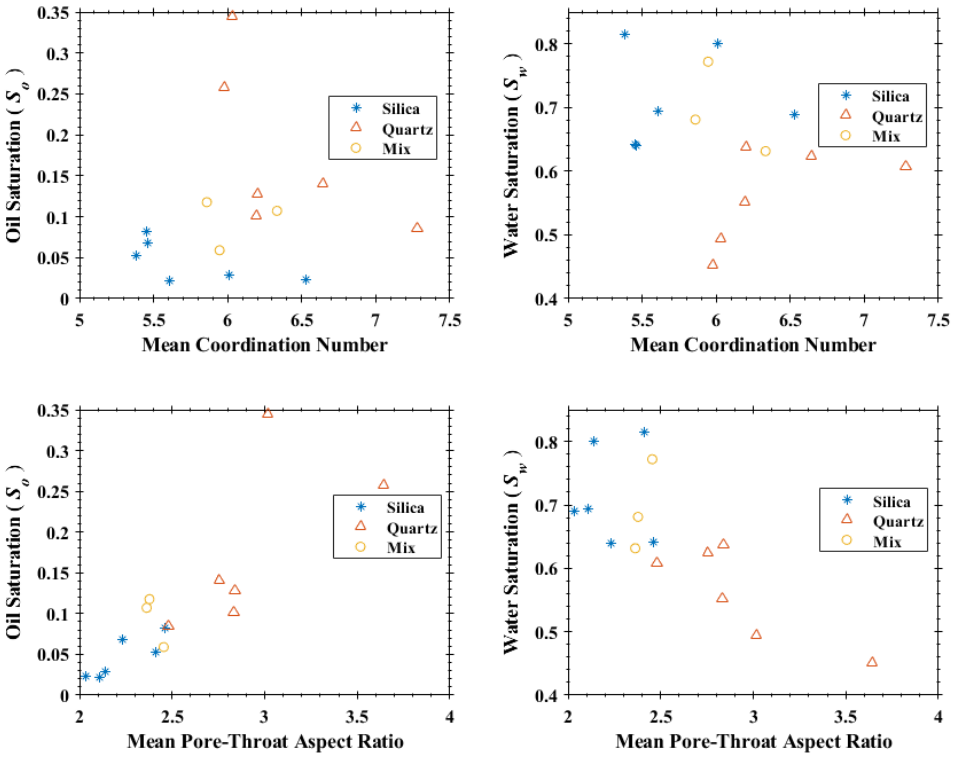

Figure 36. Oil and Water Saturations Relation With Sand Average Coordination Number and Averarge Pore-Throat Aspect Ratio.

5.4.1 Trapped NAPL Blobs Characterization

The characteristics of trapped NAPL blobs were calculated after segmenting and labeling individual oil blobs in each system. Blob's area over volume (surface area of blob divided by its volume), Blob's aspect ratio (blob's maximal axis divided by its minimal axis), blobs' equivalent diameter, and blobs' volumes were plotted against the probability in the system for all individual labeled blobs. For the Blob area over volume plots, the area was calculated using the marching cubes algorithm to eliminate the effect of cubic voxel shape, which results in an over-estimated area. Thus, the marching cub algorithm results in an accurate surface area estimation for irregularly shaped blobs. However, the volume is calculated from the total number of voxels inside the labeled blob. Figure 37. shows the silica sand distribution (probability against areas over volume). Generally, the plot indicates a descending order with the increases of areas over volume value. However, quartz sand shows a more extreme descending order in comparison with silica sand (see Figure 38.). Likewise, Figure 39. shows a descending order with the increases of areas over volume value, except for sample M3 that shows a relatively even distribution. The aspect ratio describes the proportion of blobs' shapes from $Aspect\ Ratio = \frac{Largest\ 3D\ Length}{Shotest\ 3D\ Width}$ Equation 2. All fifteen samples (silica, quartz, and mixed samples) initially show an ascending relationship of probability with the increase of aspect ratio values, followed by a decline in probability values with the increase of aspect ratio forming a peak (located between aspect ratio value 1 and 2) (see Figure 40., Figure 41., and Figure 42.).

$$Aspect\ Ratio = \frac{Largest\ 3D\ Length}{Shotest\ 3D\ Width}$$ Equation 2. Aspect Ratio Equation.

Figure 43., Figure 44., and Figure 45. Represent the correlation between the blob's abundance against their equivalent diameter. It was observed that the fifteen sample blobs' probability values decline with the increase of the value of their equivalent diameter. In other words, the vast majority of blobs that exist in the system do have smaller diameters. Thus, it is less probable to detect a blob with a diameter larger than 800 micrometers. Similarly, a general decrease in blob's probability values was observed with the increase in blobs' volume values, except for mixed sample M3 that showed a fluctuant distribution along the x-axis (see Figure 46., Figure 47., and Figure 48.). The trapped NAPL characterization results of the saturated samples have a similar trend to samples reported in the literature that belong to unsaturated packing (Hu et al., 2020; Kazemi et al., 2020; Scanziani et al., 2020; Song et al., 2020; Yang et al., 2020).

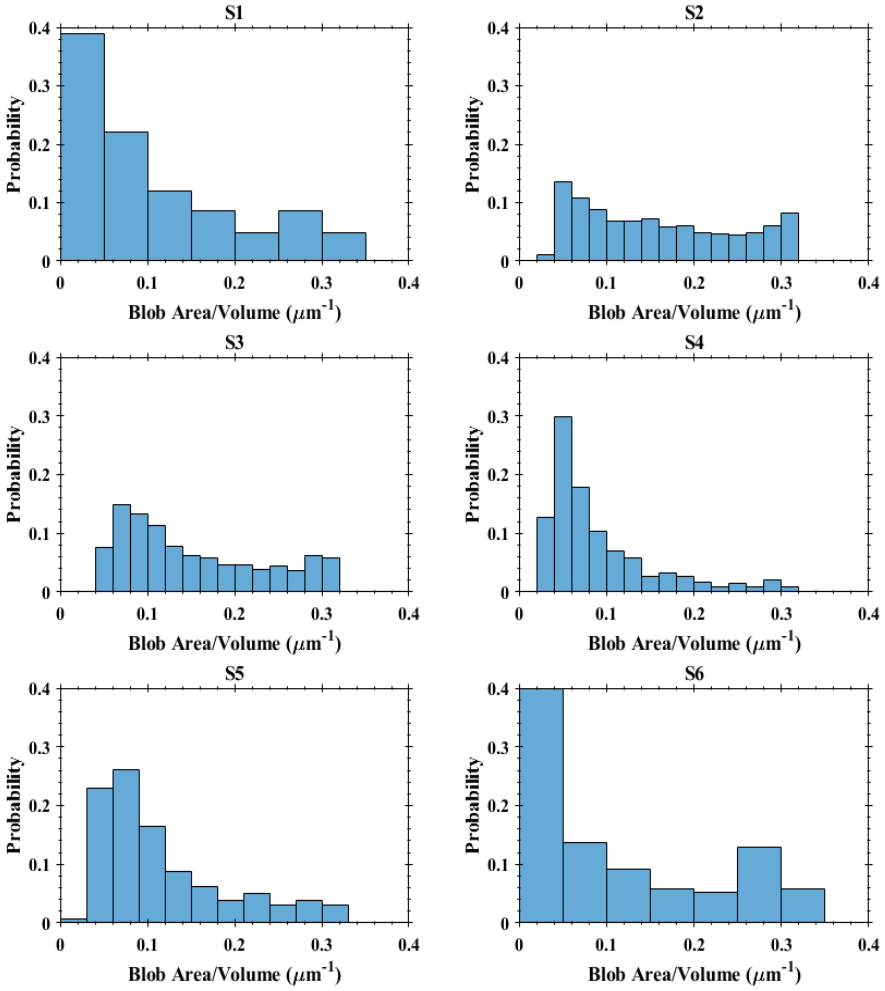

Figure 37. Probability Against Blob's Surface Area Over Blob's Volume for All Silica Sand Samples S1-S6.

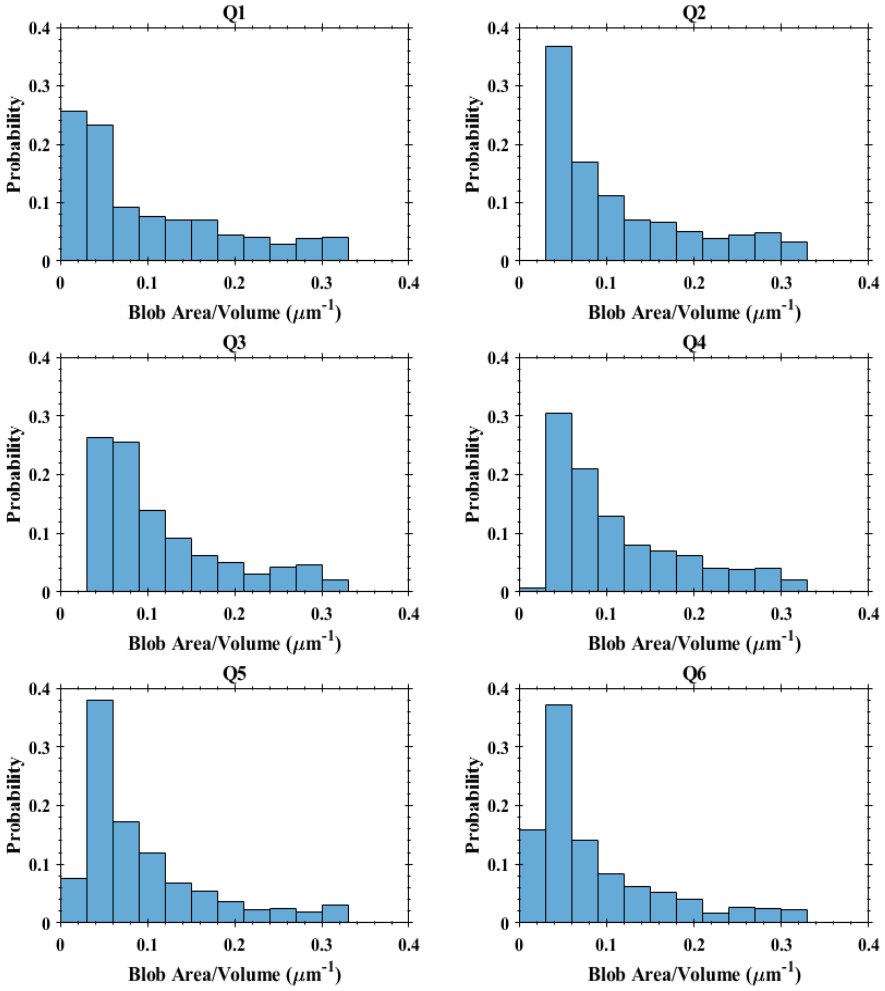

Figure 38. Probability Against Blob's Surface Area Over Blob's Volume for All Quartz Sand Samples Q1-Q6.

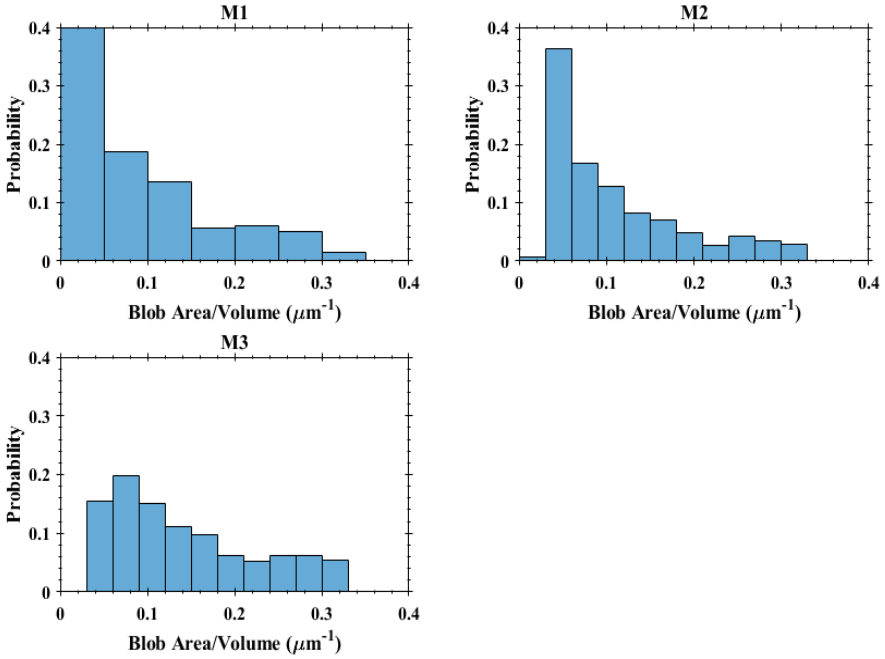

Figure 39. Probability Against Blob's Surface Area Over Blob's Volume for All Mixed Sand Samples M1-M3.

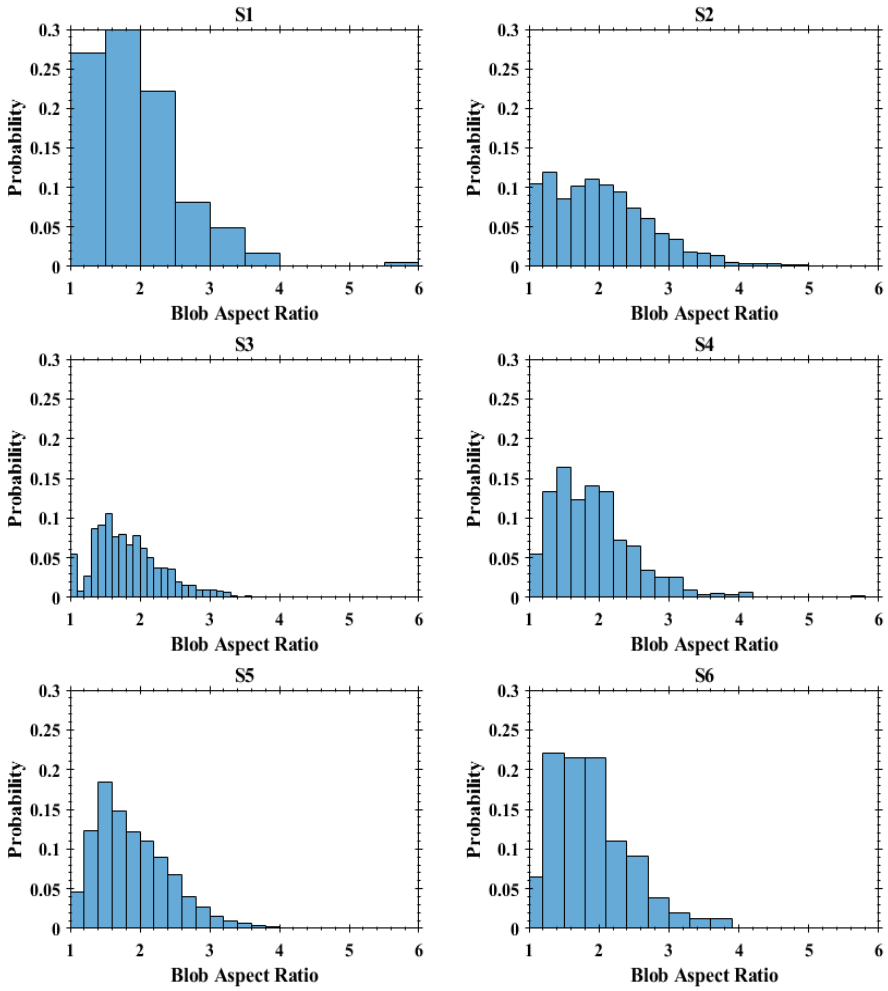

Figure 40. Probability Against Blob's Aspect Ratio for All Silica Sand Samples S1-S6.

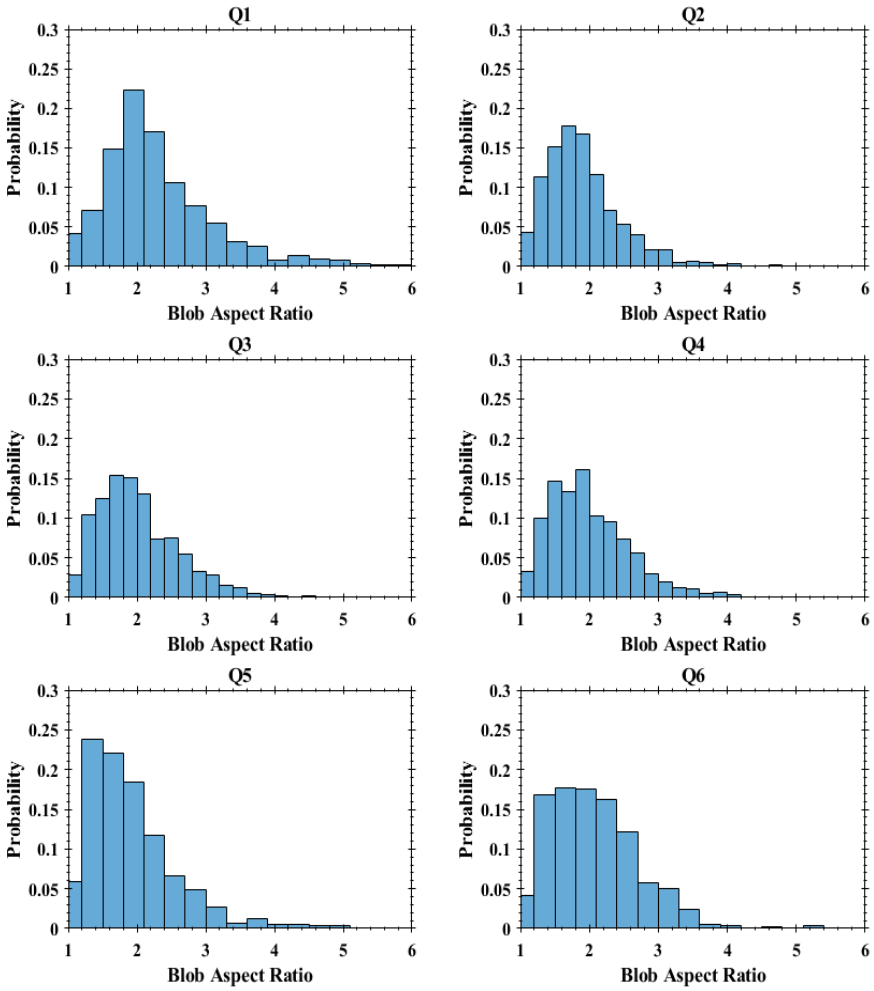

Figure 41. Probability Against Blob's Aspect Ratio for All Quartz Sand Samples Q1-Q6.

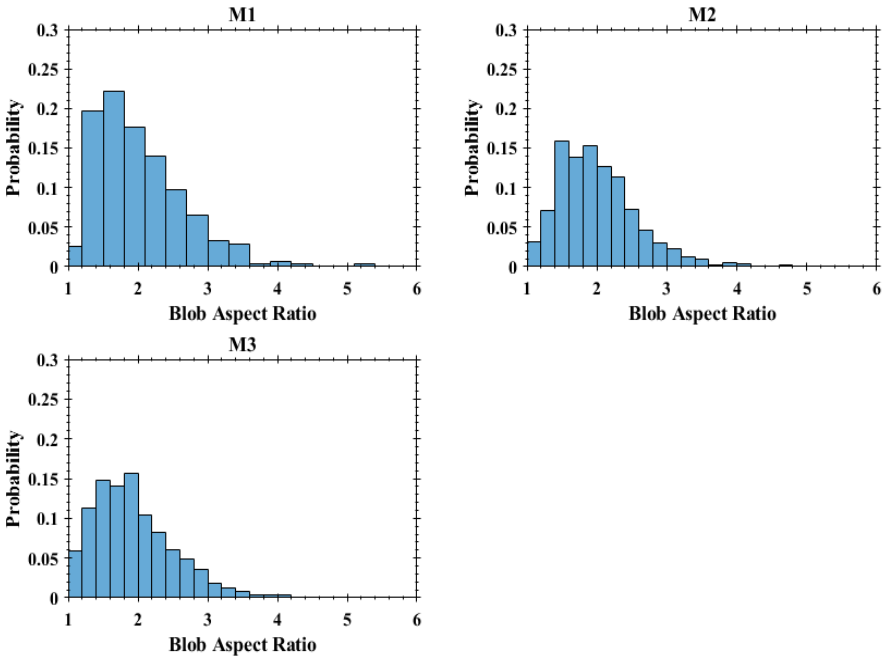

Figure 42. Probability Against Blob's Aspect Ratio for All Mixed Sand Samples M1-M3.

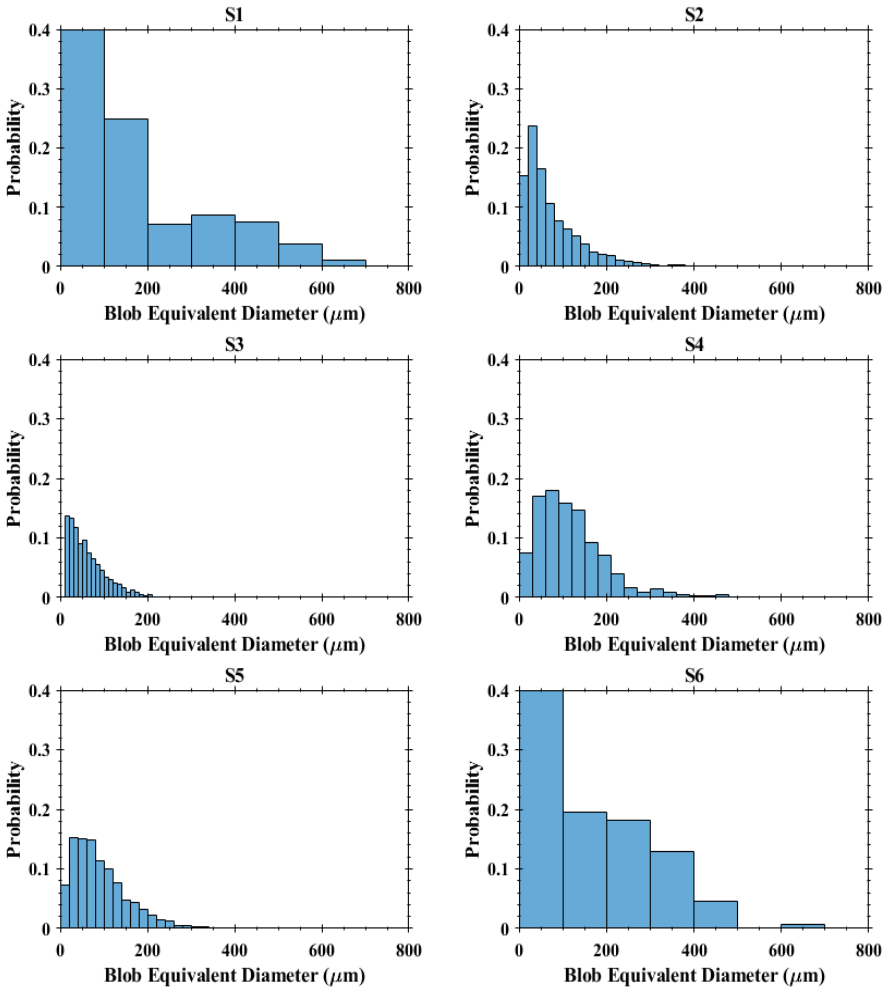

Figure 43. Probability Against Blob's Equivalent Diameter for All Silica Sand Samples S1-S6.

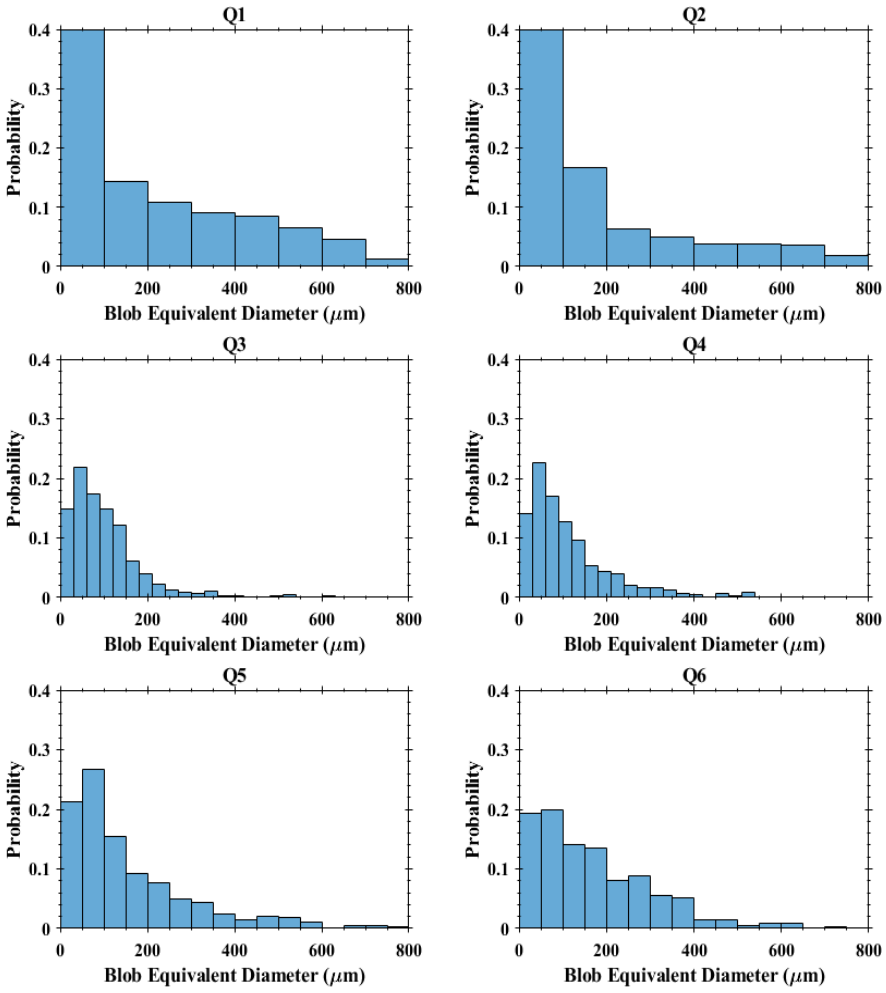

Figure 44. Probability Against Blob's Equivalent Diameter for All Quartz Sand Samples Q1-Q6.

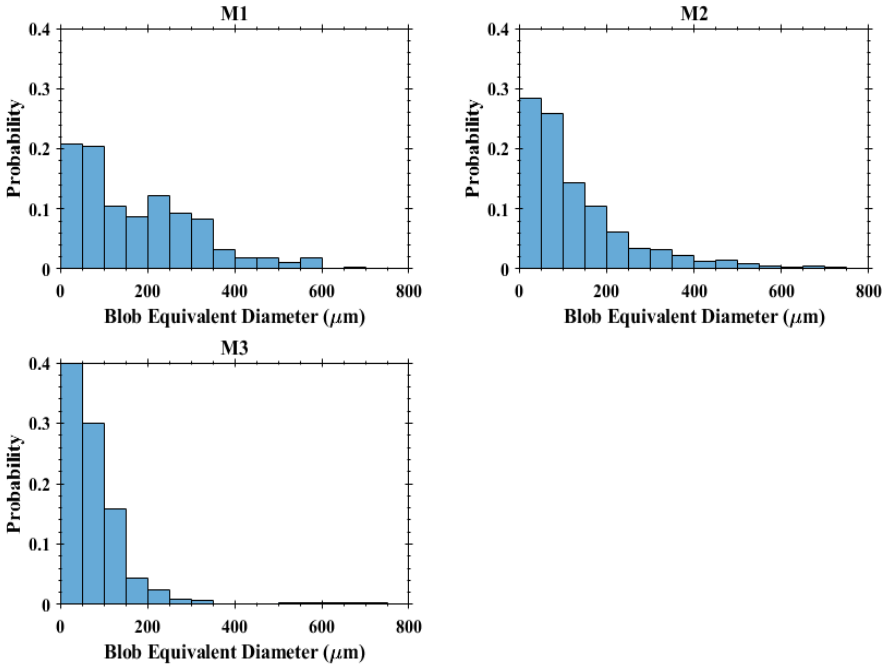

Figure 45. Probability Against Blob's Equivalent Diameter for All Mixed Sand Samples M1-M3.

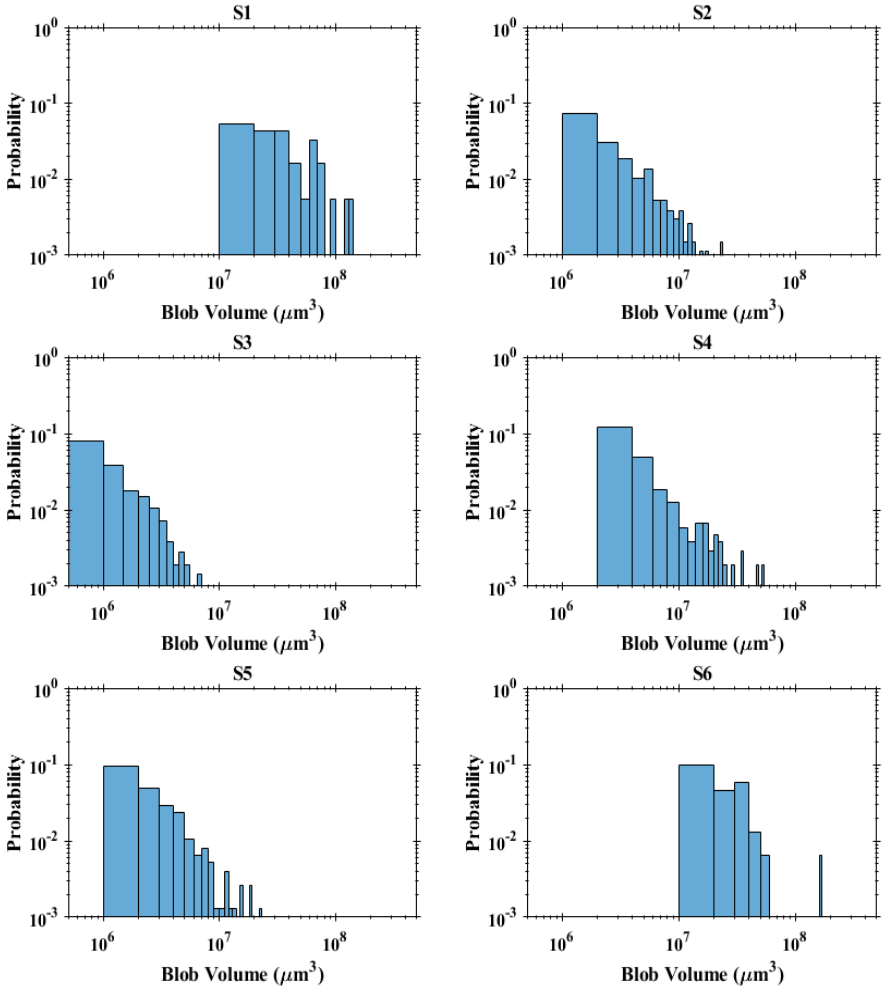

Figure 46. Probability Against Blob's Volume for All Silica Sand Samples S1-S6.

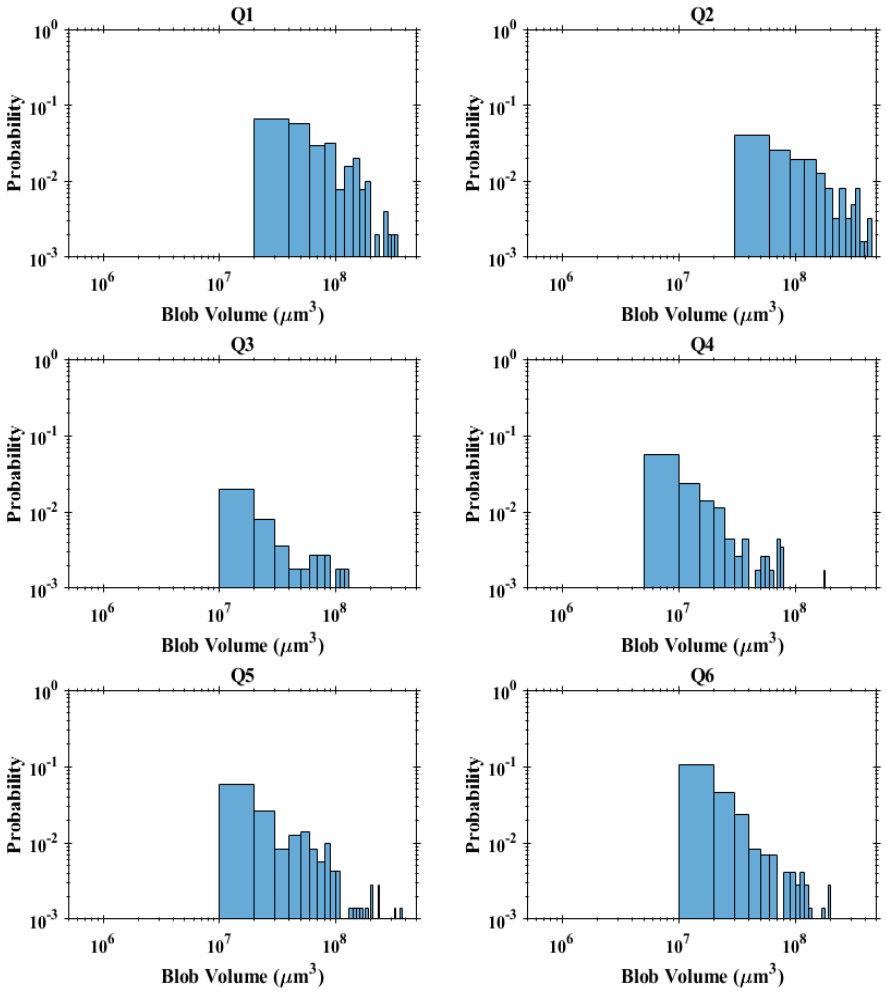

Figure 47. Probability Against Blob's Volume for All Quartz Sand Samples Q1-Q6.

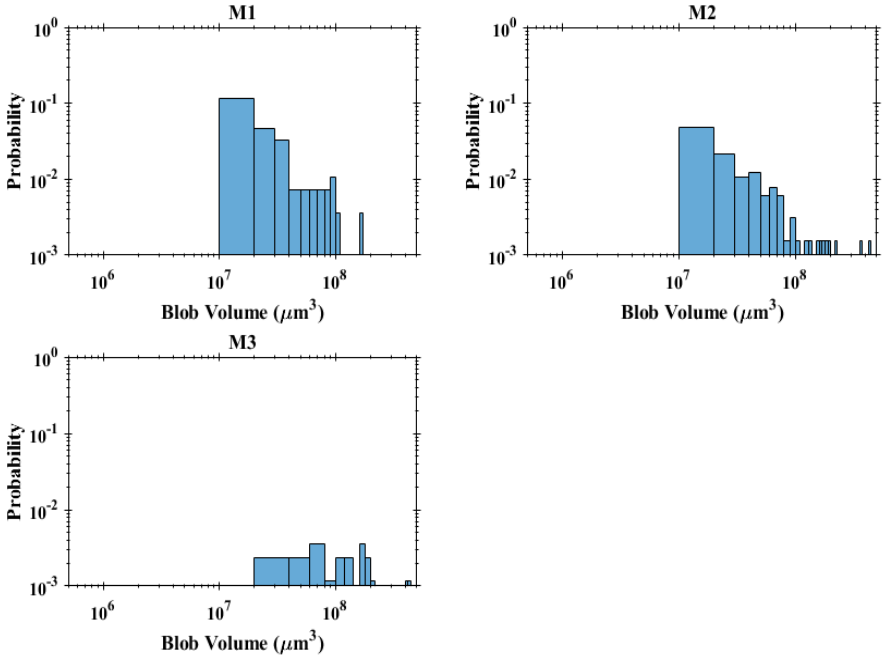

Figure 48. Probability Against Blob's Volume for All Mixed Sand Samples M1-M3.

5.4.2 Grain Characterization

The characteristics of grains were acquired after segmenting and labeling each particle. Aspect ratio (grains' maximal vs minimal axis), grain diameter, and grain volumes were plotted against the probability in the system for all individual labeled grains. Likewise, blob aspect ratio against its probability, the grains probability for all fifteen samples (seen in Figure 49., Figure 50., and Figure 51.) starts with a slight increase of probability values with the increase of aspect ratio values, followed by a decline in probability values with the increase of aspect ratio forming a peak that generally falls between aspect ratio values 1.5 and 2 (unlike blobs peak range of 1 to 2). The grain diameter is calculated based on the smallest 3D width of the grain label to replicate the sieve analysis done to obtain the size distribution of sand grains in the porous media. The grains' probability values against their diameters demonstrate a Poisson distribution shape for all fifteen samples, meaning that a peak (highest diameter probability) generally occurs between the range of 200 to 400 micrometer. However, it is less probable to observe grain diameter less than 200 micrometers in size and greater than 600 micro-meters (see Figure 52., Figure 53., and Figure 54.). No direct/general relationship pattern was observed between grains' probability values and grains' volumes. For instance, silica sand samples S1-S6 and quartz sand samples Q1-Q6 show a Poisson distribution pattern, while the other silica sand samples (S2, S3, S4, and S5) and quartz sand samples (Q2, Q3, Q4, and Q5) show an ascending relationship with the increase of volume (see Figure 55. and Figure 56.). Mixed samples M1 and M3 show a slight increase in grains' probability values followed by a decrease with the increase of volume, while sample M2 shows a direct decrease pattern with the increase of grains' volume values (see Figure 57.).

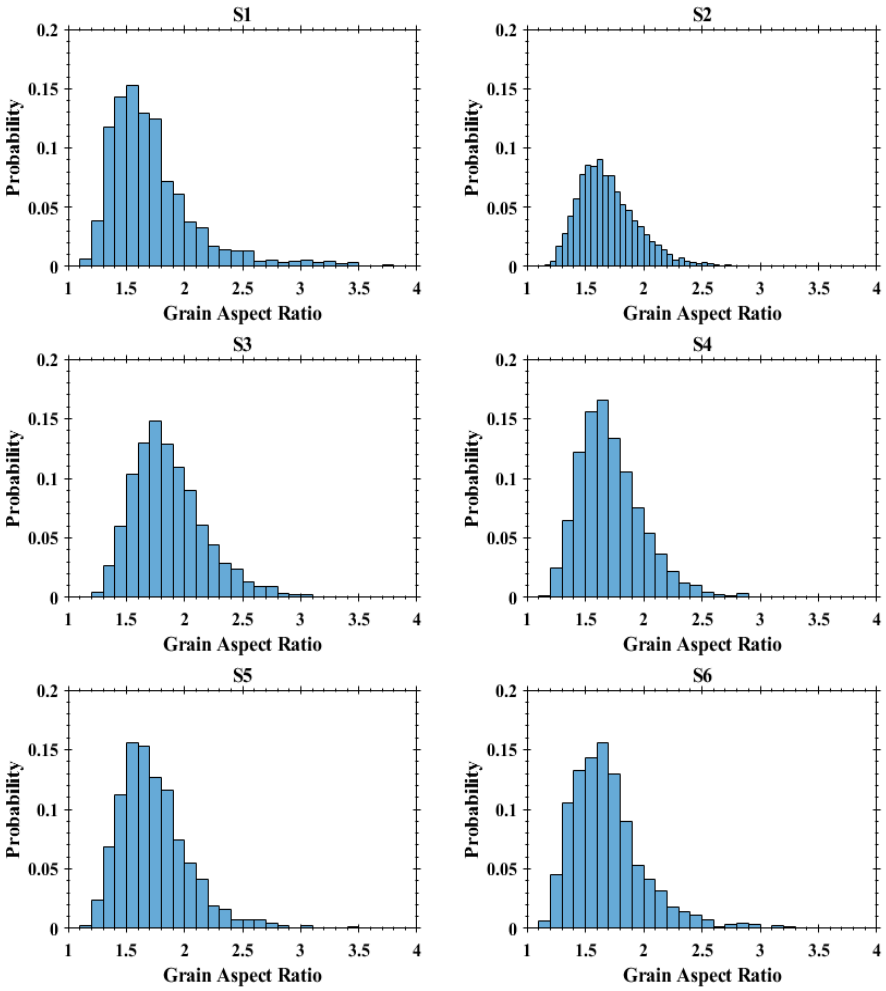

Figure 49. Probability Against Grain's Aspect Ratio for All Silica Sand Samples S1-S6.

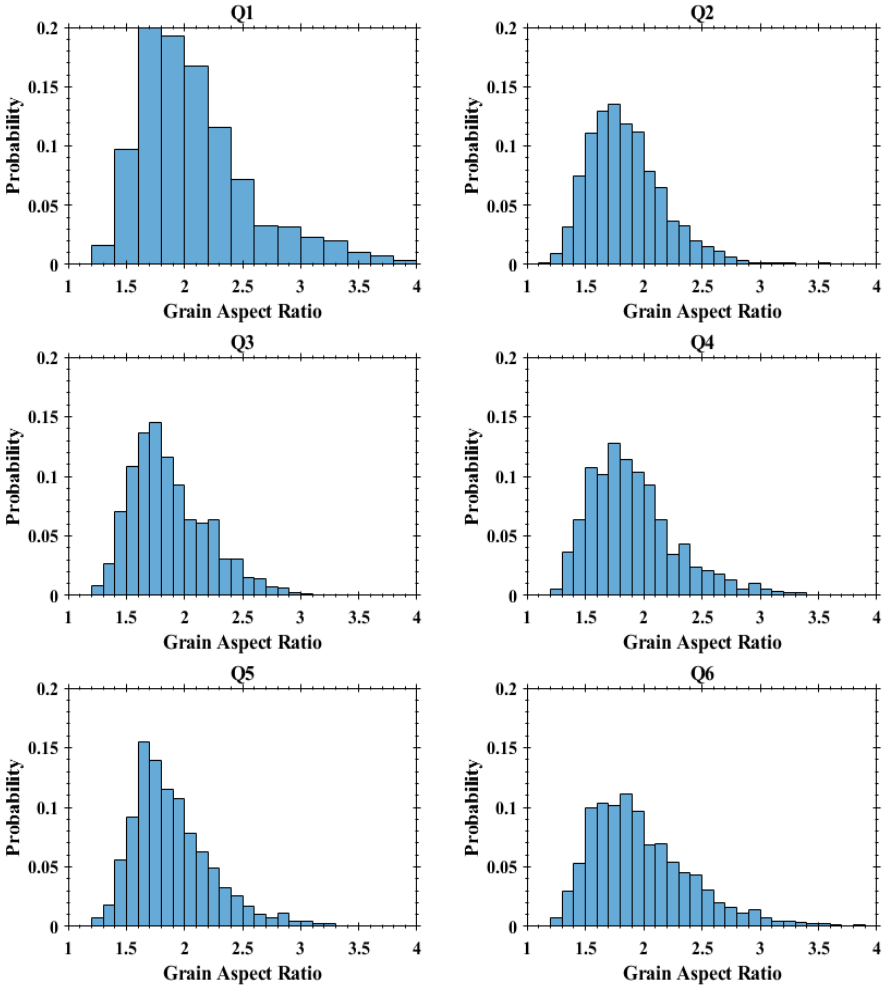

Figure 50. Probability Against Grain's Aspect Ratio for All Quartz Sand Samples Q1-Q6.

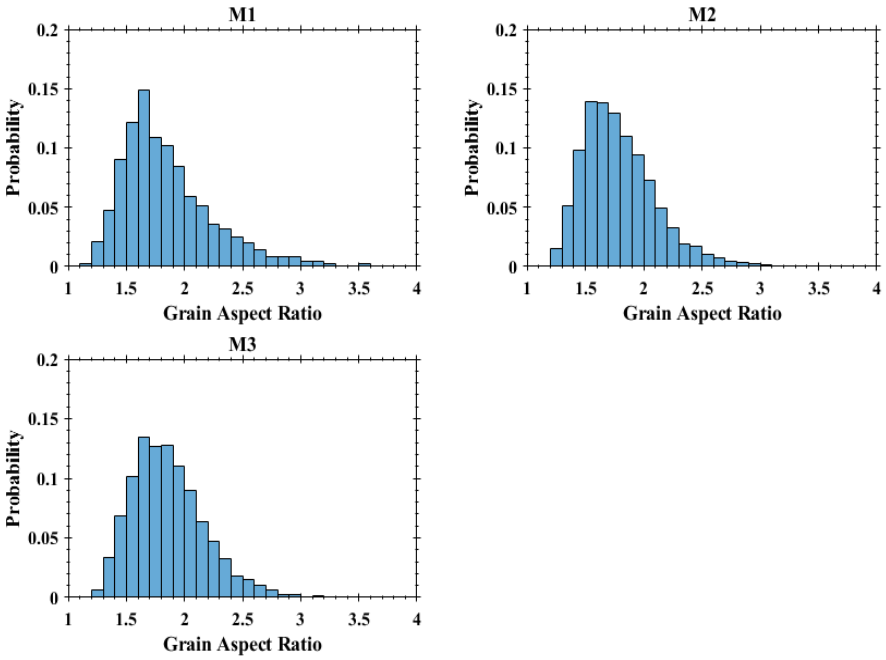

Figure 51. Probability Against Grain's Aspect Ratio for All Mixed Sand Samples M1-M3.

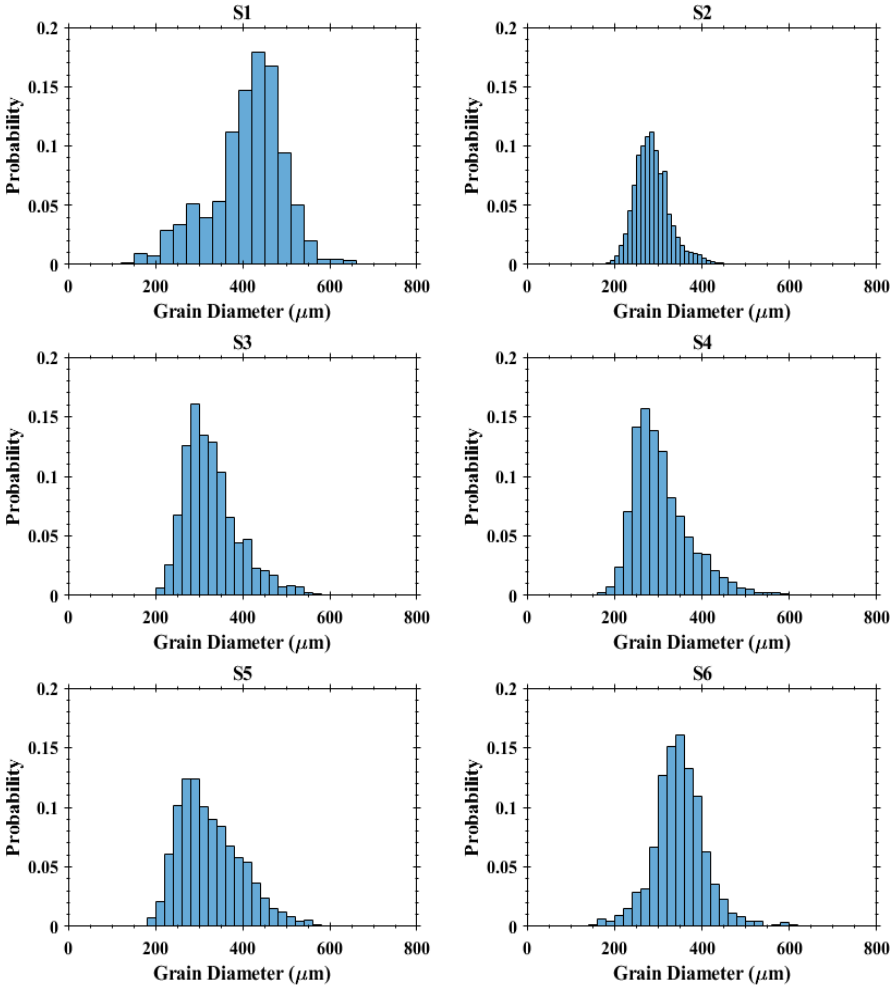

Figure 52. Probability Against Grains's Diameter for All Silica Sand Samples S1-S6.

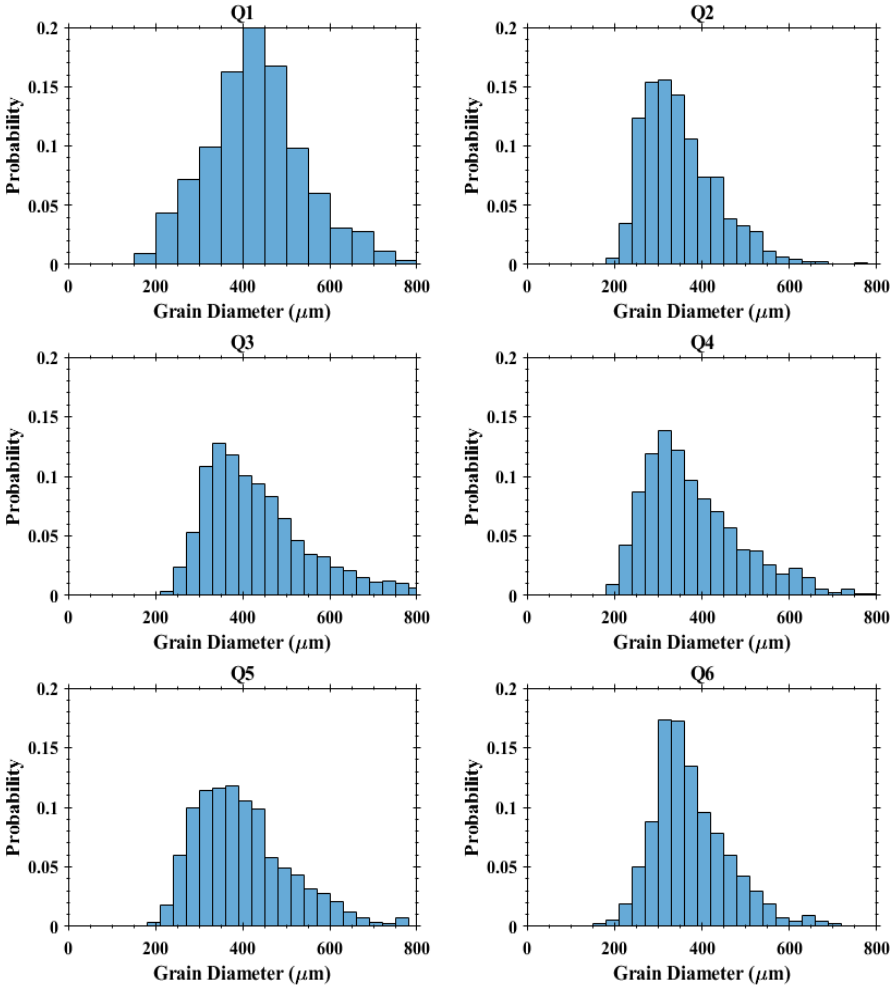

Figure 53. Probability Against Grains's Diameter for All Quartz Sand Samples Q1-Q6.

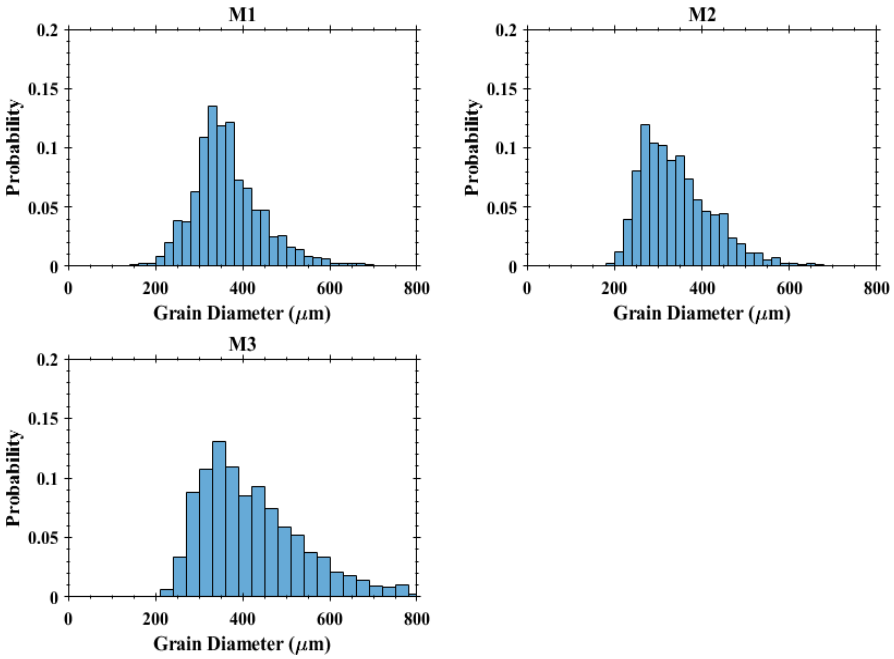

Figure 54. Probability Against Grains's Diameter for All Mixed Sand Samples M1-M3.

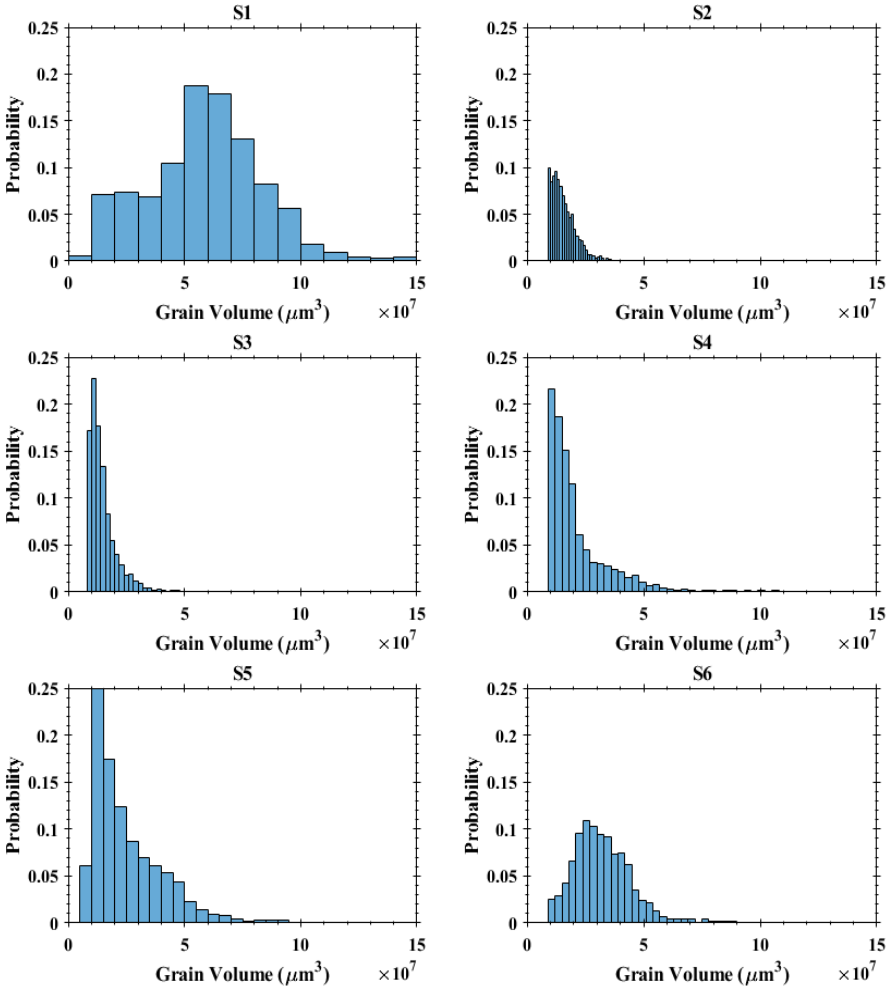

Figure 55. Probability Against Grains's Volume for All Silica Sand Samples S1-S6.

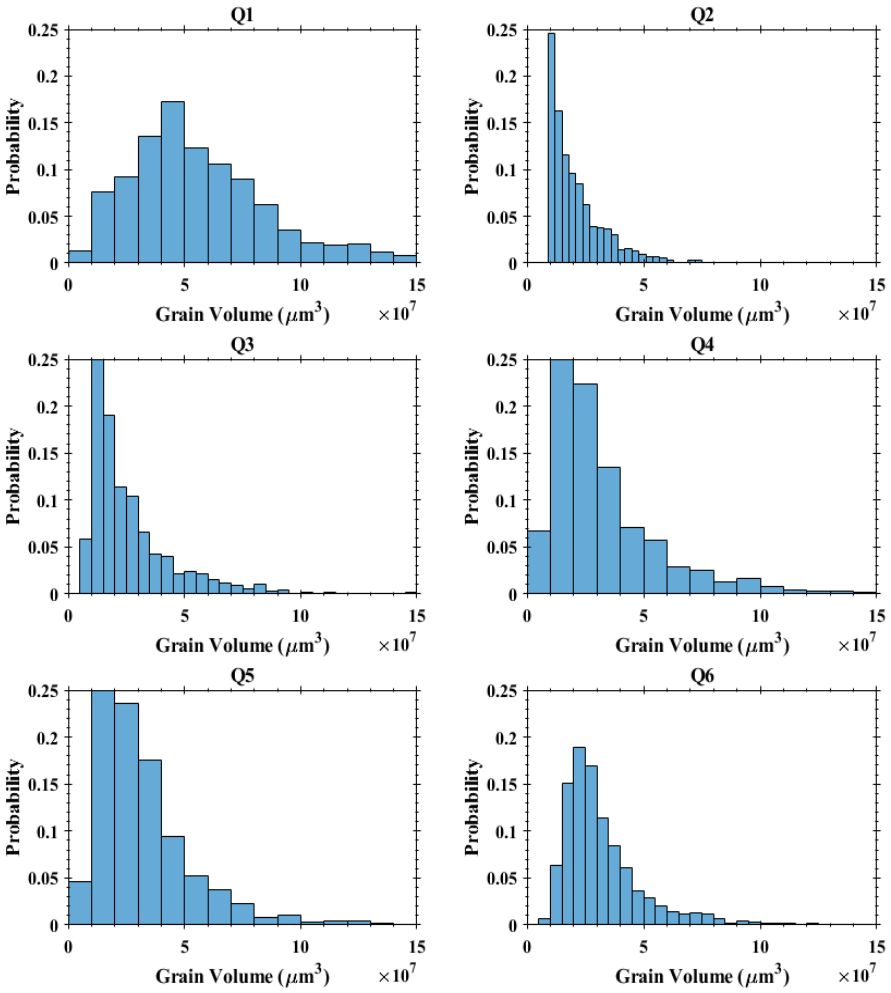

Figure 56. Probability Against Grains's Volume for All Quartz Sand Samples Q1-Q6.

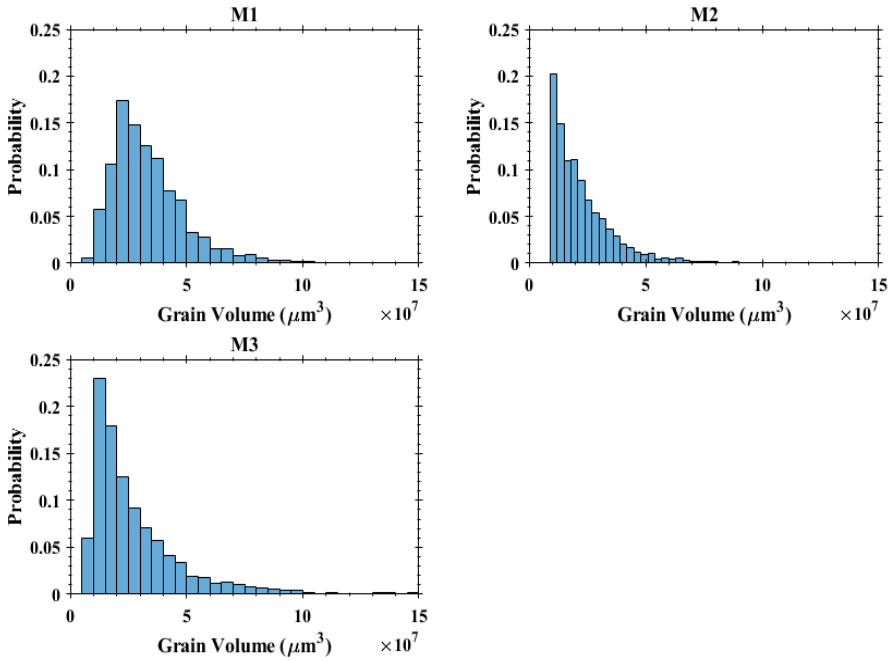

Figure 57. Probability Against Grains's Volume for All Mixed Sand Samples M1-M3.

5.5 NAPL Occupancy vs Pore Size and Pore Coordination Number

In order to fill the knowledge gap, the relationship between NAPL pore intersection percentage (NAPL occupancy) was correlated with the pore radius for each individual pore for all fifteen sand samples (see Figure 58., Figure 59., and Figure 60.). The graph describes the residual oil occupancy percentage of each pore in each column. At the first glance, all graphs show a c-shape diagram, that has an upper and a lower region with opposite intervals. The change in interval occurs around the 20% intersection, where the intersection increases for pores that were occupied by residual NAPL more than 20% as the pore radius increases. On the contrary, intersection decreases for pores that were occupied by residual NAPL less than 20% as the pore radius increases. Non-equal distribution was observed along with occupancy percentage ranges (20%-40%), indicating that the interface between water and residual NAPL was lower in the pores compared to throats. The previous observation agrees with pore-filling observations of the literature for NAPLs and can provide a pore network point of view explanation to such observations (Gao et al., 2019; Lin et al., 2021; Mohamed et al., 2020; Scanziani et al., 2018; Singh et al., 2017; Wang et al., 2019). It was also observed that within the fifteen sand samples, no pore intersection (NAPL occupancy) was greater than 80%.

Another gap in knowledge was the relation between pore intersection percentage and pore coordination number for each individual pore, the correlation was plotted for each pore based on each of the fifteen sand samples' (see Figure 61., Figure 62., and Figure 63.). It was observed that on average, the number of occupied pores decreases with the increase of pore coordination number especially after coordination numbers five and six. Since increased coordination number results in better access to the pores, enhancing flooding and the removal of trapped oil from the system (Akarri,

2019; Alhosani et al., 2020; Li et al., 2018; Liu et al., 2021; Liu et al., 2018; Shabaninejad, 2017). Mixed sand (M3) was an exception, where the decrease of occupied pores started to decrease after coordination number ten. Furthermore, it was noted that pores with coordination numbers between one and four are evenly distributed on average over the occupancy percentage range, compared to pores with a higher coordination number that were segregated either above 50% intersection or below 10% intersection. Once again, the separation observation was an exception in mixed sample M3, where the segregation started after coordination number eleven. That can be justified by the correlation of throats and pores. As the number of throats connected to a pore increase, the percentage of NAPL blobs declines in pores with high percolation. Thus, the pores with high occupancy percentages are unaffected due to low percolation in such pores.

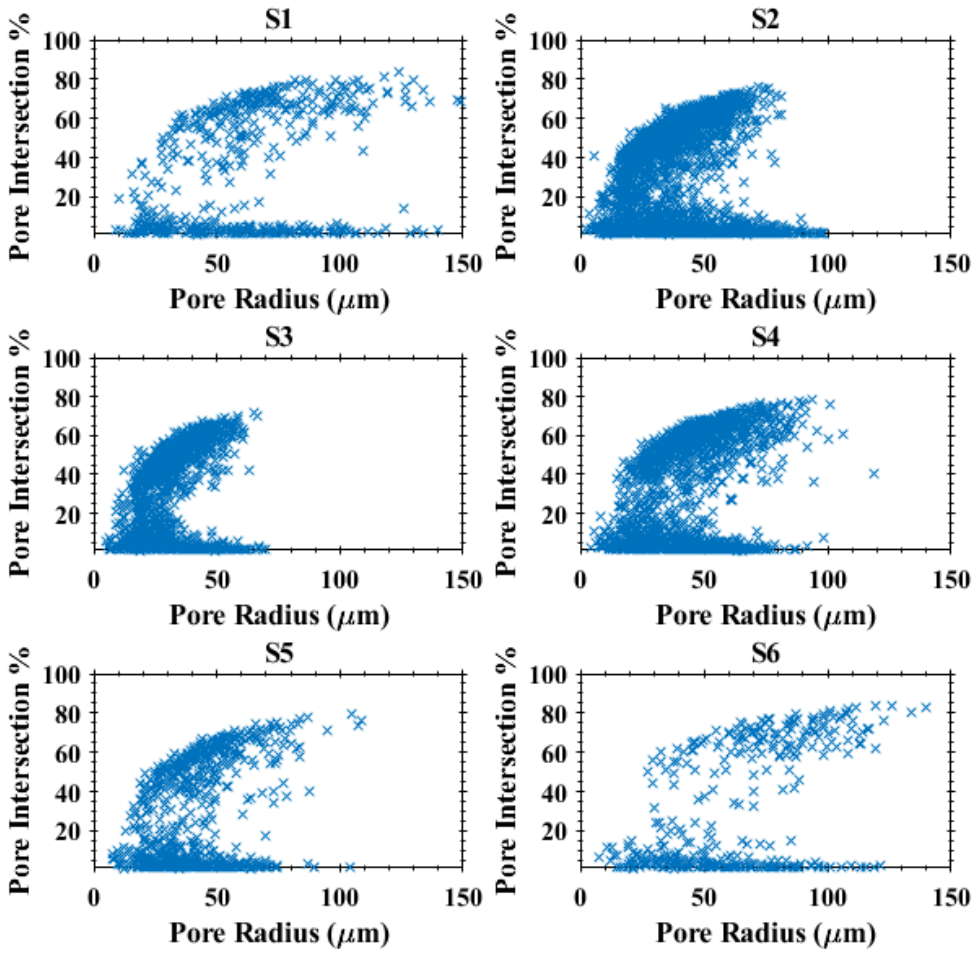

Figure 58. Residual Oil Occupancy Percentage Against Pore Radius for Each Pore in Silica Sand Systems S1-S6.

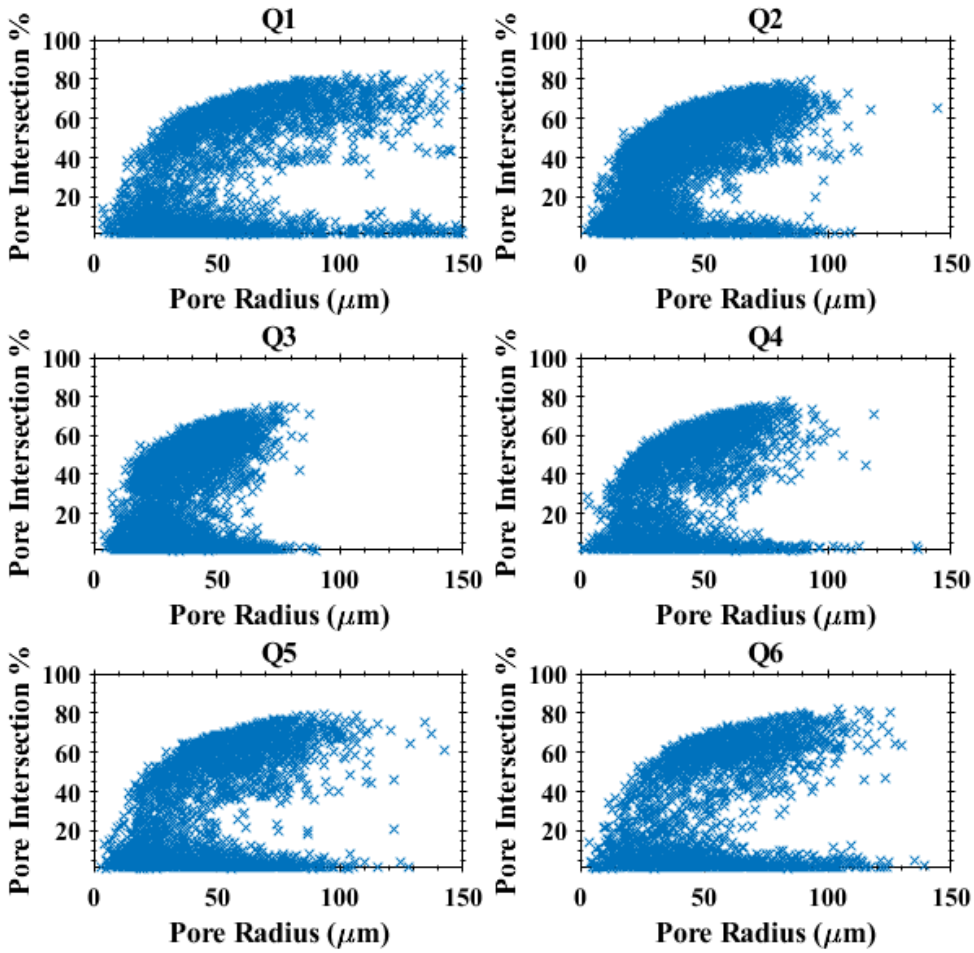

Figure 59. Residual Oil Occupancy Percentage Against Pore Radius for Each Pore in Quartz Sand Systems Q1-Q6.

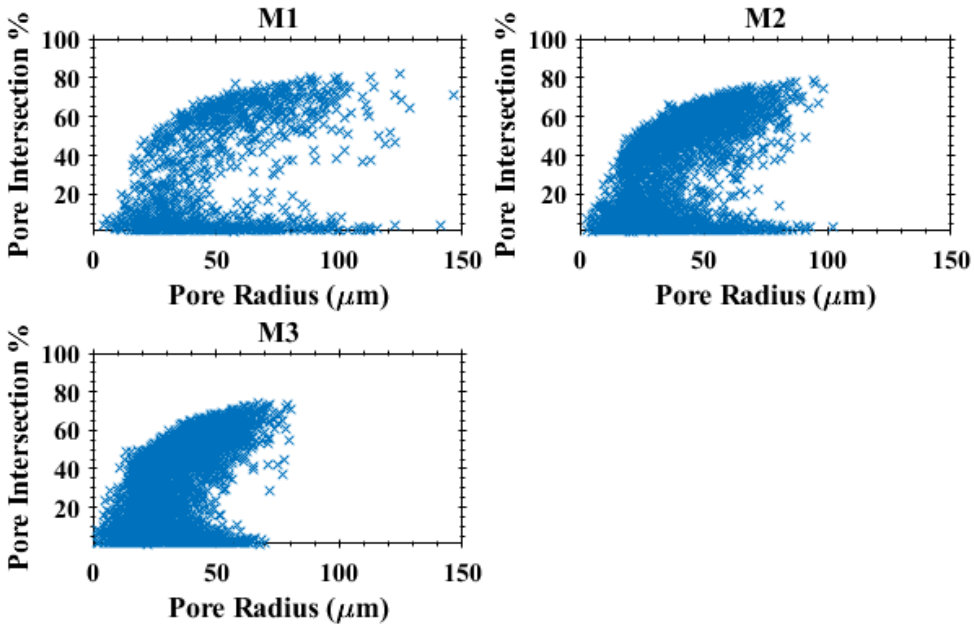

Figure 60. Residual Oil Occupancy Percentage Against Pore Radius for Each Pore in Mixed Sand Systems Q1-Q3.

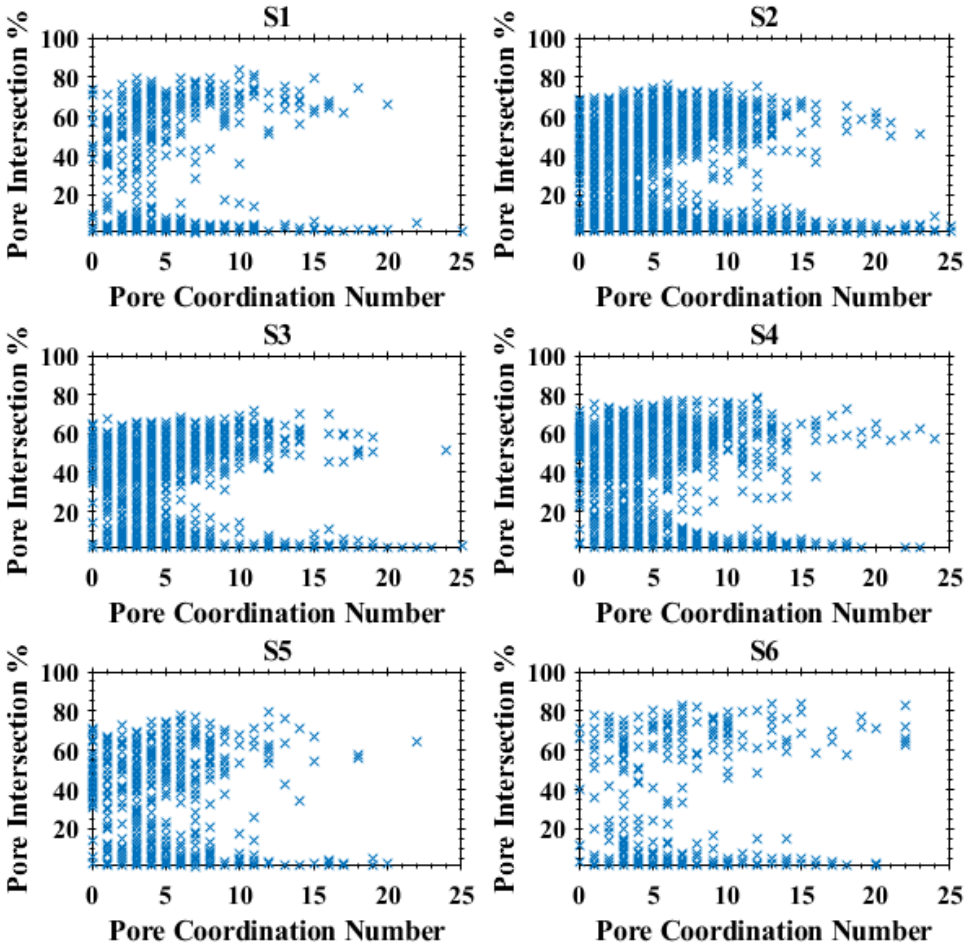

Figure 61. Residual Oil Occupancy Percentage Against Pore Coordination Number for Each Pore in Silica Sand Systems S1-S6.

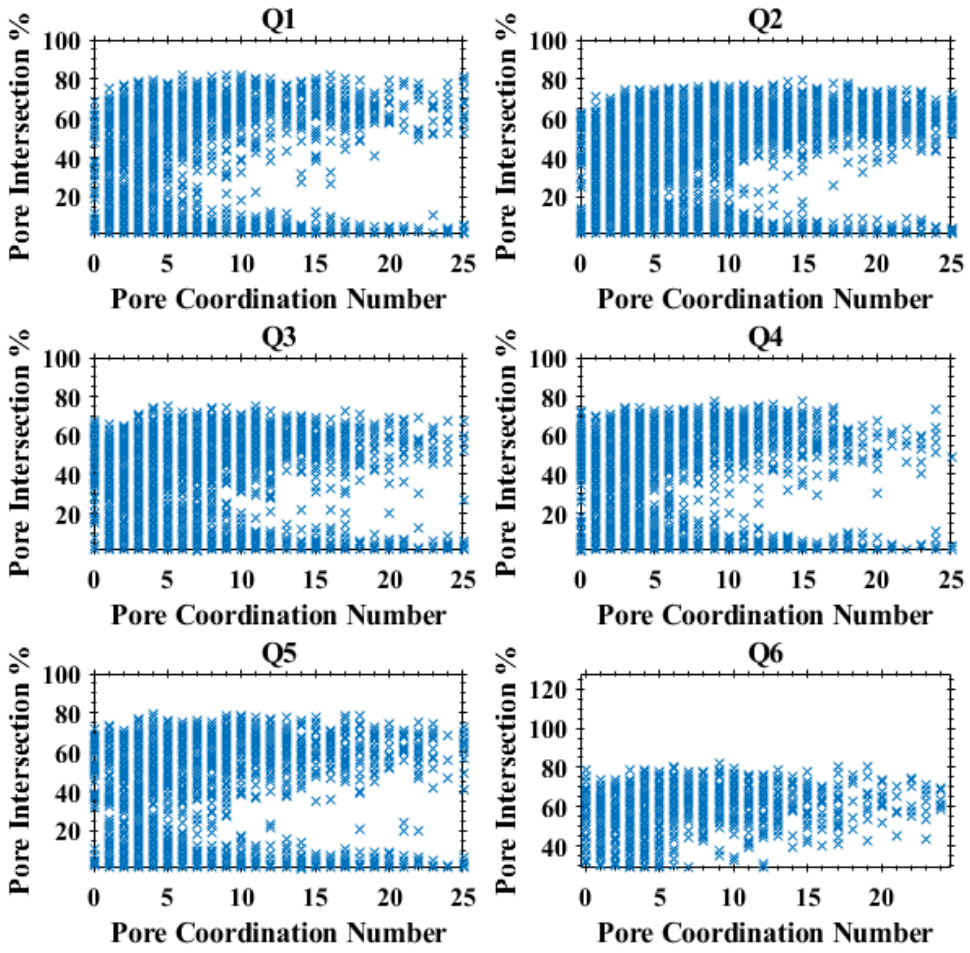

Figure 62. Residual Oil Occupancy Percentage Against Pore Coordination Number for Each Pore in Quartz Sand Systems Q1-Q6.

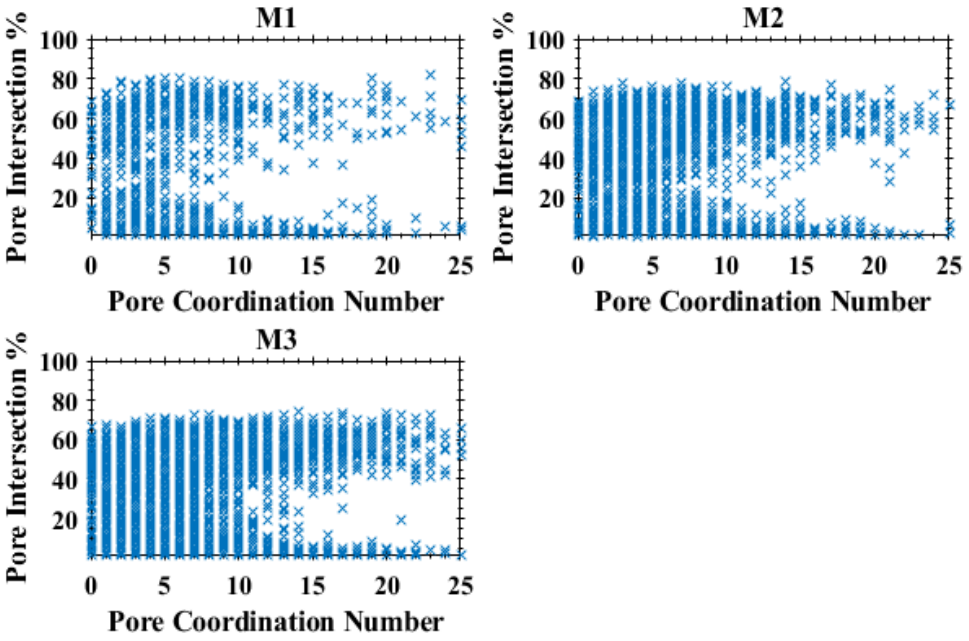

Figure 63. Residual Oil Occupancy Percentage Against Pore Coordination Number for Each Pore in Mixed Sand Systems M1-M3.

Pore Radii histogram plots (see Figure 64., Figure 65., and Figure 66.) show similar behavior with grains diameter, where Poisson distribution was dominant for all fifteen sand samples for the pores space probability values against their diameters. Pore Radii with Poisson distribution occur in sand due to the sediment size distribution and agree with the observation in the literature (Bellato et al., 2020; Mahmoodlu et al., 2020; Thakur et al., 2020; J. Sun et al., 2021; Zhang et al., 2020). It was observed that silica samples S2, S3, S4, and S5 radius distributions were ranging between 5 to 110 micrometers, where both ends have lower probabilities compared to middle values (40 micrometers for example in silica sample S3), while silica samples S1 and S6 had wider distribution range 5 to 150 micrometers. Samples S1 and S6 had their probability peaks at around 70 micrometers or pore radius value, meaning that the pore radius of 70 micrometers was the most repeated pore radius value for samples S1 and S6 (see Figure 64). Quartz sand exhibited similar properties, where samples Q2, Q3, Q4, Q5, and Q6 had average pore radius values ranging between 0 to 130 micrometers. However, quartz sample Q1 had the widest range (0 to 150 micrometers). It was observed that quartz sand had lower average peak values (always lower than 50 micrometers) compared to silica sands (between 40 and 70 micrometers) (see Figure 65). Mixed samples M2 and M3 have a narrow distribution (0 to 90 micrometers) compared to sample M1 (5 to 130 micrometers). Additionally, peak probability values were scattered in the mixed sample mainly due to the mixing effect of quartz and silica (both have different peak value ranges).

When observing the “Pore Probability Against Pore Occupancy Histogram” figures, it appears at first that all figures maintain a C-shape (previously observed in Figure 58., Figure 59., and Figure 60.). Going from the left side of Figure 67., Figure 68., and Figure 69. having an empty pore space (0% NAPL occupancy) remains the

highest probability for all the fifteen sand samples. The NAPL occupancy percentages then drop till reaching values between 20%-40% of NAPL occupancy. That even region is followed by an incline of occupancy percentages that is followed by a final drop (occurs after 60% occupancy on average), which reaches the maximum occupancy percentage of any pore space (80%).

The “Pore Probability Against Pore Coordination Number Histogram” figures show that pores having coordination numbers between 4 and 5 have the highest probabilities to be occupied by NAPL. That observation applies to all fifteen sand samples. The probability of having a pore space that is occupied by NAPL start to drop dramatically with the increase of coordination numbers higher than 5-6. That is clearly observed in quartz sand (see Figure 71.) and mixed sand (Figure 72.). However, silica sand samples maintain smaller values after coordination number 5 that rang between coordination numbers 6 to 10 (see Figure 70.). Finally, pore occupancy dropping behavior act in a similar way as in quartz and mixed samples.

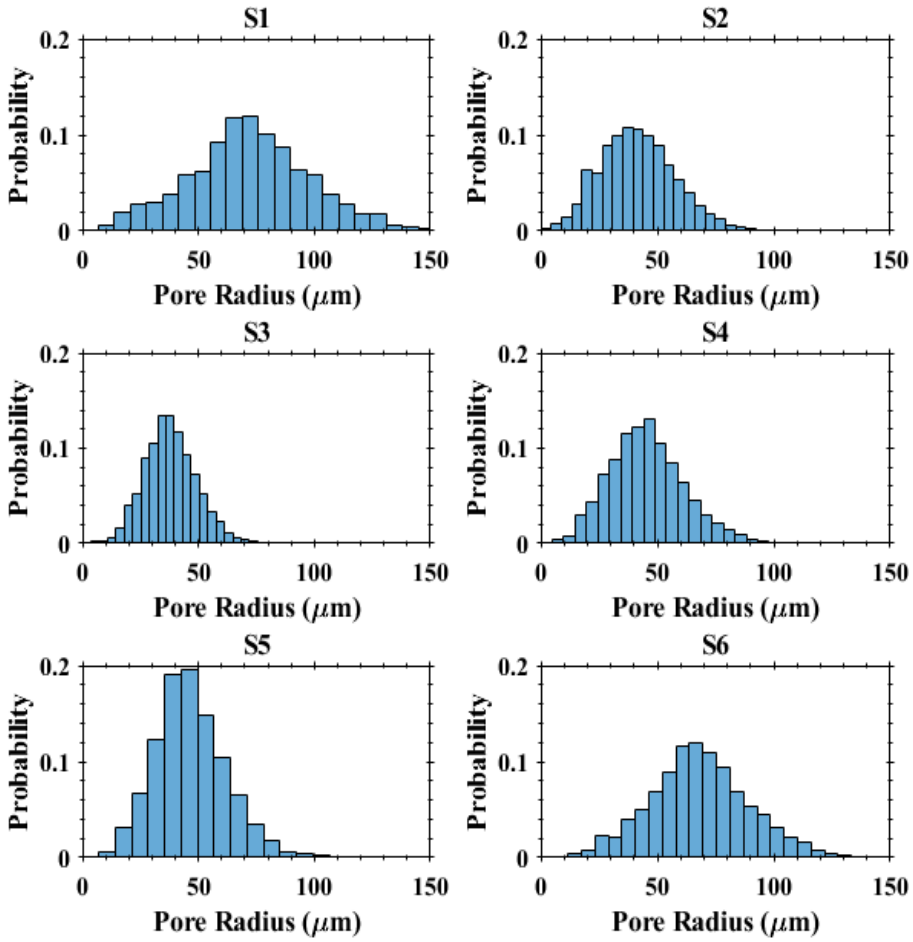

Figure 64. Pore Probability Against Pore Radiuses Histogram for Silica Sand Samples S1-S6.

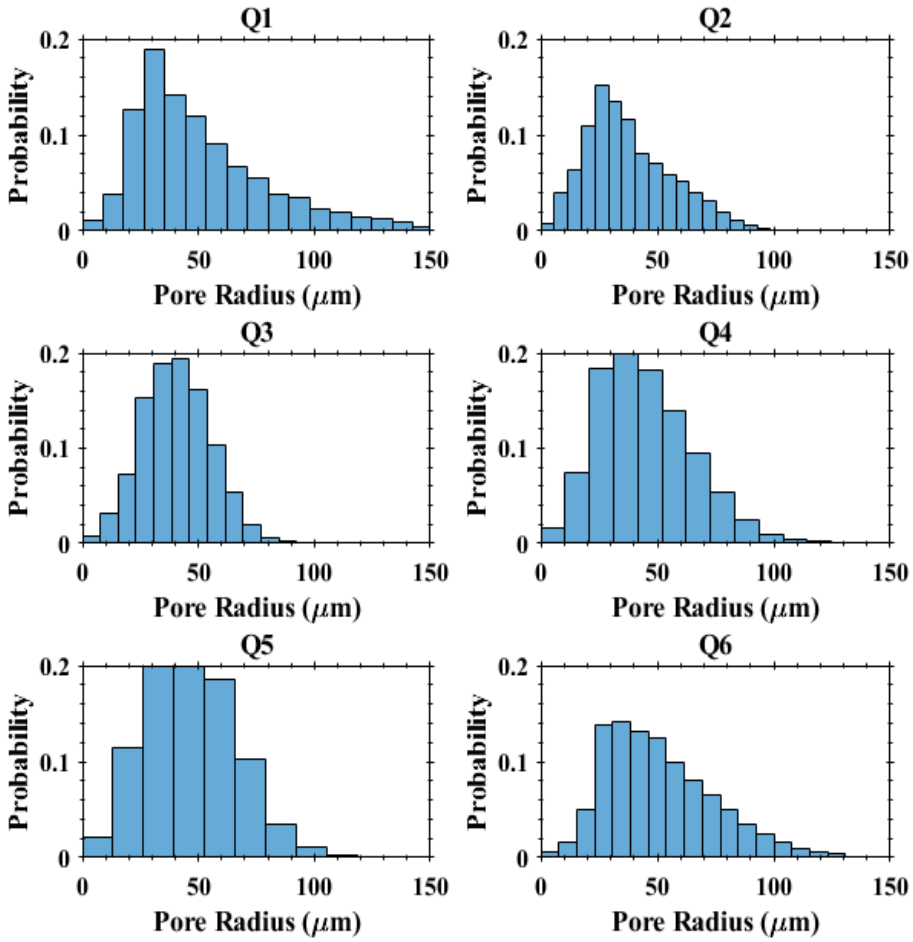

Figure 65. Pore Probability Against Pore Radiuses Histogram for Quartz Sand Samples Q1-Q6.

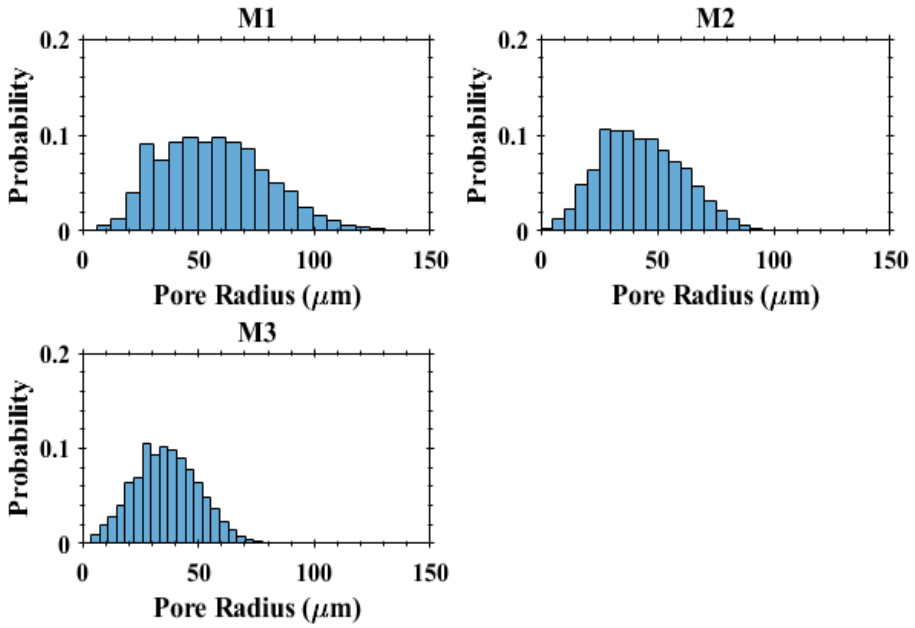

Figure 66. Pore Probability Against Pore Radiuses Histogram for Mixed Sand Samples M1-M3.

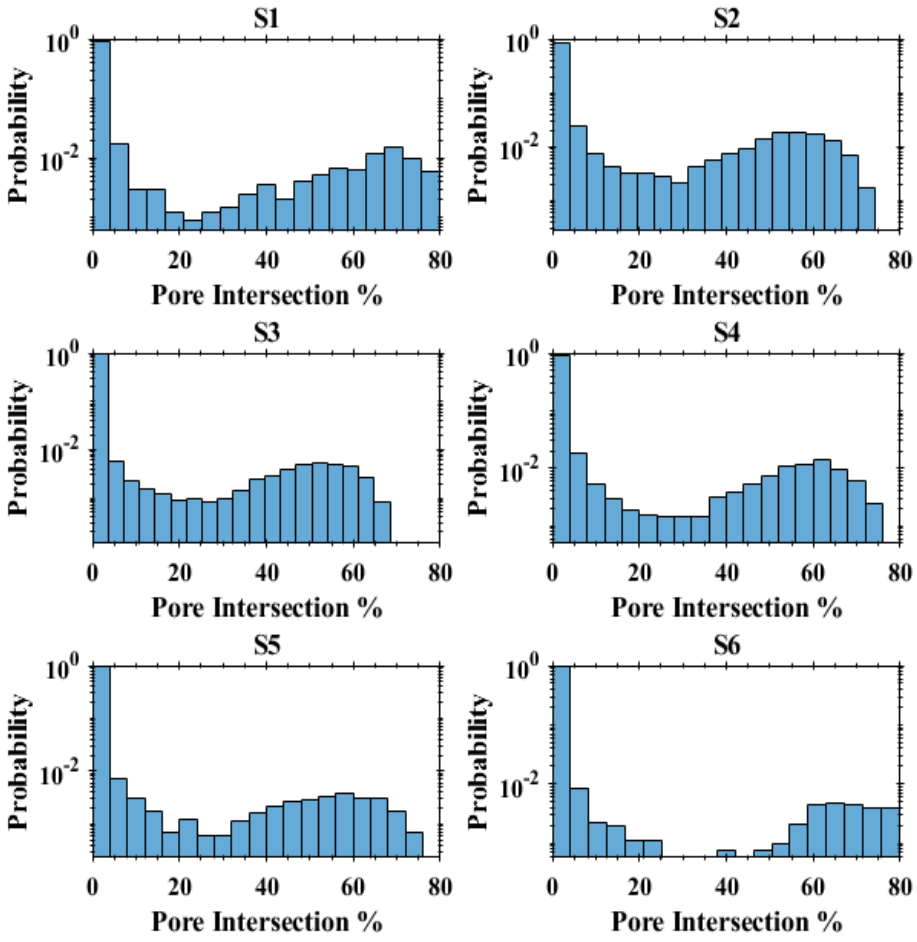

Figure 67. Pore Probability Against Pore Occupancy Histogram for Silica Sand Samples S1-S6.

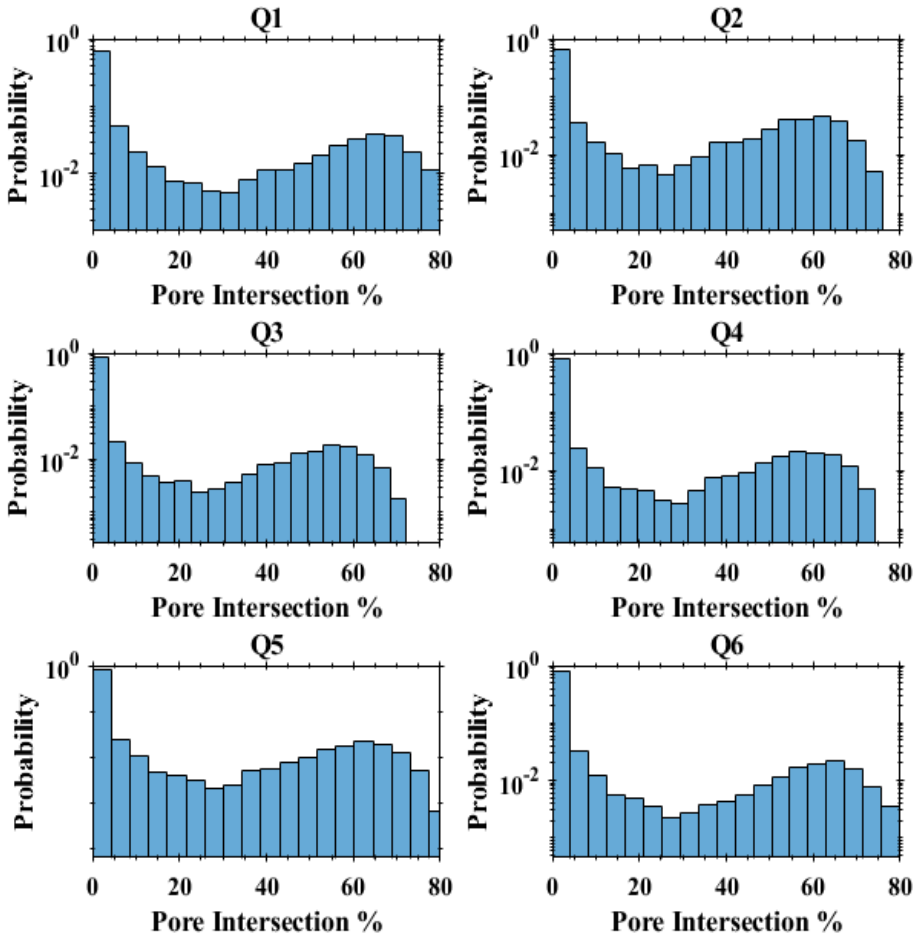

Figure 68. Pore Probability Against Pore Occupancy Histogram for Quartz Sand Samples Q1-Q6.

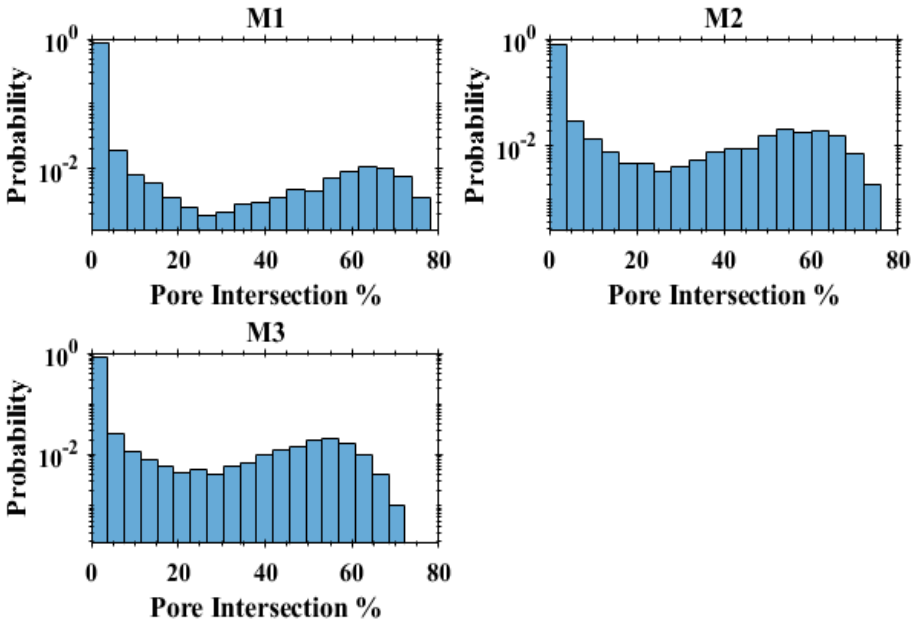

Figure 69. Pore Probability Against Pore Occupancy Histogram for Mixed Sand Samples M1-M3.

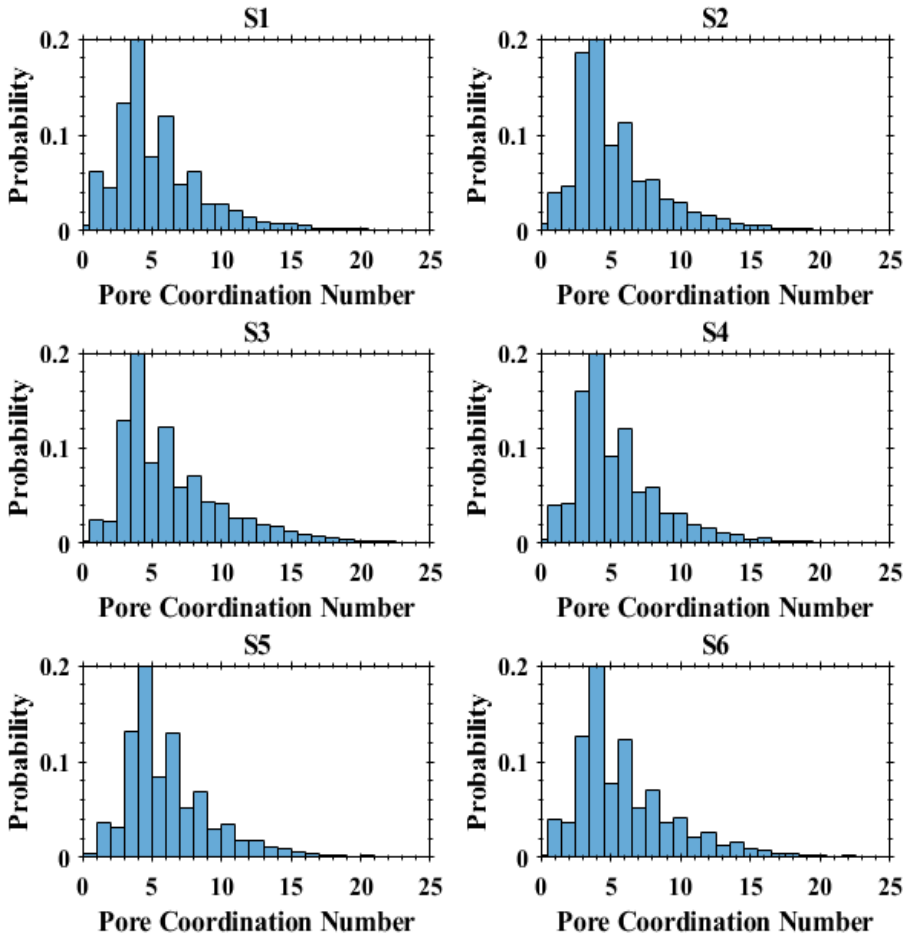

Figure 70. Pore Probability Against Pore Coordination Number Histogram for Silica Sand Samples S1-S6.

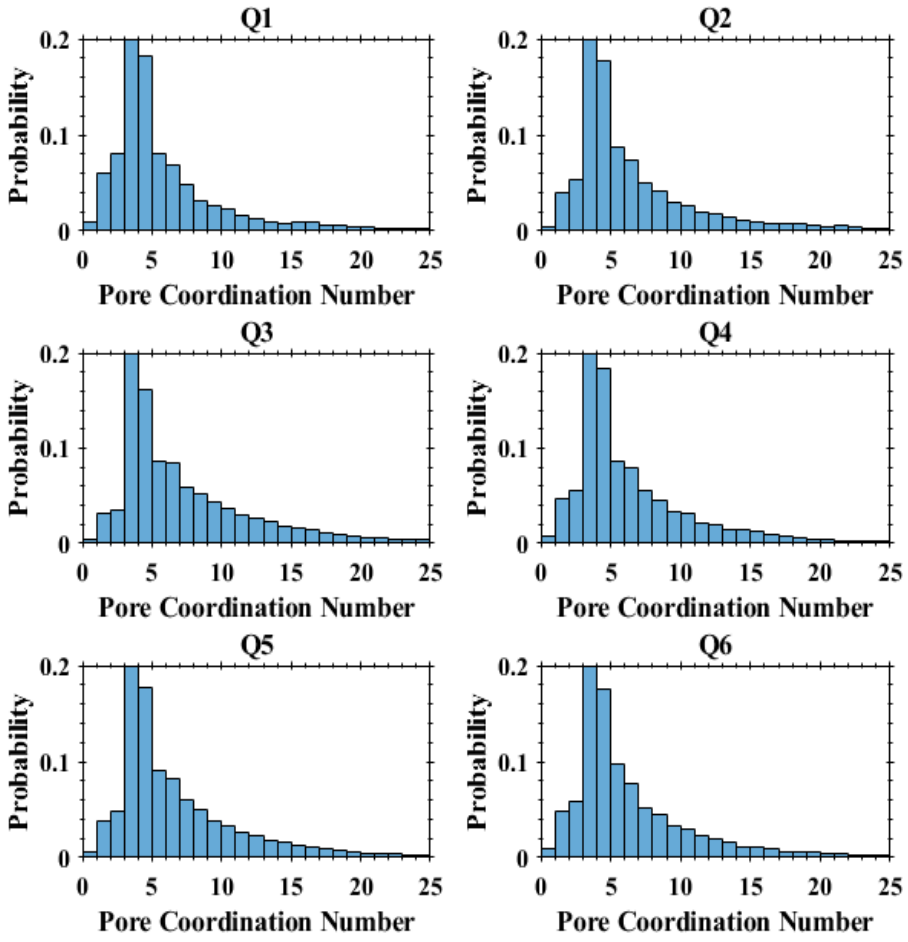

Figure 71. Pore Probability Against Pore Coordination Number Histogram for Quartz Sand Samples Q1-Q6.

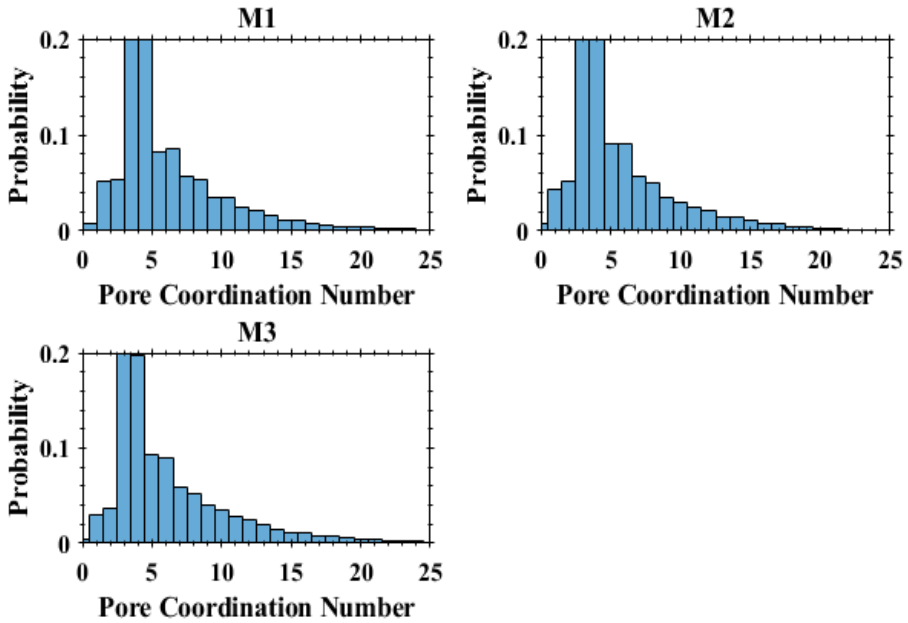

Figure 72. Pore Probability Against Pore Coordination Number Histogram for Mixed Sand Samples M1-M3.

CHAPTER 6: CONCLUSIONS

Experiments were carried out on fifteen unconsolidated sand samples (silica sand, quartz sand, and mixed sand samples) to simulate the trapped NAPL in unconsolidated porous media, where all samples were first flooded by water at a rate of 4.07ml/hour followed by NAPL injection then another water flooding procedure. The main objective of that process was to find the correlation between occupancy (of residual NAPL) ratio in pores with respect to pore sizes for various unconsolidated sands and with respect to pore coordination numbers. X-ray micro-computed scans were used to construct the three-dimensional models of all fifteen sand samples, where raw images were filtered and segmented (using PerGeos software) in order to give a distinctive label for each material phase in all samples. The research finally concluded that:

1. The NAPL occupancy interval increases for pores that were occupied by residual NAPL more than 20%, while the NAPL occupancy interval decreases for pores that were occupied by residual NAPL less than 20% as the pore radius increases.
2. The interface between water and trapped NAPL was lower in the pores compared to throats based on the fact that the distribution was unequal along with occupancy percentage ranges between 20%-40%.
3. Irreducible water saturation resulted in preventing any NAPL pore occupancy from reaching a value greater than 80%.
4. Pores with coordination numbers between one and four were evenly distributed on average over the occupancy percentage range.
5. Pores with coordination numbers higher than five were segregated either above 50% intersection or below 10% intersection.

The significance of the above conclusions is directly related to having a better characterization/understanding of how trapped NAPLs behave in each pore of real geological samples (silica and quartz sands). That can contribute to industrial applications such as improved oil recovery percentages from oil reservoirs. Building volume images of ganglia's geometry inside the sand samples improved the understanding of how ganglia are stored/trapped within the sand pores and throats, which can be beneficial in soil remediation and carbon subsurface storage applications.

REFERENCES

Akarri, S. (2019). *Pore-Scale Investigation of the Impact of Silica-Based Nanofluid on Residual Oil*. NTNU. Retrieved from https://ntnuopen.ntnu.no/ntnu-xmlui/handle/11250/2622377

Al-Kharusi, A. S., & Blunt, M. J. (2007). Network extraction from sandstone and carbonate pore space images. *Journal of Petroleum Science and Engineering*, *56*(4), 219–231. https://doi.org/10.1016/j.petrol.2006.09.003

Al-Raoush, R., Hannun, J., Jarrar, Z., Alshibli, K., & Jung, J. (2019). Impact of fines type on gas flow using 3D micro-computed tomography. In *Society of Petroleum Engineers - SPE Kuwait Oil and Gas Show and Conference 2019, KOGS 2019*. Society of Petroleum Engineers. https://doi.org/10.2118/198106-ms

Al-Raoush, R. I. (2009). Impact of wettability on pore-scale characteristics of residual nonaqueous phase liquids. *Environmental Science and Technology*, *43*(13), 4796–4801. https://doi.org/10.1021/es802566s

Al-Raoush, R. I. (2014). Experimental investigation of the influence of grain geometry on residual NAPL using synchrotron microtomography. *Journal of Contaminant Hydrology*, *159*, 1–10. https://doi.org/10.1016/j.jconhyd.2014.01.008

Al-Raoush, R. I., & Willson, C. S. (2005). A pore-scale investigation of a multiphase porous media system. *Journal of Contaminant Hydrology*, *77*(1–2), 67–89. https://doi.org/10.1016/j.jconhyd.2004.12.001

Alhammadi, A. M., Gao, Y., Akai, T., Blunt, M. J., & Bijeljic, B. (2020). Pore-scale X-ray imaging with measurement of relative permeability, capillary pressure and oil recovery in a mixed-wet micro-porous carbonate reservoir rock. *Fuel*, *268*, 117018. https://doi.org/10.1016/j.fuel.2020.117018

Alhosani, A., Scanziani, A., Lin, Q., Foroughi, S., Alhammadi, A. M., Blunt, M. J., &

Bijeljic, B. (2020). Dynamics of water injection in an oil-wet reservoir rock at subsurface conditions: Invasion patterns and pore-filling events. *Physical Review E*, *102*(2), 23110. https://doi.org/10.1103/PhysRevE.102.023110

Andersson, L., Schlueter, S., & Wildenshild, D. (2018). Defining a novel pore-body to pore-throat "Morphological Aspect Ratio" that scales with residual non-wetting phase capillary trapping in porous media. *Advances in Water Resources*, *122*, 251–262. https://doi.org/10.1016/j.advwatres.2018.10.009

Arns, C. H., Bauget, F., Limaye, A., Sakellariou, A., Senden, T. J., Sheppard, A. P., … Knackstedt, M. A. (2005). Pore-scale characterization of carbonates using x-ray microtomography. *SPE Journal*, *10*(4), 475–484. https://doi.org/10.2118/90368-PA

Bakke, S., & ØRen, P.-E. (2002). Process Based Reconstruction of Sandstones and Prediction of Transport Properties. *Transport in Porous Media*, *46*(2–3), 311–343. https://doi.org/10.1023/a:1015031122338

Bellato, D., Marzano, I. P., & Simonini, P. (2020). Microstructural Analyses of a Stabilized Sand by a Deep-Mixing Method. *Journal of Geotechnical and Geoenvironmental Engineering*, *146*(6), 04020032. https://doi.org/10.1061/(ASCE)GT.1943-5606.0002254

Blunt, M. J., Bijeljic, B., Dong, H., Gharbi, O., Iglauer, S., Mostaghimi, P., … Pentland, C. (2013). Pore-scale imaging and modelling. *Advances in Water Resources*, *51*, 197–216. https://doi.org/10.1016/j.advwatres.2012.03.003

Brownrigg, D. R. K. (1984). The Weighted Median Filter. *Communications of the ACM*, *27*(8), 807–818. https://doi.org/10.1145/358198.358222

Brusseau, M. L., Peng, S., Schnaar, G., & Murao, A. (2007). Measuring air-water interfacial areas with X-ray microtomography and interfacial partitioning tracer

tests. *Environmental Science and Technology*, *41*(6), 1956–1961. https://doi.org/10.1021/es061474m

Chatzis, I., Morrow, N. R., & Lim, H. T. (1983). MAGNITUDE AND DETAILED STRUCTURE OF RESIDUAL OIL SATURATION. *Society of Petroleum Engineers Journal*, *23*(2), 311–326. https://doi.org/10.2118/10681-PA

Coles, M. E., Hazlett, R. D., Muegge, E. L., Jones, K. W., Andrews, B., Dowd, B., … Soll, W. E. (1998). Developments in Synchrotron X-Ray Microtomogrqphy with Applications to Flow in Porous Media. *SPE Reservoir Engineering (Society of Petroleum Engineers)*, *1*(4), 288–296. https://doi.org/10.2118/50985-pa

Cowell, M. A., Kibbey, T. C. G., Zimmerman, J. B., & Hayes, K. (2000). Partitioning of ethoxylated nonionic surfactants in water/NAPL systems: Effects of surfactant and NAPL properties. *Environmental Science and Technology*, *34*(8), 1583–1588. https://doi.org/10.1021/es9908826

Daigang, W., Yongle, H., & Jingjing, S. (2015). X-ray MCT based numerical analysis of residual oil pore-scale characteristics under various displacing systems. *Journal of Petroleum Science and Engineering*, *135*, 168–176. https://doi.org/10.1016/j.petrol.2015.09.015

Doan, D. H., Delage, P., Nauroy, J. F., Tang, A. M., & Youssef, S. (2012, October). Microstructural characterization of a Canadian oil sand. *Canadian Geotechnical Journal*. NRC Research Press . https://doi.org/10.1139/T2012-072

Dong, H., & Blunt, M. J. (2009). Pore-network extraction from micro-computerized-tomography images. *Physical Review E*, *80*(3), 036307. https://doi.org/10.1103/PhysRevE.80.036307

Etkin, D. (1999). HISTORICAL OVERVIEW OF OIL SPILLS FROM ALL SOURCES (1960-1998)). In *International Oil Spill Conference* . Arlington.

Fang, Y., Yang, E., & Cui, X. (2019). Study on Distribution Characteristics and Displacement Mechanism of Microscopic Residual Oil in Heterogeneous Low Permeability Reservoirs. *Geofluids*, *2019*, 12. https://doi.org/10.1155/2019/9752623

Frollini, E., & Petitta, M. (2018). Free LNAPL volume estimation by pancake model and vertical equilibrium model: Comparison of results, limitations, and critical points. *Geofluids*, *2018*. https://doi.org/10.1155/2018/8234167

Gao, Y., Raeini, A. Q., Blunt, M. J., & Bijeljic, B. (2019). Pore Occupancy, Relative Permeability and Flow Intermittency Measurements Using X-Ray Micro-tomography in a Complex Carbonate. *Advances in Water Resources*. https://doi.org/10.1016/j.advwatres.2019.04.007

Heshmati, M., & Piri, M. (2018). Interfacial boundary conditions and residual trapping: A pore-scale investigation of the effects of wetting phase flow rate and viscosity using micro-particle image velocimetry. *Fuel*, *224*, 560–578. https://doi.org/10.1016/j.fuel.2018.03.010

Hu, Y., She, Y., Patmonoaji, A., Zhang, C., & Suekane, T. (2020). Effect of capillary number on morphological characterizations of trapped gas bubbles: Study by using micro-tomography. *International Journal of Heat and Mass Transfer*, *163*, 120508. https://doi.org/10.1016/j.ijheatmasstransfer.2020.120508

Huijer, K. (n.d.). *Trends in Oil Spills from Tanker Ships 1995-2004*. London.

Huling, S. G., & Weaver, J. W. (1991). *Ground Water Issue DENSE NONAQUEOUS PHASE LIQUIDS*. Washington, D.C.

Iglauer, S., Fernø, M. A., Shearing, P., & Blunt, M. J. (2012). Comparison of residual oil cluster size distribution, morphology and saturation in oil-wet and water-wet sandstone. *Journal of Colloid and Interface Science*, *375*(1), 187–192.

https://doi.org/10.1016/j.jcis.2012.02.025

Iglauer, S., Paluszny, A., & Blunt, M. J. (2013). Simultaneous oil recovery and residual gas storage: A pore-level analysis using in situ X-ray micro-tomography. In *Fuel* (Vol. 103, pp. 905–914). Elsevier. https://doi.org/10.1016/j.fuel.2012.06.094

Iglauer, Stefan, Favretto, S., Spinelli, G., Schena, G., & Blunt, M. J. (2010). X-ray tomography measurements of power-law cluster size distributions for the nonwetting phase in sandstones. *Physical Review E - Statistical, Nonlinear, and Soft Matter Physics*, *82*(5). https://doi.org/10.1103/PhysRevE.82.056315

Iglauer, Stefan, Paluszny, A., Pentland, C. H., & Blunt, M. J. (2011). Residual CO_2 imaged with X-ray micro-tomography. *Geophysical Research Letters*, *38*(21), n/a-n/a. https://doi.org/10.1029/2011GL049680

Iglauer, Stefan, Paluszny, A., Rahman, T., Zhang, Y., Wülling, W., & Lebedev, M. (2019). Residual Trapping of CO in an Oil-Filled, Oil-Wet Sandstone Core: Results of Three-Phase Pore-Scale Imaging. *Geophysical Research Letters*, *46*(20), 11146–11154. https://doi.org/10.1029/2019GL083401

Iglauer, Stefan, Rahman, T., Sarmadivaleh, M., Al-Hinai, A., Fernø, M. A., & Lebedev, M. (2016). Influence of wettability on residual gas trapping and enhanced oil recovery in three-phase flow: A pore-scale analysis by use of microcomputed tomography. *SPE Journal*, *21*(6), 1916–1929. https://doi.org/10.2118/179727-PA

Jernelöv, A., & Lindén, O. (1981). Ixtoc I: A Case Study of the World's Largest Oil Spill. *Ambio*, *10*(6), 299–306.

Karpyn, Z. T., Piri, M., & Singh, G. (2010). Experimental investigation of trapped oil clusters in a water-wet bead pack using X-ray microtomography. *Water Resources Research*, *46*(4), 4510. https://doi.org/10.1029/2008WR007539

Kazemi, F., Azin, R., & Osfouri, S. (2020). Evaluation of phase trapping models in gas-

condensate systems in an unconsolidated sand pack. *Journal of Petroleum Science and Engineering*, *195*, 107848. https://doi.org/10.1016/j.petrol.2020.107848

Khordagui, H., & Al-Ajmi, D. (1993). Environmental impact of the Gulf War: An integrated preliminary assessment. *Environmental Management*, *17*(4), 557–562. https://doi.org/10.1007/BF02394670

Konečný, F., Boháček, Z., Müller, P., Kovářová, M., & Sedláčková, I. (2003). Contamination of soils and groundwater by petroleum hydrocarbons and volatile organic compounds-Case study: ELSLAV BRNO. *Bulletin of Geosciences*, *78*(3), 225–239.

Lebedeva, E. V., & Fogden, A. (2011). Micro-CT and wettability analysis of oil recovery from sand packs and the effect of waterflood salinity and kaolinite. *Energy and Fuels*, *25*(12), 5683–5694. https://doi.org/10.1021/ef201242s

Li, J., Gao, Y., Jiang, H., Liu, Y., & Dong, H. (2018). Pore-Scale imaging of the oil cluster dynamic during drainage and imbibition using in situ x-ray microtomography. *Geofluids*, *2018*. https://doi.org/10.1155/2018/7679607

Liang, X., Zhou, F., Liang, T., Su, H., Yuan, S., & Li, Y. (2020). Impacts of pore structure and wettability on distribution of residual fossil hydrogen energy after imbibition. *International Journal of Hydrogen Energy*, *45*(29), 14779–14789. https://doi.org/10.1016/j.ijhydene.2020.03.208

Lin, Q., Bijeljic, B., Foroughi, S., Berg, S., & Blunt, M. J. (2021). Pore-scale imaging of displacement patterns in an altered-wettability carbonate. *Chemical Engineering Science*, *235*, 116464. https://doi.org/10.1016/j.ces.2021.116464

Liu, X., Ren, D., Dong, F., Nan, J., & Zhou, R. (2021). Quantitative Study of Residual Oil Distribution during Water Flooding through Digital Core Analysis. *Geofluids*, *2021*. https://doi.org/10.1155/2021/6619440

Liu, Z., Cheng, H., Xu, C., Chen, Y., Chen, Y., & Li, Y. (2018). Effect of lithology on pore-scale residual oil displacement in chemical flooding using nuclear magnetic resonance experiments. In *Society of Petroleum Engineers - SPE EOR Conference at Oil and Gas West Asia 2018* (Vol. 2018-March). Society of Petroleum Engineers. https://doi.org/10.2118/190450-ms

Mahmoodlu, M. G., Raoof, A., Bultreys, T., Van Stappen, J., & Cnudde, V. (2020). Large-scale pore network and continuum simulations of solute longitudinal dispersivity of a saturated sand column. *Advances in Water Resources*, *144*, 103713. https://doi.org/10.1016/j.advwatres.2020.103713

Mehmani, A., Kelly, S., Torres-Verdín, C., & Balhoff, M. (2019). Residual oil saturation following gas injection in sandstones: Microfluidic quantification of the impact of pore-scale surface roughness. *Fuel*, *251*, 147–161. https://doi.org/10.1016/j.fuel.2019.02.118

Mohamed, A. I. A., Khishvand, M., & Piri, M. (2020). A pore-scale experimental investigation of process-dependent capillary desaturation. *Advances in Water Resources*, *144*, 103702. https://doi.org/10.1016/j.advwatres.2020.103702

Mohsin Thakur, M., Penumadu, D., & Bauer, C. (2020). Capillary Suction Measurements in Granular Materials and Direct Numerical Simulations Using X-Ray Computed Tomography Microstructure. *Journal of Geotechnical and Geoenvironmental Engineering*, *146*(1), 04019121. https://doi.org/10.1061/(ASCE)GT.1943-5606.0002194

Morrow, N. R., Chatzis, I., & Taber, J. J. (1988). Entrapment and mobilization of residual oil in bead packs. *SPE Reservoir Engineering (Society of Petroleum Engineers)*, *3*(3), 927–934. https://doi.org/10.2118/14423-PA

Nwilo, P. C., & Badejo, O. T. (2005). Oil spill problems and management in the Niger

Delta. In *2005 International Oil Spill Conference, IOSC 2005* (Vol. 2005, pp. 11400–11403). Allen Press. https://doi.org/10.7901/2169-3358-2005-1-567

Oren, P. E., Billotte, J., & Pinczewski, W. V. (1992). Mobilization of waterflood residual oil by gas injection for water-wet conditions. *SPE Formation Evaluation*, *7*(1), 70–78. https://doi.org/10.2118/20185-PA

Pratt, W. (2013). *Introduction to Digital Image Processing - 1st Edition - William K. P*. CRC Press.

Princ, T., Fideles, H. M. R., Koestel, J., & Snehota, M. (2020). The Impact of Capillary Trapping of Air on Satiated Hydraulic Conductivity of Sands Interpreted by X-ray Microtomography. *Water*, *12*(2), 445. https://doi.org/10.3390/w12020445

Prodanović, M., Lindquist, W. B., & Seright, R. S. (2006). Porous structure and fluid partitioning in polyethylene cores from 3D X-ray microtomographic imaging. *Journal of Colloid and Interface Science*, *298*(1), 282–297. https://doi.org/10.1016/j.jcis.2005.11.053

Raeini, A. Q., Bijeljic, B., & Blunt, M. J. (2017). Generalized network modeling: Network extraction as a coarse-scale discretization of the void space of porous media. *Physical Review E*, *96*(1), 013312. https://doi.org/10.1103/PhysRevE.96.013312

Scanziani, A., Singh, K., Bultreys, T., Bijeljic, B., & Blunt, M. J. (2018). In situ characterization of immiscible three-phase flow at the pore scale for a water-wet carbonate rock. *Advances in Water Resources*, *121*(June), 446–455. https://doi.org/10.1016/j.advwatres.2018.09.010

Scanziani, A., Singh, K., Menke, H., Bijeljic, B., & Blunt, M. J. (2020). Dynamics of enhanced gas trapping applied to CO2 storage in the presence of oil using synchrotron X-ray micro tomography. *Applied Energy*, *259*, 114136.

https://doi.org/10.1016/j.apenergy.2019.114136

Schnaar, G., & Brusseau, M. L. (2005). Pore-scale characterization of organic immiscible-liquid morphology in natural porous media using synchrotron x-ray microtomography. *Environmental Science and Technology*, *39*(21), 8403–8410. https://doi.org/10.1021/es0508370

Shabaninejad, M. (2017). *Pore-scale Analysis of Residual Oil in Sandstones and its Dependence on Waterflood Salinity, Analysed by Tomography and Microscopy*. https://doi.org/10.25911/5D6663CBA5961

Singh, K., Menke, H., Andrew, M., Lin, Q., Rau, C., Blunt, M. J., & Bijeljic, B. (2017). Dynamics of snap-off and pore-filling events during two-phase fluid flow in permeable media. *Scientific Reports*, *7*(1), 1–13. https://doi.org/10.1038/s41598-017-05204-4

Song, R., Peng, J., Sun, S., Wang, Y., Cui, M., & Liu, J. (2020). Visualized Experiments on Residual Oil Classification and Its Influencing Factors in Waterflooding Using Micro-Computed Tomography. *Journal of Energy Resources Technology*, *142*(8). https://doi.org/10.1115/1.4045926

Sun, J., Dong, H., Arif, M., Yu, L., Zhang, Y., Golsanami, N., & Yan, W. (2021). Influence of pore structural properties on gas hydrate saturation and permeability: A coupled pore-scale modelling and X-ray computed tomography method. *Journal of Natural Gas Science and Engineering*, *88*, 103805. https://doi.org/10.1016/j.jngse.2021.103805

Sun, T., & Neuvo, Y. (1994). Detail-preserving median based filters in image processing. *Pattern Recognition Letters*, *15*(4), 341–347. https://doi.org/10.1016/0167-8655(94)90082-5

Wang, Q., Zhang, S., Li, Y., & Klassen, W. (2011). Potential Approaches to Improving

Biodegradation of Hydrocarbons for Bioremediation of Crude Oil Pollution. *Journal of Environmental Protection*, *02*(01), 47–55. https://doi.org/10.4236/jep.2011.21005

Wang, Y., Song, R., Liu, J. J., Cui, M. M., & Ranjith, P. G. (2019). Pore scale investigation on scaling-up micro-macro capillary number and wettability on trapping and mobilization of residual fluid. *Journal of Contaminant Hydrology*, *225*, 103499. https://doi.org/10.1016/j.jconhyd.2019.103499

Xiong, Q., Baychev, T. G., & Jivkov, A. P. (2016). Review of pore network modelling of porous media: Experimental characterisations, network constructions and applications to reactive transport. *Journal of Contaminant Hydrology*, *192*, 101–117. https://doi.org/10.1016/J.JCONHYD.2016.07.002

Yadali Jamaloei, B., Kharrat, R., Asghari, K., & Torabi, F. (2011). The influence of pore wettability on the microstructure of residual oil in surfactant-enhanced water flooding in heavy oil reservoirs: Implications for pore-scale flow characterization. *Journal of Petroleum Science and Engineering*, *77*(1), 121–134. https://doi.org/10.1016/j.petrol.2011.02.013

Yang, Y., Tao, L., Iglauer, S., Hejazi, S. H., Yao, J., Zhang, W., & Zhang, K. (2020). Quantitative Statistical Evaluation of Micro Residual Oil after Polymer Flooding Based on X-ray Micro Computed-Tomography Scanning. *Energy and Fuels*, *34*(9), 10762–10772. https://doi.org/10.1021/acs.energyfuels.0c01801

Yu, B., & Cheng, P. (2002). A fractal permeability model for bi-dispersed porous media. *International Journal of Heat and Mass Transfer*, *45*(14), 2983–2993. https://doi.org/10.1016/S0017-9310(02)00014-5

Zhang, L., Ge, K., Wang, J., Zhao, J., & Song, Y. (2020). Pore-scale investigation of permeability evolution during hydrate formation using a pore network model

based on X-ray CT. *Marine and Petroleum Geology*, *113*, 104157. https://doi.org/10.1016/j.marpetgeo.2019.104157

Zhou, Y., Yin, D., Cao, R., & Zhang, C. (2018). The mechanism for pore-throat scale emulsion displacing residual oil after water flooding. *Journal of Petroleum Science and Engineering*, *163*, 519–525. https://doi.org/10.1016/j.petrol.2018.01.027